COARSE PARTICLES IN HIGH-STRENGTH LOW-ALLOY STEELS

CHARACTERIZATION OF FERRONIOBIUM AND THE THERMODYNAMICS AND KINETICS OF DISSOLUTION OF NIOBIUM COMPOUNDS IN LIQUID IRON

By AARON W. DEN BOER, B.ENG

A Thesis Submitted to the School of Graduate Studies in Partial Fulfillment of the Requirements for the Degree Master of Applied Sciences

MASTER OF APPLIED SCIENCE (2013) McMaster University

(Materials Science & Engineering) Hamilton, Ontario, Canada

TITLE: The Characterization of Ferroniobium and the Thermodynamics and Kinetics of Dissolution of Niobium Compounds in Liquid Iron

AUTHOR: Aaron W. Den Boer, B.Eng. (McMaster University)

SUPERVISOR: Professor Dmitri V. Malakhov

NUMBER OF PAGES: xiii, 118

Abstract

Solidification of Nb-microalloyed HSLA steels may result in the precipitation of niobium carbonitrides, which is hardly surprising in view of their extreme thermodynamic stability. Recently, it was proposed in literature that coarse Nb-rich particles found along the centerline of continuously cast HSLA steels originated from ferroniobium additions during ladle metallurgy. In particular, it was hypothesized that thermally stable phases formed during manufacturing of ferroniobium were released into the melt once the ferroniobium had partially fused. In this contribution, Scheil–Gulliver formalism is employed to predict the phase portrait of ferroniobium in an attempt to simulate the manufacturing process of ferroniobium.

To corroborate the predictions, the microstructure of ferroniobium is characterized to determine if thermally stable particles exist in ferroniobium. Further, a model is developed to predict the dissolution rate of thermally stable phases that were observed in ferroniobium as well as in the centerline region of as-cast HSLA steel. Finally, a sample near the centreline region of a Nb-microalloyed HSLA steel is characterized and centreline compositions are measured. Based on experimental evidences, an alternative explanation to the origin of thermally stable particles found near the centreline of HSLA steels is proposed.

Acknowledgments

I would like to acknowledge my professor and friend, Dr. Dmitri V. Malakhov for his unwavering support in this project. His constant encouragement and inquiring mind led to the fruition of this contribution. I am grateful for the mutual enrichment of our knowledge in this aspect of high temperature materials processing, and the opportunity to develop a fundamental scientific methodology under his supervision.

I would also like to thank the Steel Research Centre for their support of this project, as well as the advice and valuable discussions with Dr. Gordon A. Irons and Mr. John Thomson. I would like to thank the R&D division of Evraz North America Inc. for their contribution and interest in this project, in particular, Dr. Laurie Collins and Dr. Shahrooz Nafisi.

The completion of this research was aided with the support of my dear wife, Johanna, and I am grateful for her unfaltering assistance. In addition, I thank my parents for their influence in my formative years and encouragement during my studies.

I would like to thank my colleagues, in particular, Mr. Peyman Saidi, for mutually enriching discussions, as well as the assistance of the technical staff in the Materials Science and Engineering Department, including Mr. Ed McCaffery, Mr. Doug Culley and Mr. Xiaogang Li. In addition, I would like to extend appreciation to the staff of the Canadian Centre for Electron Microscopy for their advice in the sample preparation and characterization.

Table of Contents

List of Figures

List of Tables

List of Abbreviations and Symbols

Symbol	Definition	Unit
g	Gravity	m/s^2
υ	Velocity	m/s
D	Diffusion coefficient	m^2/s
R	Radius	m
t	Time	s
N	Mass flux	$kg/m^2/s$
ω	Mass fraction	
ω_i^*	Mass fraction of component *i* at the interface	
ω_i^∞	Mass fraction of component *i* far from the interface	
$(\omega_{Fe})_{ln}$	Mass fraction of the correction factor for non-dilute systems	
ρ	Density	kg/m^3
ν	Kinematic viscosity	m^2/s
Re	Reynolds number	
Sc	Schmidt number	
Gr	Grashof number	
Sh	Sherwood number	
m_i	Mass of component *i*	kg
$A_{int,i}$	Interfacial area of component *i*	m^2

Abbreviation	Definition
CBMM	Companhia Brasileira de Metalurgia e Mineração
HSLA	High-Strength Low-Alloy
DICTRA	DIffusionally Controlled TRAnsformations

Declaration of Academic Achievement

This contribution seeks to expand the body of knowledge surrounding the microstructure of ferroniobium and its relationship to the dissolution of ferroniobium in liquid steel. However, a consensus of the niobium-rich side of the Fe–Nb phase diagram has not been reached. For this reason, all computations making use of thermodynamic data must be supported with microstructural evidences.

The majority of publications on ferroniobium microstructures have neglected the the consideration of ferroniobium as a multiphase entity. The identification and characterization of thermally stable phases in ferroniobium is supported with predictions of the phase portrait of a ferroniobium alloy using computational thermodynamics. Also, the effect of carbon on the formation of thermally stables phases in ferroniobium will be an addition to the literature on ferroniobium microstructures.

Furthermore, numerous publications have discussed the dissolution of ferroniobium as a macroscopic object, but in a majority of cases, have failed to consider ferroniobium as a multiphase entity with thermally stable phases. Thus, this contribution will add to the knowledge on dissolution rates of these phases, which may not dissolve easily in liquid steel because of their thermodynamic stability.

Finally, this contribution examines coarse particles at the centreline region of a Nb-microalloyed HSLA steel. The common explanation for centerline segregation in microalloyed steels will be challenged based on experimental evidences. An alternative explanation is given that may provide the scientific community with an improved understanding of the origin of coarse Nb-rich particles in the centreline of HSLA steels.

1 Introduction

The assertion that microstructure controls mechanical properties of a metallic material is a concentrated wisdom gained from centuries of practical experience and decades of thinking. Physical metallurgy with a theory of dislocations as its integral part forms a solid scientific foundation the assertion rests upon. Even if it is comprehended what particular microstructure is needed to achieve required properties, it is not always obvious how it can be arrived at. It is apparent, however, that for a certain class of materials, there is only a limited number of ways to cause microstructural changes. In the case of HSLA steels, which this contribution is focused on, such changes can be induced by modifying composition, solidification conditions, and post-casting thermo-mechanical processing. It is indeed difficult to make a clever decision on concentrations of alloying additions, but once it is made, it seems much easier to produce a melt of a particular composition in a ladle.

It was discovered several decades ago that alloying steel with carbon would increase its strength, but worsen mechanical properties such as weldability, formability and fracture toughness. The heightened requirements for steel with improved mechanical properties began the push for developing a new class of steels. Researchers uncovered the effect of low-alloying elements on grain refinement and strengthening mechanisms during thermo-mechanical processing[1-3] of HSLA steels. Small amounts of elements such as niobium, titanium, and vanadium used in alloying steel gave birth to the class of microalloyed HSLA steels. In general, the compositions of HSLA steel are similar to

medium carbon steel, besides the microalloying elements. HSLA steels may have varying compositions depending on the strength requirements. Therefore, HSLA steels are classified according to their mechanical properties rather than composition.

The alloying process is performed during the secondary metallurgy process, also known as ladle metallurgy. In ladle metallurgy, among other things, the composition is modified to attain the target composition. The microalloying of steel is performed through the addition of ferroalloys to the melt. Once the ferroalloys have melted or dissolved, the alloying elements disperse in the melt and homogenization is achieved by bubbling argon from the bottom of the ladle. After the composition and temperature of the steel are in acceptable ranges, the ladle is moved to the caster for solidification.

Cast slabs are subjected to subsequent thermo-mechanical processing to enhance the mechanical properties. The formation of fine carbonitrides during hot rolling and other thermo-mechanical processes is the reason for precipitation strengthening of HSLA steels. These precipitates retard dislocation motion during deformation thus making the material stronger. In addition, precipitation of carbonitrides in austenite during controlled cooling prevents ferrite from forming; this results in a smaller ferrite grain size in the final product. The combination of these two phenomena results in a steel with enhanced mechanical properties (Figure 1). It must be emphasized that the size of precipitates are small, on the order of hundreds of nanometers (Figure 2).

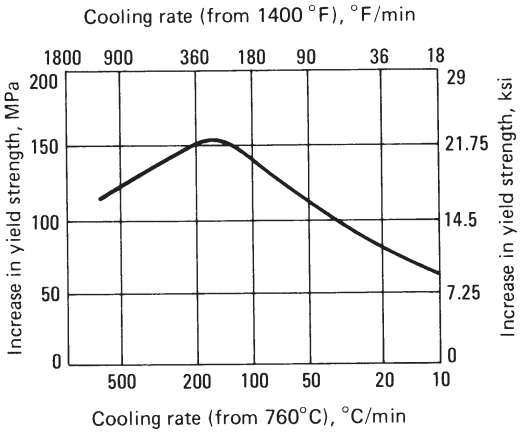

Figure 1 – The effect of cooling rate on the yield strength of a HSLA steel due to precipitation strengthening

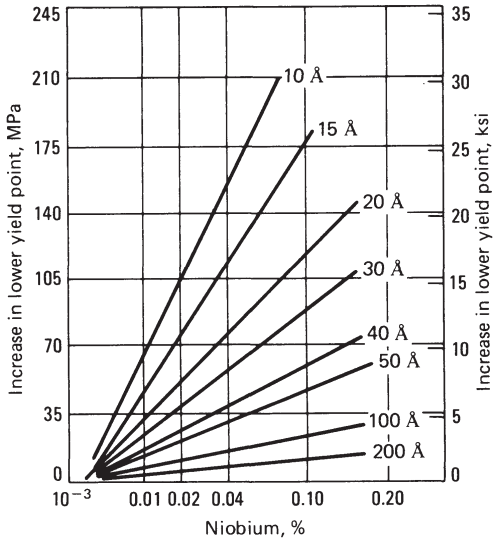

Figure 2 – The effect of wt. % of niobium and size of precipitates on the lower yield point of HSLA steel

The HSLA steels were originally developed in the 1960s for large-diameter oil and gas pipelines. Currently, these markets still constitute an important category of the HSLA steels and are estimated to be around 12 % of total world steel production. In this industry, sour service pipelines are of particular interest because of small concentrations of hydrogen-containing species in the oil and gas. Specifically, hydrogen sulphide compounds (*i.e.* H_2S) in the oil and gas react with the steel and diffuse into the steel,

preferentially attacking regions where coarse particles exist[4]. This causes severe degradation of mechanical properties of the pipeline steel, especially if the coarse particles are near (or, at) the surface of the pipeline which the fluid contacts. It is apparent that the failure of such an application could have potentially disastrous consequences to human life and the environment.

In the past decades, various authors and companies reported on coarse particles in HSLA steels. These coarse particles typically contain carbon, niobium, nitrogen, and titanium[5-9]. In this contribution it is intended to reveal the origin of these coarse particles in HSLA steels.

2 Problem Statement

In the literature, there are two hypotheses about the origin of coarse particles that are observed in the centreline region of microalloyed HSLA steels (see Table 1). The hypotheses will be discussed in the following sections.

Table 1 – Hypotheses about the origin of coarse particles observed in HSLA steel

Hypothesis	Pro	Contra
I. Particles form during solidification (mainstream theory)	Coarse particles may form if there are high concentrations of alloying elements in liquid steel	The concentrations of alloying elements are small; no evidence of macrosegregation of Nb/Ti
II. Particles exist before and during casting (recent conjecture)	Particles are released into the liquid steel and remain undissolved during casting	If particles dissolve quickly (usually, they do), they will not exist when casting begins

2.1 Coarse Particles Formed by Precipitation During Solidification

The first set of publications-which can be grouped under the first hypothesis-maintain that the particles formed due to segregation during solidification.

Chen *et al.*[5] observed large particles of nitrogen-rich (TiNb)(C,N) in Nb–Ti–V microalloyed HSLA steels; the major cause attributed by the authors to the presence of these particles was the addition of Ti to the steel which initiated the formation of TiN in the interdendritic liquid. As seen in Figure 3, the large particles have a dendritic morphology. In addition to these dendrites, cuboidal particles were also observed. These latter particles were believed to form in the liquid melt, or (most probably) during casting where significant segregation of Ti and N led to the formation of large TiN-rich cuboidal

precipitates. It should be noted that Chen *et al.* attributed the formation of these large particles to segregation, and not to the existence of thermally stable* phases inherited from ferroalloy additions.

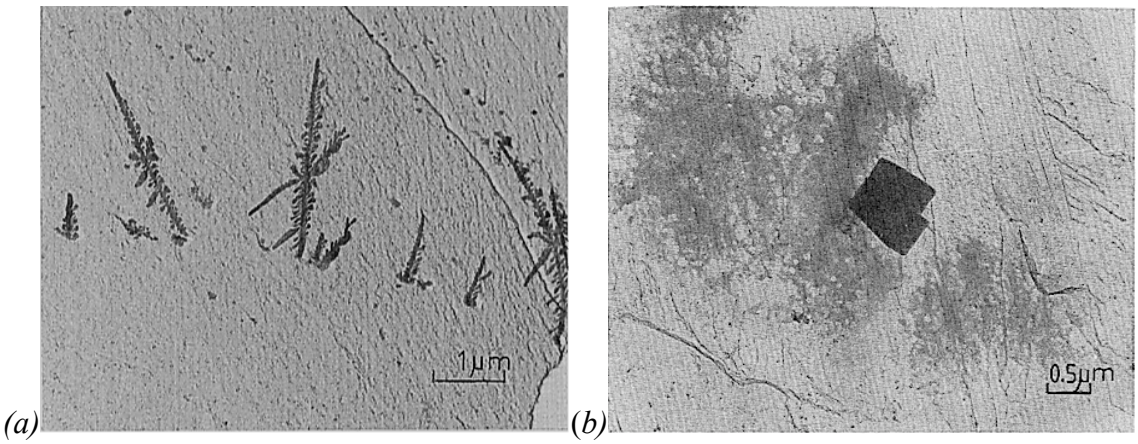

Figure 3 – *(a)* Coarse particles of (Ti,Nb)(C,N) with dendritic morphology and *(b)* TiN particle with cuboidal morphology[5]

Zhou and Priestner[9] investigated Nb-Ti-V HSLA steels with varying Ti concentration. Large Nb-rich particles that precipitated on MnS inclusions were observed in steels containing a concentration of Ti greater than a critical value (Ti > 0.012 wt. %). In all steel samples with less than that critical value of Ti, no carbonitrides were formed. However, with varying Ti and N concentrations, different compositions of these particles were observed, some Ti-rich, others Nb-rich. In addition, Ti-rich cuboidal inclusions were found in steel samples containing relatively high Ti concentrations.

* A thermally stable phase has a melting temperature above the temperature of liquid steel in a ladle, about 1600°C

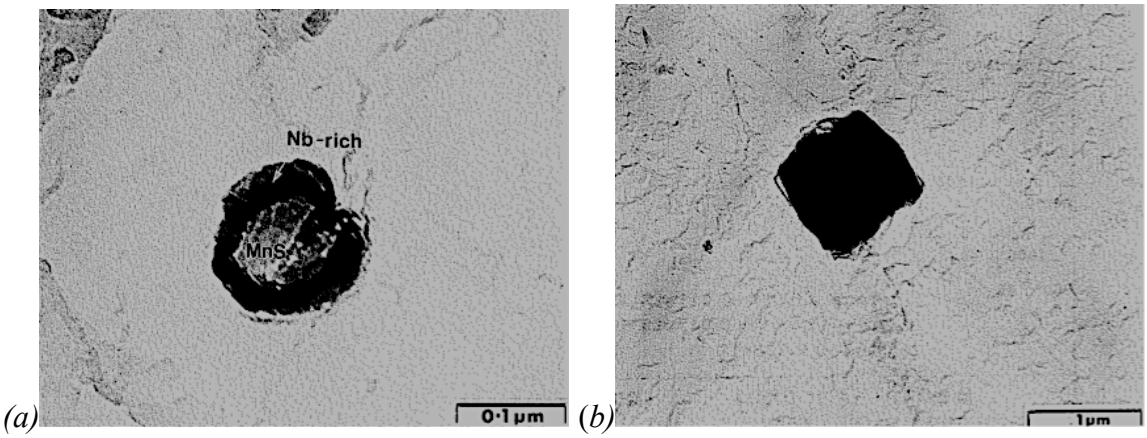

Figure 4 – *(a)* Nb-rich cap around an MnS core and *(b)* a TiN cuboid found in steels with high Ti concentration[9]

Zhuo *et al.*[7,8] investigated the segregation behavior in HSLA steels microalloyed with Ti and Nb. With respect to microsegregation in the interdendritic regions, nano-sized precipitates of (Ti,Nb)(C,N) have been observed. However, in the examined steel large (Ti,Nb)(C,N) precipitates were observed. The shapes of (Ti, Nb)(C, N) particles varied; some were cuboidal, while others were dendritic or irregular with different morphologies, sizes and compositions. It was shown that increasing the cooling rate transformed Ti-rich (Ti,Nb)(C,N) to Nb-rich (Ti,Nb)(C,N). In addition, the Nb-rich carbonitrides were typically smaller than the Ti-rich carbonitrides.

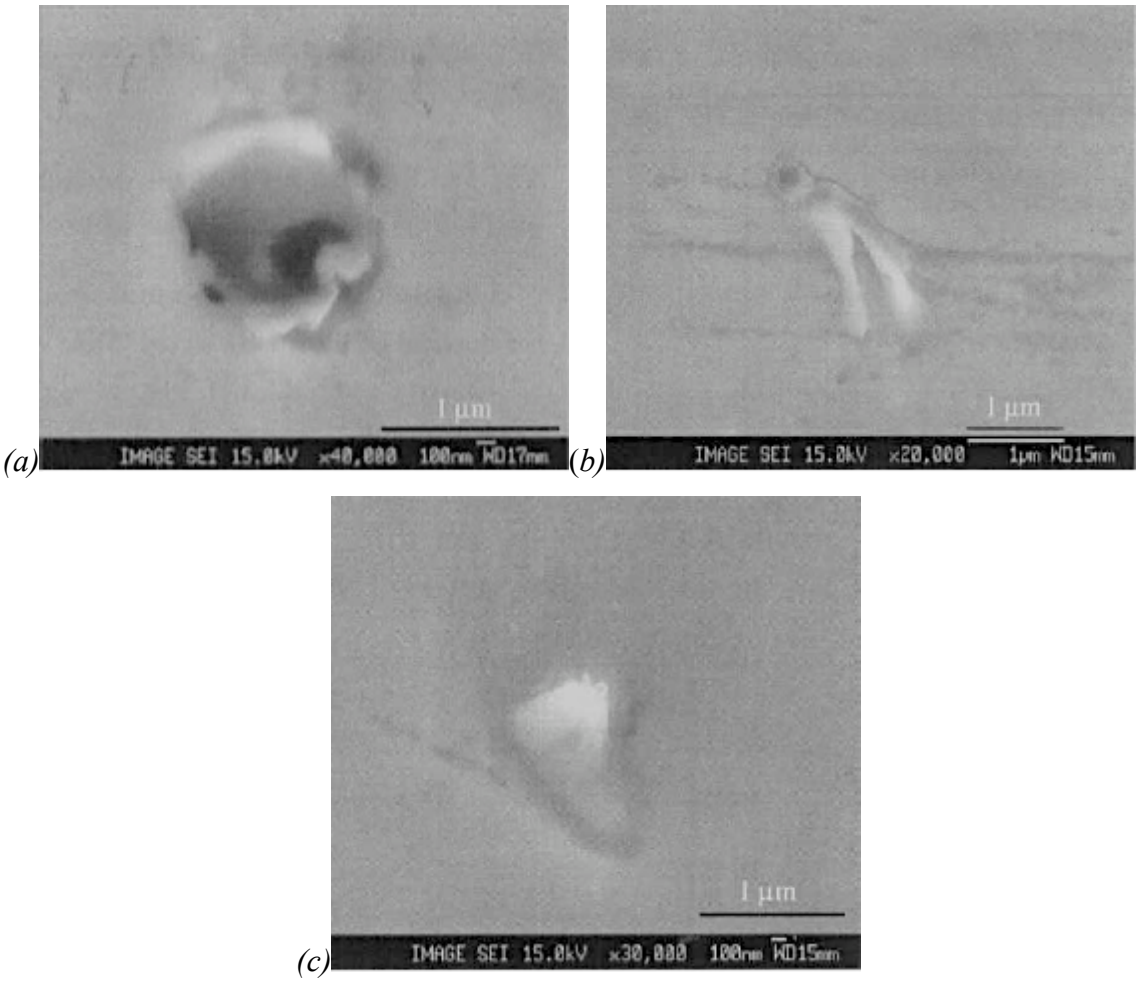

Figure 5 – Carbonitrides observed by Zhou with *(a)* cuboidal, *(b)* dendritic, and *(c)* irregular morphologies[7]

2.2 Coarse Particles Inherited From Ferroniobium Additions

The second set of publications-which can be grouped under the second hypothesis-speculate that coarse particles originate from the ferroalloy additions during ladle metallurgy. In other words, the coarse particles are released into the melt after the ferroalloy disintegrates and survive in the liquid long enough until casting. Since their

melting temperature is above ladle temperature, they will eventually-not necessarily quickly-dissolve in liquid steel.

Mendoza *et al.*[10] investigated the formation of coarse Nb-rich particles in a HSLA cast slab. It was suggested that the thermally stable phases in ferroalloys, specifically ferroniobium, remained undissolved during ladle metallurgy and were embedded in the steel matrix during casting. The centerline cracks were associated with the large particles near the centerline. Mendoza *et al.* analyzed the large particles and concluded that they were the Laves phase of the Fe-Nb system.

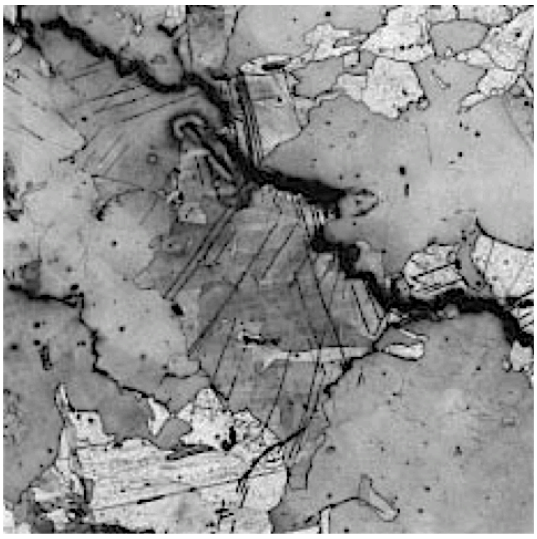

Figure 6 – Elongated particles associated with the Laves intermetallic phase from the Fe–Nb system[10]

Based on the work of Mendoza *et al.*, Abraham *et al.*[11,12] went further and suggested that the coarse particles observed in HSLA steels could be attributed to carbonitrides originating from ferroniobium. During the manufacturing of ferroniobium, the presence of impurities such as C and N combine with Nb, resulting in the formation of thermodynamically stable Nb(C,N). These coarse particles could remain undissolved

during ladle metallurgy and become trapped in the solidifying steel during casting. Based on previous research, it was proposed that these coarse particles could react with C, N and Ti in the steel and lead to the formation of (Ti,Nb)(C,N). Abraham *et al.*[11] suggested three routes in which the thermally stable phases could survive in liquid steel. First, these phases may originate from the ferroalloy addition. Second, these phases could react with components like C and N in the steel leading to the formation of carbonitrides. Third, these phases may precipitate from solution during solidification. Abraham *et al.* concluded by making two important statements. First, the non-stoichiometric composition of the coarse particles suggested that the particles did not form by a precipitation mechanism. Second, since these particles were observed in abundance near the centerline regions, it was suggested that they did not form by a segregation mechanism. Considering these statements, Abraham *et al.* proposed that these thermally stable phases existed in the liquid melt prior to solidification. Since they were large in size, it is possible that they avoided being trapped by the dendrite arms until the end of solidification.

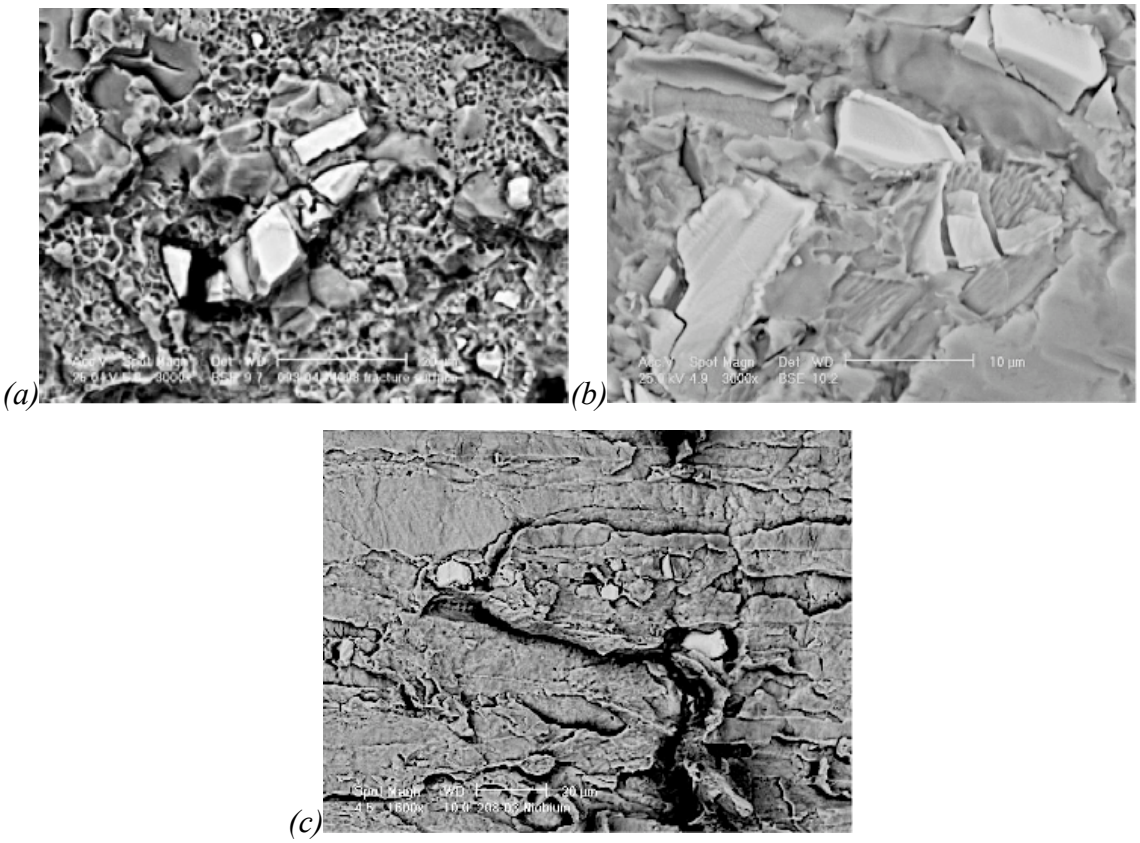

Figure 7 – Coarse particles: *(a)* Nb-rich, *(b)* Nb-rich along mid-thickness crack, *(c)* Nb/Ti-rich along mid-thickness crack[12]

2.3 Research Objectives

In this contribution, the second hypothesis given in Table 1 will be scrutinized, based on the conjecture of Abraham *et al.* Specifically, attention will be paid to the ferroniobium alloy since most coarse particles found in the HSLA steels contain Nb, and the formation of niobium carbides and carbonitrides in ferroniobium may occur due to their extreme thermodynamic stability. The microstructure of ferroniobium will be characterized and thermally stable phases will be identified. Furthermore, the experimental evidence of thermally stable phases will be compared with the results of

simulations by computational thermodynamics. Such simulations are useful to ferroalloy manufacturers and researchers as a predictive tool for ferroalloy phase portraits. The salient features of thermodynamic databases will be explored to give clarity on the usage of such predictive tools. Next, the dissolution kinetics of the thermally stable phases identified in the microstructure will be modeled and compared with results generated by commercial software (DICTRA). Finally, a sample of HSLA steel containing coarse particles will be investigated and characterized. In addition, clarity will be given on the speculation that macrosegregation may cause the formation of the coarse particles.

3 Literature Review

The discovery of niobium during the 19th century and its ability to enhance the mechanical properties of carbon steels was explored by metallurgists. However, sources of niobium were rare, driving its economic value upward resulting in a costly option for steelmakers. In the late 1950's, the discovery of niobium ore in Brazil and Canada provided an abundance of niobium for the steel industry, reducing the cost of producing steel with niobium additions. These events along with the societal demand for higher strength steels led to the research and production of HSLA steels[1].

The manner in which niobium is added to steel was also investigated to optimize the yield of niobium in the steel. Although several methods are currently employed to add niobium to liquid steel, such as niobium wire, pellets, and powder, the most common practice is additions of ferroniobium during ladle metallurgy. For this reason, the process of ferroniobium manufacturing will be reviewed to understand how the microstructure of ferroniobium is related to its manufacturing history.

3.1 Ferroniobium Manufacturing

The quality and size of the reserves of the niobium mine operated by CBMM gives this company the majority of the market share of ferroniobium production. For this reason, the manufacturing of niobium is considered from the process designed by CBMM[13]. To be sure, CBMM has evolved their manufacturing process over the past several decades, but for the past 15 years the process effectively remained the same.

The manufacturing process[†] begins with the extraction of niobium ore from the pyrochlore deposits. To produce ferroniobium, the pyrochlore deposits of the form $(Na,Ca)_2Nb_2O_6(OH,F)$ are pyrometallurgical refined. This process is used to remove poisonous elements such as P, Pb, and S in two consecutive steps: sintering and smelting in an arc furnace. The concentrates are pelletized with petroleum coke and bentonite[‡] and sintered, removing H_2O and S. The sintered pellets are crushed and fed to the electric arc furnace where they are combined with petroleum coke and steel scrap. The carbon from the coke reduces the phosphorus and lead oxides. The refined molten concentrate (*i.e.* Nb_2O_5) is tapped from the furnace at temperatures of 1450–1500°C and granulated by water; it is then sent to the aluminothermic reduction shop for ferroniobium production.

Although there are three possible methods to reduce niobium pentoxide, the most efficient is aluminothermic reduction. Since ferroniobium is used in steels, carbothermic reduction would result in a significant amount of carbides in ferroniobium, rendering the product useless for its intended application. Silicothermic reduction is inefficient since an incomplete reaction leads to the formation of other oxides of niobium. These oxides are difficult for silicon to reduce and are gathered in the slag, leading to considerable losses of niobium. Therefore, aluminothermic reduction is the industry-wide process used for ferroniobium production. The reaction is:

$$3Nb_2O_5 + 10Al = 6Nb + 5Al_2O_3 + 63{,}500 \text{ cal/atg Al (at 298 K)}$$

However, the energy evolved from this reaction is not sufficient to keep the bath in the liquid phase. For this reason, energy is added in the following form:

[†] It must be stated that only the relevant aspects of the process will be discussed.
[‡] An impure clay consisting mostly of montmorillonite (*i.e.* $(Na,Ca)_{0.33}(Al,Mg)_2(Si_4O_{10})(OH)_2 \cdot nH_2O$)

$$Fe_2O_3 + 2Al = Al_2O_3 + 2Fe + 104{,}850 \text{ cal/atg Al (at 298 K)}$$

This ensures that the ferroniobium is molten and can be separated from the slag easily for maximum niobium recovery. The melt exceeds a temperature of 2200°C in the converter and is held for more than 10 minutes to ensure separation of slag and metal. The molten ferroniobium is cast on a flat surface and cools in air. The as-cast structure is retained since the metal does not undergo any thermal treatments. A powerful hammer is used to break the ferroniobium in pieces and the different sizes are sorted and packaged for shipping (Figure 8). The capacity of the manufacturing plant at CBMM for niobium product is given in Table 2.

Figure 8 – A sample of standard grade ferroniobium produced by CBMM

Table 2 – Niobium products and capacities produced at CBMM

Products	wt. % Nb	Capacity (tons/year)
Ferroniobium (standard grade)	65–67	45,000
Niobium oxide (high purity)	99	3,000
Ferroniobium (vaccum grade) and nickel niobium	65–67	1,500
Niobium oxide (optical grade)	99.9	150
Niobium metal	99.9	60

3.2 Binary Fe–Nb Phase Diagrams

In previous works, there exists an abundance of binary phase diagrams for the Fe–Nb system. Although the thermodynamic details will not be exhausted in this contribution, it suffices to present a majority of the available Fe–Nb phase diagrams consisting of two types: optimized (or, assessed) and experimentally calculated. In general, all Fe–Nb diagrams contain two intermetallic phases, the Laves (ε) and μ-phase. However, on the Nb-rich side of the phase diagram, there are significant discrepancies in the phase boundaries of intermetallic phases (Figure 9). For example, the μ-phase differs in how it fuses in two ways: congruently or peritectically (compare Figure 9 with Figure 10, Figure 11 and Figure 12).

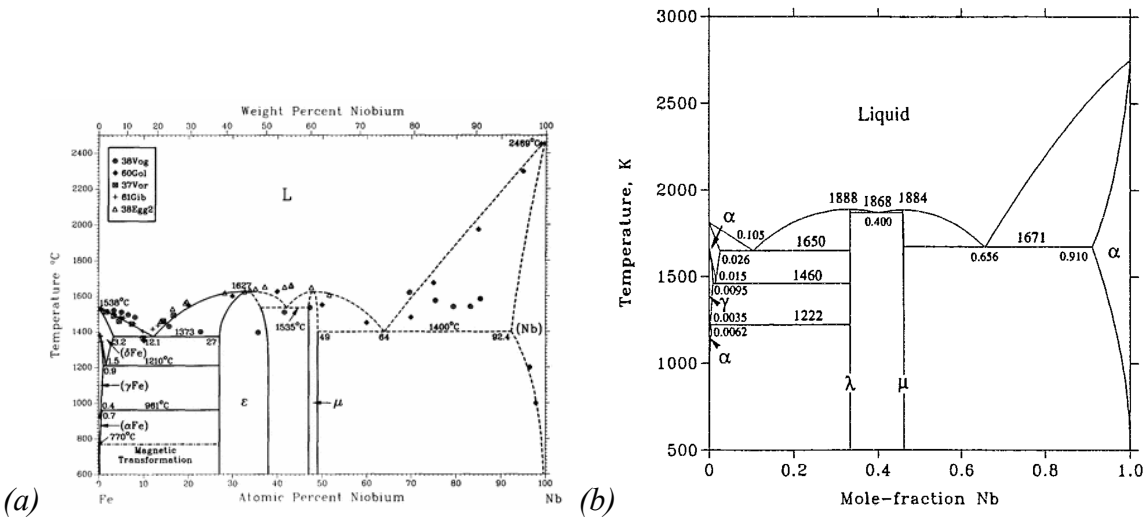

Figure 9 – The Fe–Nb phase diagrams publish by *(a)* Paul *et al.*[14] and *(b)* Huang[15]

Another discrepancy is that the existence of the Fe_2Nb_3 (η) phase in the Fe–Nb system varies between publications. This phase has been experimentally identified and used in thermodynamic assessments of the Fe–Nb system. It is worth mentioning that most assessments and experimental works do not acknowledge the existence of the η-phase in the binary Fe–Nb system. The only work to experimentally corroborate the presence of the η-phase in the binary Fe–Nb system was by Bejarano *et al*[16] (Figure 10). This phase was described as "metastable" and certain conditions were necessary to cause stabilization of this phase. In particular, specific conditions of cooling and/or the presence of O and N may cause this phase to stabilize. An x-ray study by Bejarano *et al.*[17] confirmed the metastability of the η-phase due to slow cooling kinetics during DTA experiments.

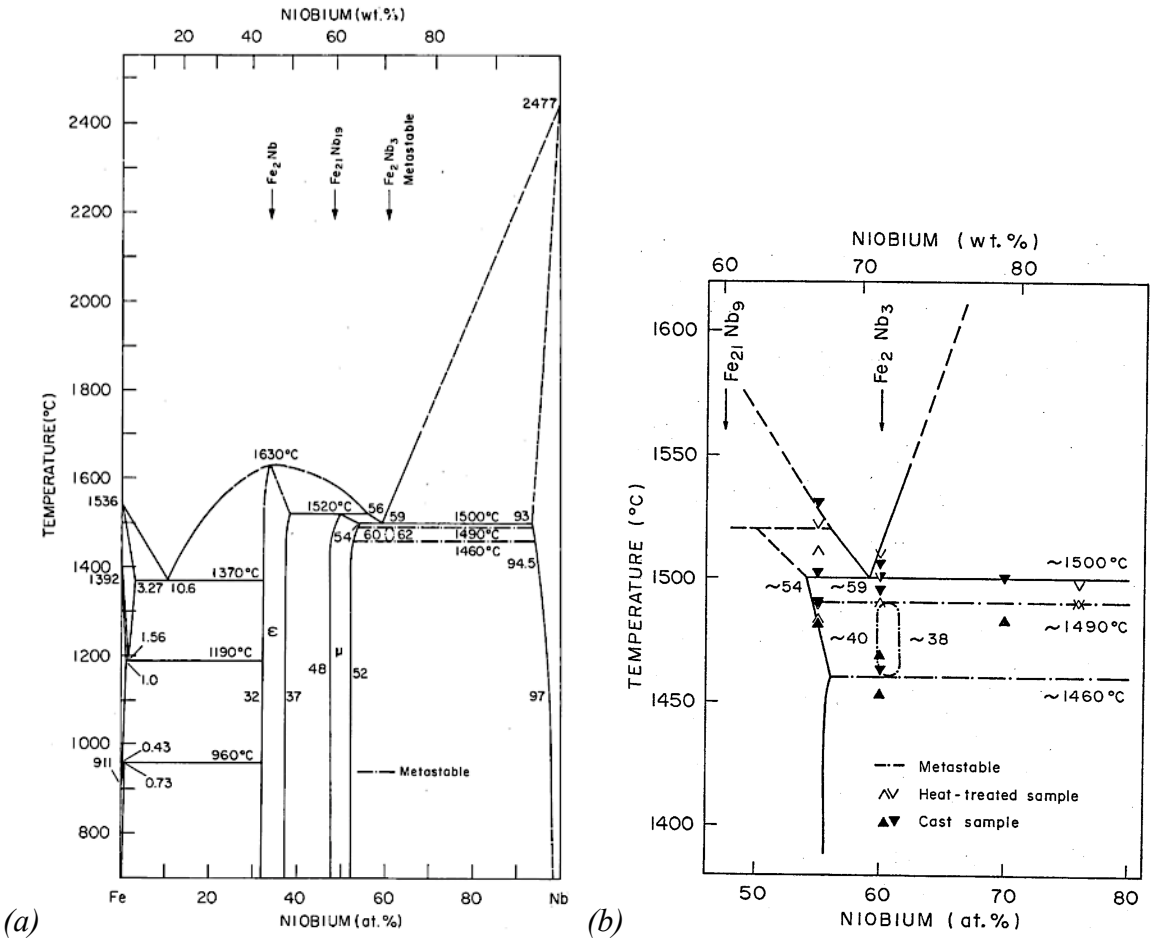

Figure 10 – *(a)* The Fe–Nb phase diagram proposed by Bejarano *et al.*[18] and *(b)* the metastable phase Fe_2Nb_3[16]

In the past two years, three comparable Fe–Nb phase diagrams have been published. The first is an experimental phase diagram by Voss *et al.*[19] (Figure 12) who established phase equilibria using EPMA and DTA measurements, while the two most recent diagrams by Khvan *et al.*[20,21] (Figure 13) are assessments produced due to discrepancies observed in the phase diagrams of multicomponent systems such as Fe–Mn–Nb–C, Fe–Mn–Nb–N and Nb–C–N. It should be noted that the most recent

assessments compare well with the assessment by Toffolon *et al.*[22] (Figure 11) and the experimental phase diagram determined by Voss *et al*.

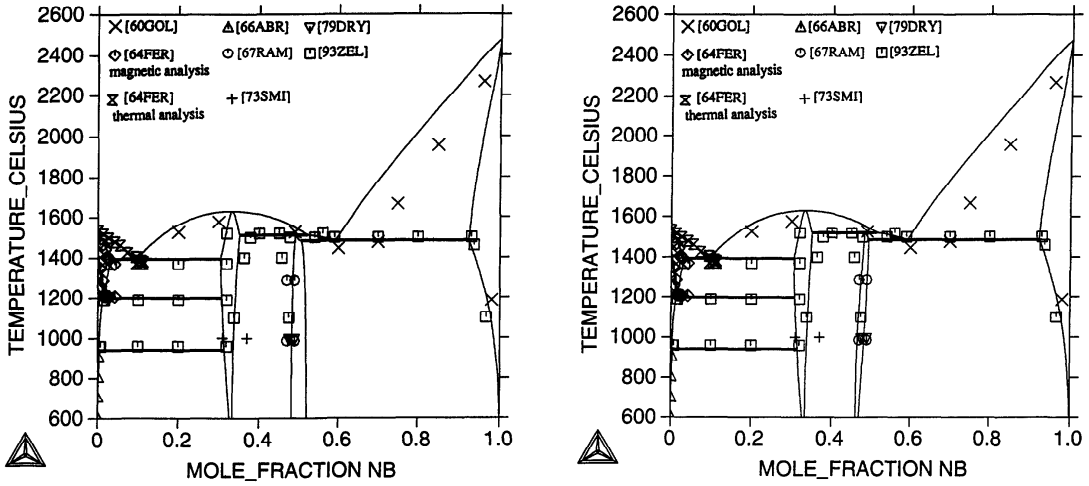

Figure 11 – The Fe–Nb phase diagram assessed by Toffolon *et al.* with the µ-phase having *(a)* 3 sublattices and *(b)* 4 sublattices[22]

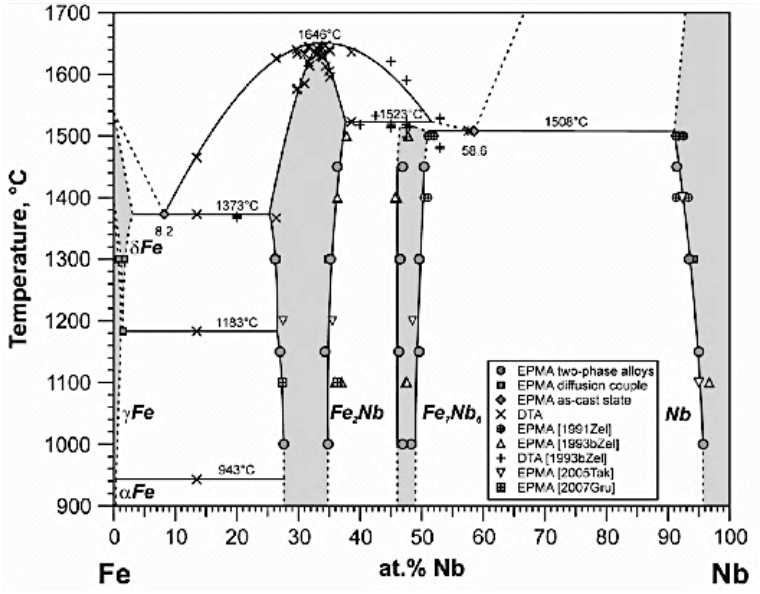

Figure 12 – The Fe–Nb phase diagram experimentally determined by Voss *et al.*[19]

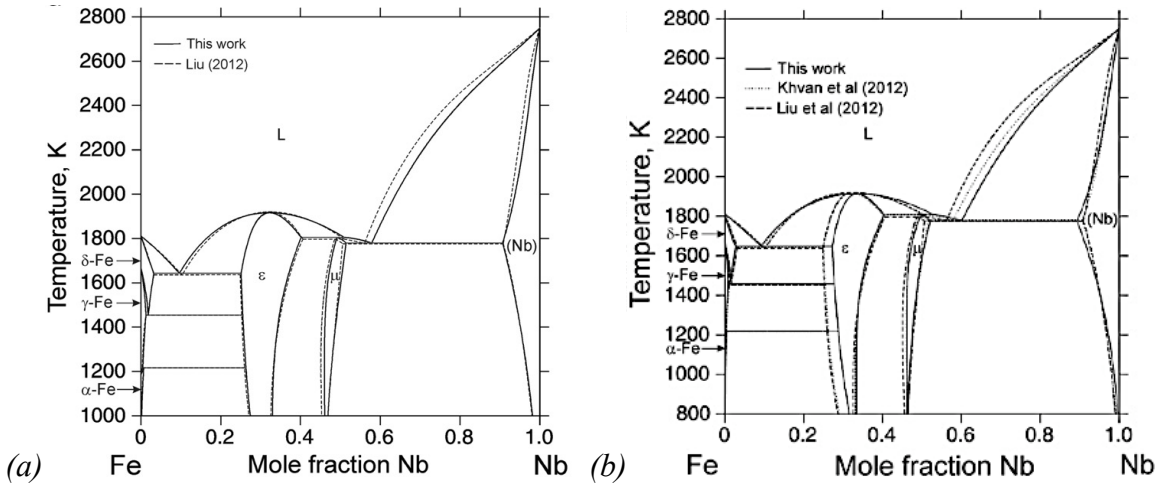

Figure 13 – Assessed Fe–Nb phase diagrams by *(a)* Khvan *et al.*[20] and *(b)* Khvan *et al.*[21]

In conclusion, the Fe–Nb phase diagram has been developed with a more accurate thermodynamic description in the most recent assessments, and is supported with an experimental confirmation of the phases, particularly on the Nb-rich side of the phase diagram. This clarity on the variety of different Fe–Nb phase diagrams will prove useful to those who are performing thermodynamic calculations (*i.e.* ferroalloy manufacturers, researchers, *etc.*). However, thermodynamic databases must be updated with the most recent thermodynamic data of the Fe–Nb system so that the predictions of microstructure, phase fractions, liquidus temperatures and other useful data can be relied upon.

3.3 Microstructure of Ferroniobium

The microstructures of binary Fe–Nb alloys have been published by various authors, usually those who are experimentally determining phase equilibria for the Fe–Nb binary system. One such example is Voss *et al.*[19] who experimentally determined the homogeneity range and peritectic melting of the μ-phase. In this case, the use of 99.95%

pure Fe and 99.9% pure Nb gives a truly representative microstructure in the Fe–Nb system (Figure 14). From this perspective, such micrographs are not representative of the microstructure of commercially manufactured ferroniobium, since the impurity levels are significantly higher in them. For this reason, a distinction is made in this contribution between ferroniobium, and Fe–Nb; the former referring to the commercial product, and the latter referring to the binary system.

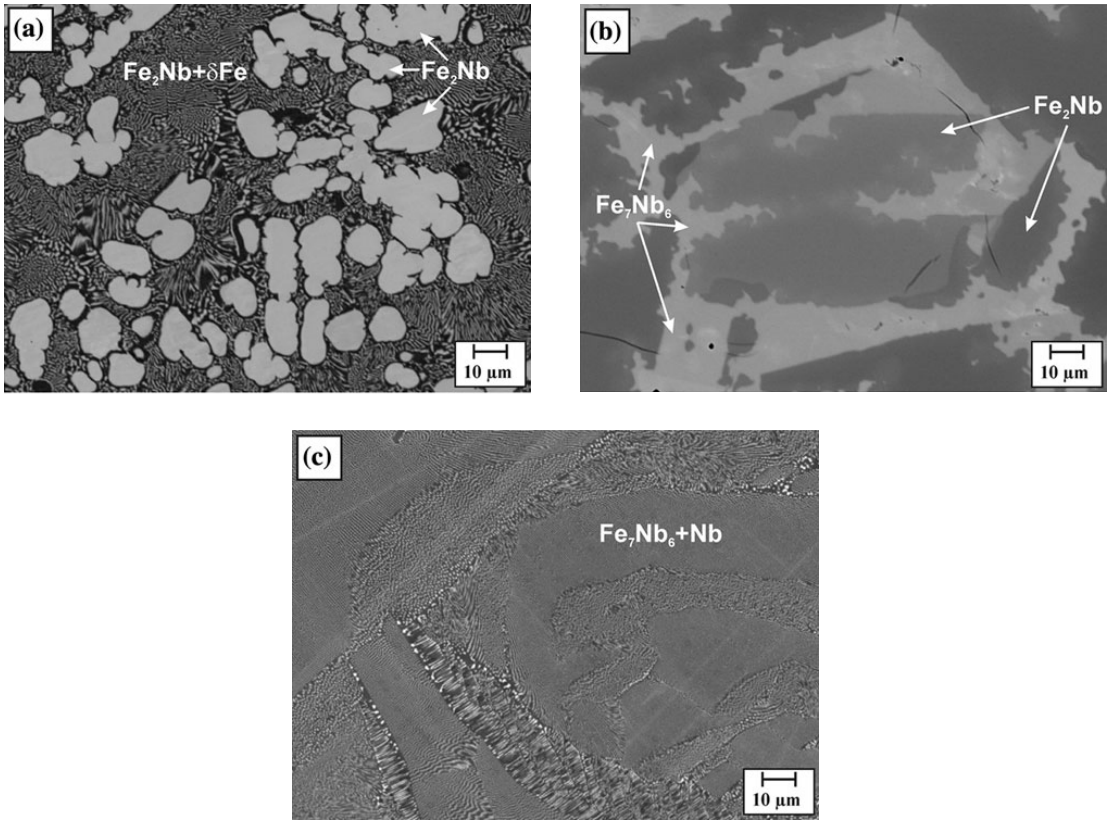

Figure 14 – Microstructures of Fe–Nb alloys that reveal the intermetallics of ε- and µ-phase, and the solid solutions of δFe and Nb[19].

Few publications document the microstructures of ferroniobium and the effect of impurities on their phase portraits. The microstructures that are concerned with commercial ferroniobium are reviewed from two publications. Raman *et al.*[23] noticed a

significant fraction of η-phase present in commercial ferroniobium and Bejarano *et al.*[17] demonstrated that its stabilization could be attributed to either specific cooling conditions or impurity levels. Therefore, in this contribution the examination of the microstructure of commercial grade ferroniobium is of importance to determine if any thermodynamically stable phases exist (*e.g.* carbides or carbonitrides).

The phase portrait of a commercial ferroniobium alloy was investigated by Abraham *et al.*[11,12] by characterizing the phases and their compositions. Their hypothesis that liquid steel inherits carbides and carbonitrides from the ferroniobium must be substantiated with an undeniable proof of their existence in ferroniobium. The examination of the microstructure of a ferroniobium alloy caused Abraham *et al.* to conclude that only two phases existed in it: the μ-phase and the Nb solid solution phase. It must be noted that, although carbon was present in the niobium ferroalloy (0.83 wt. %), no carbides were detected in the analysis. In addition, the presence of impurities and/or solidification conditions did not appear to stabilise the η-phase, since it was not observed. During solidification of this alloy, the μ-phase forms as a primary phase with varying composition, until the eutectic temperature is reached at which point the μ + Nb eutectic forms. Since the overall composition of Nb is close to the eutectic, the fraction of eutectic is quite high (see Figure 15).

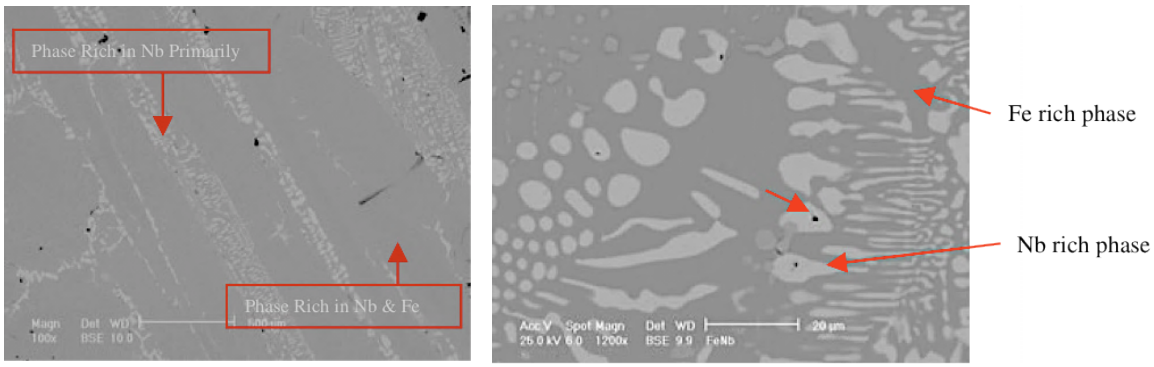

Figure 15 – The microstructure of a commercial grade ferroniobium alloy

3.4 Dissolution of Ferroniobium Alloys

The dissolution kinetics of ferroniobium and its alloys is reviewed from the literature to determine if the kinetics of dissolution of any thermally stable phases were determined. A literature search revealed an abundance of publications on on the kinetics of dissolution of ferroniobium, and its alloys. For convenience, it is useful to divide the publications on ferroniobium dissolution into two groups (Table 3). In the first category, the melting/dissolution of ferroniobium is examined by considering its overall (or, net) composition and corresponding liquidus temperature. The second group examined the kinetics of melting/dissolution from a truly binary perspective by taking into account the phase portrait of ferroniobium and thermally stable phases in the binary Fe–Nb system. It should be noted that all thermally stable phases were related to the binary Fe–Nb system, and carbides/carbonitrides were never mentioned.

Table 3 – The publications on dissolution kinetics of ferroniobium

Group	Perspective on Dissolution Kinetics of Ferroniobium	References
1	Total composition	24-26
2	Thermally stable phases	27-30

In the early stages of measuring the kinetics of incorporating ferroalloys into liquid steel, a categorization of ferroalloys was made to differentiate between their assimilation into liquid steel by either melting or dissolution. Ferroalloy additions in steelmaking were classified in two categories: class I ferroalloys having melting temperatures below that of liquid steel in a ladle, and class II ferroalloys with melting temperatures above liquid point.

Class I ferroalloys assimilate into the liquid by melting. Examples of class I ferroalloys include ferromanganese, silicomanganese, ferrochrome and ferrosilicon. Argyropoulos *et al.*[24] proposed four possible routes how this assimilation could occur. Routes 1–4 refer to additions have melting temperatures below liquid steel, while Route 5 considers additions with melting temperatures above the liquid point. In all cases, a solid steel shell freezes (B) around the object immediately following immersion into the liquid (A). The simplest yet most common case is shown in route 1 (Figure 16), where the shell still surrounds the ferroalloy lump while the lump begins to melt (C). The ferroalloy is molten before the shell has melted back into the liquid (D). The rate at which the shell melts back depends on heat transfer kinetics and fluid dynamics of the bath. However, routes 2,3 and 4 are also possible. These routes depend on the thermal properties of the

alloy, the addition's size, and the composition and temperature of the steel bath. The second route considers the case where the steel shell is assimilated back into the liquid (C). Subsequently, the bare ferroalloy is exposed to the liquid steel and melts (D). This is often the case for ferroalloys that have been preheated, or heated by the warm steel shell; the ferroalloy is not sufficiently cool to form another solid steel shell on the surface. It follows from this second route, that if the core of ferroalloy is not heated enough, a third scenario may occur. The ferroalloy may partially melt beneath the steel shell (C). Once the ferroalloy is re-exposed to the liquid steel, the portion of molten ferroalloy will be released into the liquid. If the ferroalloy is large, a second steel shell may form on the surface of the ferroalloy (D) since the core of the ferroalloy is cool. Route 4B shows the case where ferroalloys have high exothermic heats of dissolution in liquid steel (*i.e.* exothermic reaction near the steel shell/ferroalloy interface forms liquid eutectic and heat is released). This phenomenon may shorten the period of time for the steel shell to encase the ferroalloy and enhance the melting/dissolution rate of the ferroalloy. It should be noted that this route is applicable to class I and II ferroalloys.

Class II ferroalloys assimilate into the liquid bath via a "true" dissolution process, which is governed by diffusion of solute material through a boundary layer into the liquid bath. Examples of class II ferroalloys include ferrovanadium, ferrotungsten, ferromolybdenum, and ferroniobium. The mechanism for the dissolution of class II ferroalloys can be described most commonly by route 5. Once the steel shell melts back (C), the solid will be exposed and its temperature will equilibrate with the surrounding

liquid. The melting temperature of the solid is higher than the liquid so the ferroalloy dissolves into the bath.

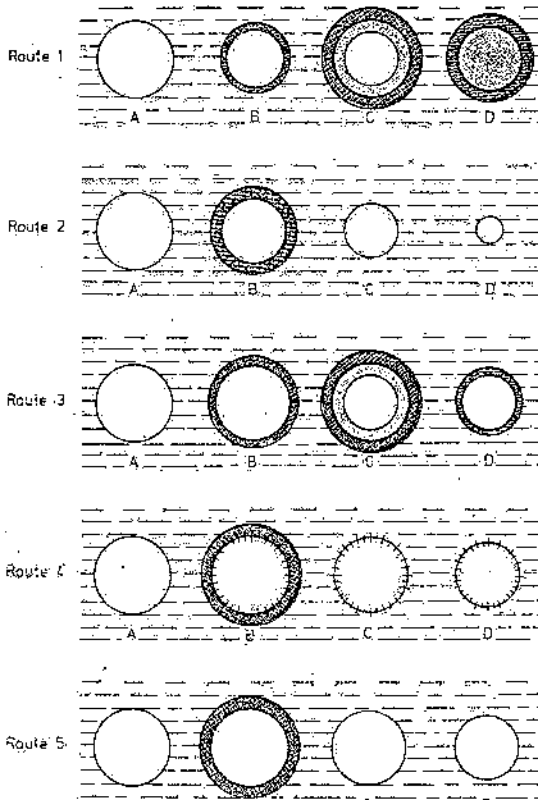

Figure 16 – The possible routes of assimilation of alloys into liquid steel from Argyropoulos

Since this contribution is focussed on ferroniobium due to previously mentioned reasons (page 11), a review on the dissolution kinetics is also restricted to this particular ferroalloy. In all publications, the authors used models, experiments, or a combination of these to describe the kinetics of dissolution.

3.4.1 Kinetic Studies Considering the Overall Composition of Ferroniobium

In the first category, a publication by Argyropoulos *et al.*[24] proposed a model to predict the dissolution times of class I and class II ferroalloys. For the case of

ferroniobium, which is a class II ferroalloy, the model calculated the dissolution times of two types of Nb alloys: 65 wt. % Nb and pure bcc Nb. The dissolution rates of the two types were compared, and the time to complete dissolution was calculated for natural and forced convection conditions. It is important to note that these dissolution times *included* the steel shell freezing and melting back, approximated to 1% of the total dissolution time by the authors. Based on the results, Argyropoulos *et al.* emphasized the importance of stirring (forced convection conditions) in industrial processes. This was given a quantified by developing velocity field predictions in an idealized furnace tapping operation. The predicted flow fields generated by argon stirring in a 250 ton ladle is shown in Figure 17 with velocities ranging from 0.1–1.25 m/s.

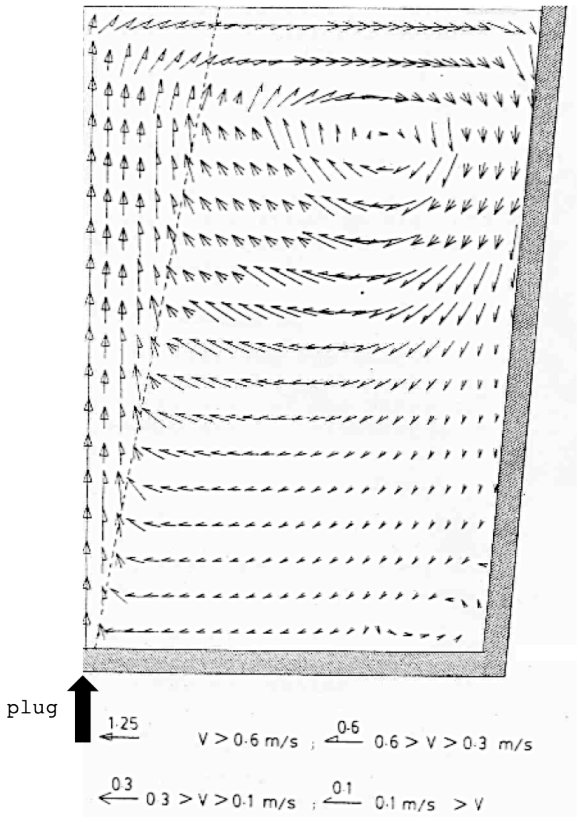

Figure 17 – Predicted velocity profile generated by argon stirring in a 250 ton cylindrical ladle from a centrally located porous plug[24]

In a subsequent publication, Argyropoulos [25] experimentally measured the dissolution characteristics of ferroalloys in liquid steel using a microprocessor-based system connected to a load cell (Figure 18). The steel was inductively melted and the steel bath was deoxidized prior to immersing ferroalloy lumps in the liquid. The ferroalloy was attached to the load cell and the change in weight was recorded. The continuous measurement recorded by the load cell included the formation of steel crust, and subsequent melt-back, and dissolution of the ferroalloy. Argyropoulos *et al.* selected industrial grades of ferrosilicon, ferrovanadium and ferroniobium to be used in the experiments. Two types of tests were carried out: first, the power input to the induction furnace was turned *off* during the immersion period to simulate natural convection conditions; second, the power input was turned *on* (*i.e.* induction stirring) during the immersion period to simulate forced convection conditions.

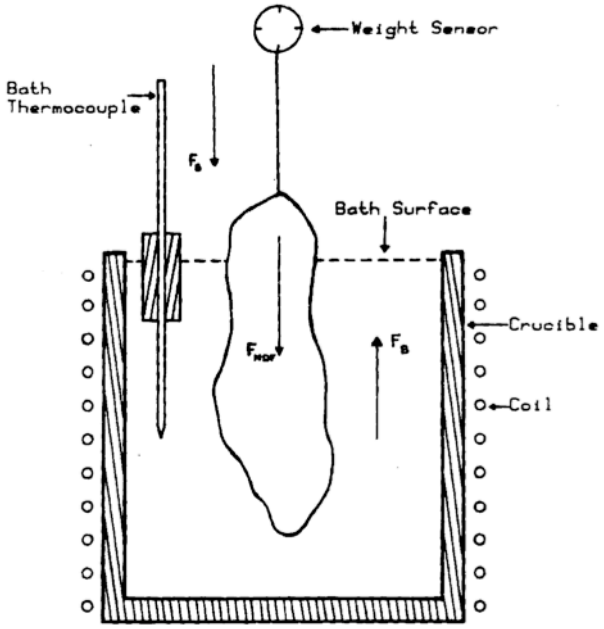

Figure 18 – A schematic of the load cell configuration and crucible set-up[25]

Under forced convection conditions, the velocity of the liquid steel flowing around the ferroniobium lumps was calculated to be 0.1 m/s.

The dissolution rates of two types of ferroniobium were measured: high purity grade, and standard (commercial) grade. The mass transfer rates of high purity grade ferroniobium were faster than standard grade ferroniobium. This difference was attributed to the exothermic reaction with liquid iron for high purity grade ferroniobium and standard grade ferroniobium. High purity grade ferroniobium was calculated to have a larger partial heat of mixing with liquid iron, and therefore faster dissolution times. Standard grade ferroniobium, which contained a few weight percent of Al and Si as impurities in the alloy originating from the manufacturing process, had a lower partial heat of mixing with liquid iron and slower dissolution kinetics. He used the model from a previous work[24] to include this exothermicity and predicted the dissolution times of high purity grade ferroniobium for natural and combined natural and forced convection conditions (Figure 19).

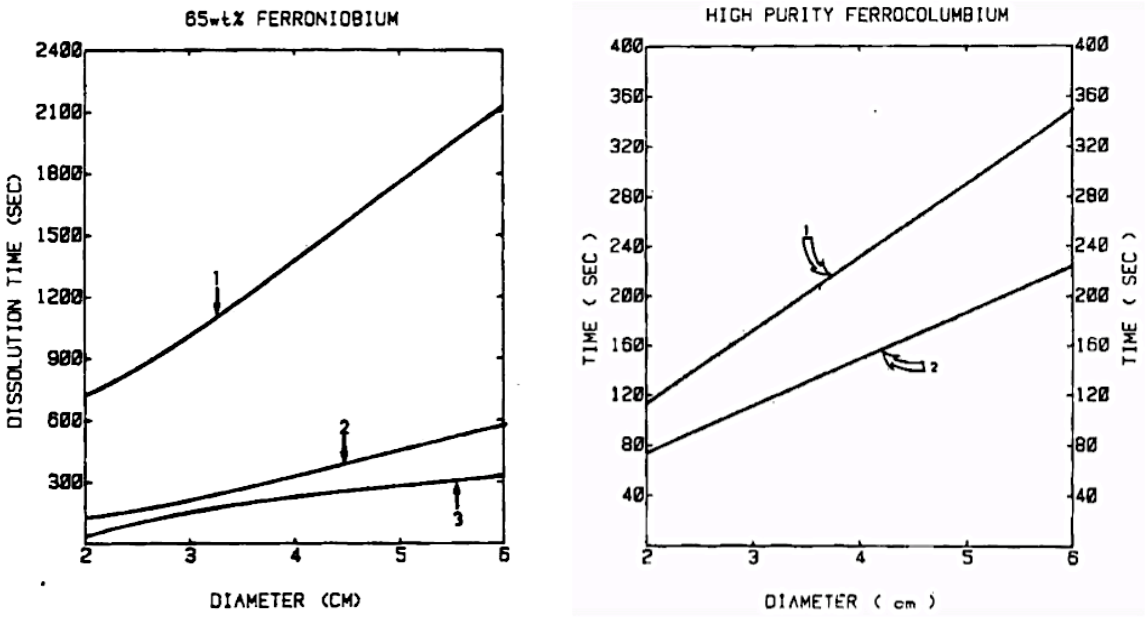

Figure 19 – Dissolution of two types of ferroniobium alloys at 1600°C; *(a)* curve 1: natural convection, combined natural and forced convection for curve 2 (v=0.1 m/s) and curve 3 (v=0.3 m/s); *(b)* curve 1: natural convection, curve 2: combined natural and forced convection (v=0.1 m/s)[25]

The last work dedicated to the dissolution of ferroalloys from the first group was from Sismanis *et al.*[26]. The dissolution of Nb, B, and Zr ferroalloys in liquid steel and liquid iron were determined both experimentally and theoretically. In addition, the effect of dissolved oxygen in the liquid melts on the dissolution kinetics was revealed. The rate of dissolution was monitored experimentally through the use of a load cell, thermocouple and data acquisition process control (DPAC) system.

In the theoretical model, the mass flux was considered for the case where the ferroalloys were class II alloys. It was assumed that the irregular geometric lumps were idealized spheres that contained the same volume as the lumps. The dissolution rates for high purity and standard grade ferroniobium alloys were measured. The predicted dissolution times for high purity ferroniobium in steel bath were reported for natural and forced convection conditions. The effect of oxygen was not incorporated into the model.

The experimentally determined mass flux for high purity ferroniobium was reported as 0.69 kg/m^2/s (natural convection) and 1.12 kg/m^2/s (forced convection). The predicted dissolution time and experimental mass flux for standard grade ferroniobium in a steel bath was not reported.

In another experiment, the dissolution rate of standard grade ferroniobium in a *cast iron* melt was experimentally measured and compared with model predictions. The mass transfer rate calculated from experiments for a bath temperature of 1400°C was 0.04 kg/m^2/s under natural convection conditions. Based on these results, the dissolution of a spherical standard grade ferroniobium alloy was modeled and predicted long dissolution times (Figure 20). An explanation for the effect of carbon in the melt on such a lengthy dissolution time was not provided.

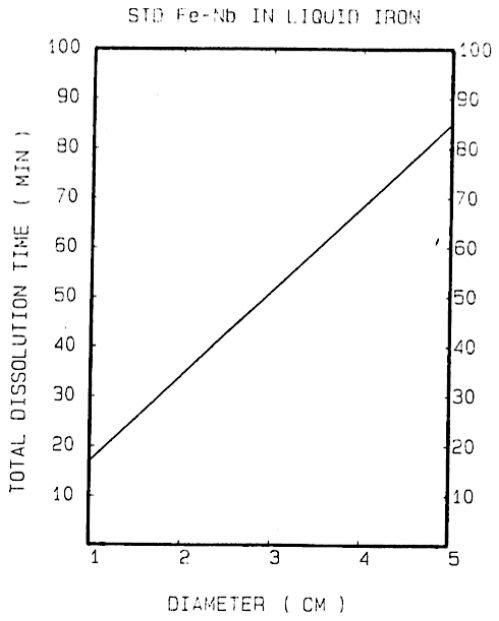

Figure 20 – Predicted dissolution times of standard grade ferroniobium lumps in liquid cast iron (3.5 wt. % C)[26]

3.4.2 Kinetic Studies Considering Thermally Stable Phases in Ferroniobium

The second group of authors acknowledged the effect of phase portrait in the ferroniobium alloy on the dissolution kinetics. The first author to publish a paper in this regard was Argyropoulos[27], who examined the effect of microexothermicity and macroexothermicity on the dissolution kinetics of select ferroalloys. The term microexothermicity refers to the release of heat due to the formation of an intermetallic compound at the interface of the ferroalloy and liquid steel. This type of exothermicity is usually observed when a powder alloy compact is submerged in liquid steel. On the other hand, macroexothermicity refers to heat released when a ferroalloy is dissolved into liquid steel - often associated with the partial heat of mixing of a ferroalloy due to the large ratio of liquid steel to metal. The degree of macroexothermicity decreases with increasing amounts of iron in the ferroalloy[§].

In this publication, the intermetallic Laves phase (Fe_2Nb) was fabricated by mixing iron powder and iron-niobium powder. Specifically, a cylinder of ferroniobium powder with 69 wt. % Nb was combined with sufficient iron powder and pressed to form a pellet[**]. The iron addition was intended to lower the niobium concentration and modify the overall composition to be similar to the Laves phase composition. Upon immersing the pellet in liquid steel, the total enthalpy increased corresponding to an increase in temperature of the pellet past its liquidus temperature of 1650°C; this increase in enthalpy was attributed to microexothermicity, specifically the formation of the Laves phase. The

[§] That is, ferroniobium with 80 wt. % Nb has a higher degree of macroexothermicity than a 50 wt. % ferroniobium alloy
[**] This powder is called a modified ferroniobium compact because iron powder was added

experiments showed that the modified ferroniobium compact dissolved rapidly and the main cause of this fast dissolution was attributed to microexothermicity.

Furthermore, a model was used to predict dissolution behaviour for microexothermic spheres of ferroniobium. The model predicted rapid dissolution kinetics for a ferroniobium microexothermic sphere in a liquid steel bath at 1600°C (Figure 21); the dissolution rate was faster for the modified ferroniobium compact than for commercial ferroniobium alloys.

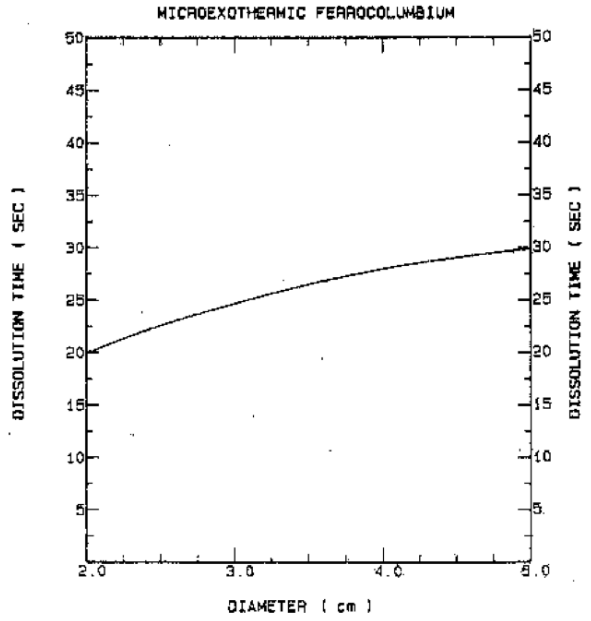

Figure 21 – Dissolution model predicting the kinetics of a microexothermic ferroniobium sphere in liquid steel[27]

The macroexothermic behaviour was modeled for two types of ferroniobium alloys: standard grade and high purity grade. It should be noted that no experimental work was performed for macroexothermic ferroniobium to corroborate the predictions of the model. The macroexothermic behaviour is expected to exist for standard grade ferroniobium, since it has a total of 6 wt. % of Si and Al impurities. These impurities are

supposed to have two effects: first, the silicon content (2.5 wt. %) was supposed to form $NbSi_2$, which has a high melting point (actually, this small amount of silicon does not stabilise the formation of $NbSi_2$); second, the impurity contents are expected to reduce the partial heat of mixing. For this reason, the high purity grade ferroniobium is expected to dissolve faster than the standard grade ferroniobium (Figure 22).

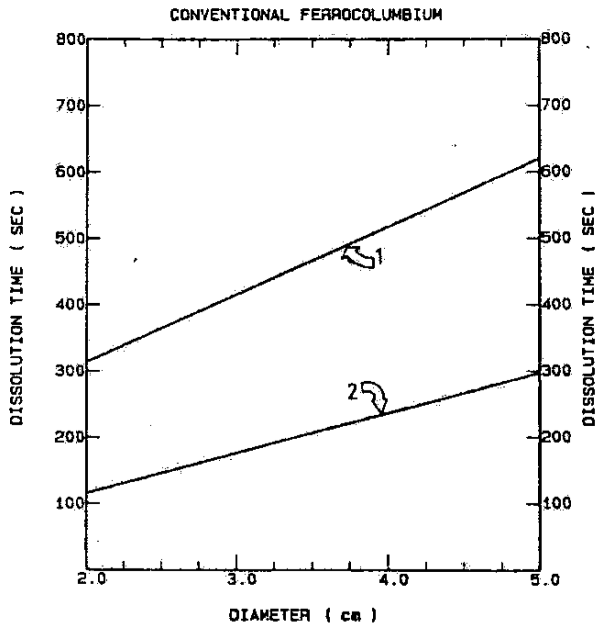

Figure 22 – The model results for dissolution of standard grade (curve 1) and high purity grade (curve 2) ferroniobium in liquid steel[27]

The second work in this group of publications came from Gourtsoyannis *et al.*[29]. In that paper, the dissolution rates of niobium and molybdenum metals and Ni- and Mo-ferroalloys in steel baths was experimentally determined. It was shown that metallic niobium dissolves faster than molybdenum, while the conditions are reversed for their respective ferroalloys. This effect was attributed to the macroexothermic mixing of Nb with liquid Fe (Figure 23).

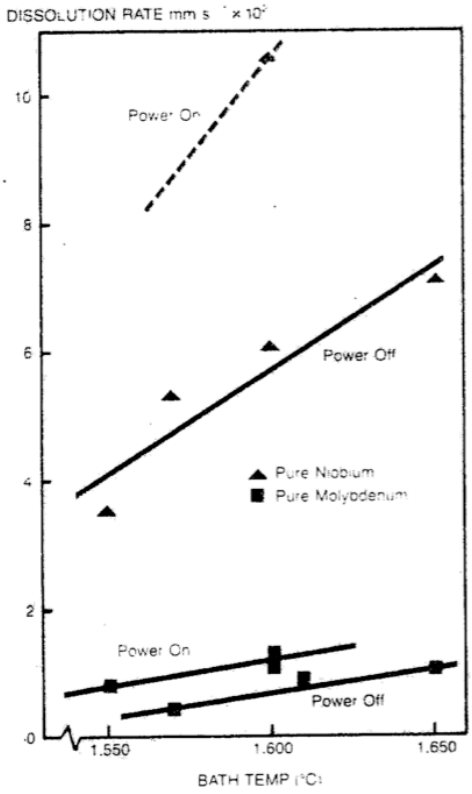

Figure 23 – Dissolution kinetics of niobium rods in liquid steel[29]

A standard grade Fe–66Nb alloy was assumed to contain the thermally stable phase (Laves) whose liquidus temperature is around 1650°C. The dissolution rate of this ferroniobium alloy would presumably increase when the temperature was in the vicinity of 1650°C. To confirm this, two ferroniobium alloys were fabricated: 50 and 73 wt. % Nb. The 50 wt. % Nb alloy contains a considerable fraction of Laves phase while the 73 wt. % Nb alloy does not contain Laves phase at all. The dissolution rates of these two alloys in a steel bath were measured, and the results clearly show the increase in dissolution rate of the 50 wt. % Nb alloy, while the dissolution rate of the 73 wt. % Nb alloy is reported as sluggish (Figure 24). An explanation for this sluggish behaviour was

not provided. The Fe–Nb phase diagram implies that a significant fraction of bcc Nb would exist in the ferroalloy, which may have an effect on the dissolution rate.

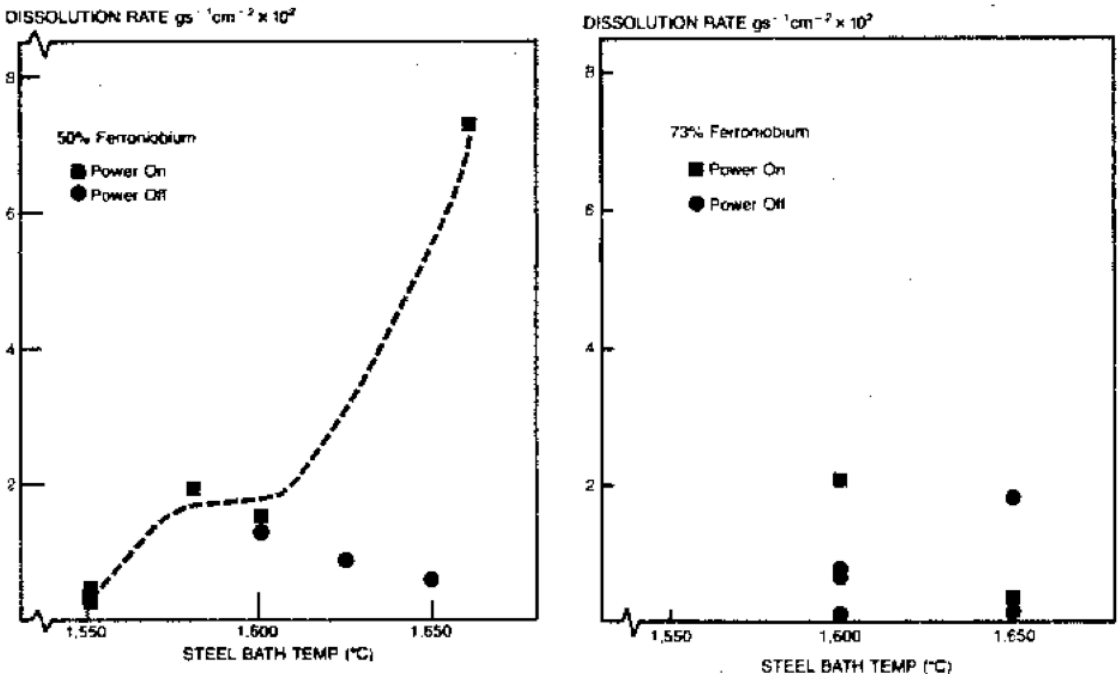

Figure 24 – Dissolution of 50 wt. % Nb and 73 wt. % Nb alloys in liquid steel[29]

In addition, industrial applicability was discussed regarding the dissolution rates of ferroalloys. In particular, based on the work of Dr. Tanaka, the predicted velocity profile in the ladle was determined to have a range of 0.1–0.6 m/s. For natural convection baths, the dissolution rate of pure Nb at 1600°C is experimentally extrapolated to be 3.6 mm/min. In forced convection baths, the dissolution rate of pure Nb at 1600°C is experimentally extrapolated to be 6.5 mm/min.

Another publication in the second group was written by Sismanis *et al.*[30]. The exothermic dissolution of cylindrical specimens of Zr, Ti, and Nb in liquid steel was modeled and compared with experiments. The model included the time of the steel shell

period and subsequent dissolution of the metallic addition, including exothermic reactions. Thus, mass and heat transfer equations were used to model the disintegration of ferroniobium alloys. The model also accounted for the cases of natural convection and forced convection. The model assumed that there was no mass or heat flux in the axial dimension of the cylinder (*i.e.* that flux operated in the radial direction only).

It was acknowledged that reactions could happen at the Nb/Fe interface during the steel shell period, such as the formation of intermetallics like Fe_2Nb and Fe_2Nb_3. However, no intermetallics were observed at the interface since the temperature of formation needed to be at least 1370°C according to the Fe–Nb phase diagram. This temperature may not have been reached prior to the final stages of the steel shell period. For this reason, the ferroalloy may not form intermetallics at the interface between solid ferroalloy and solid steel shell; instead, it would dissolve in the liquid steel. A typical outcome of a niobium dissolution experiment is presented in Figure 25; curve 1 refers to the measured steel bath temperature, while curve 2 registered the net downward force of the cylinder in the melt. Curve 3 measured the centreline temperature of the niobium cylinder, while curve 4 predicted it.

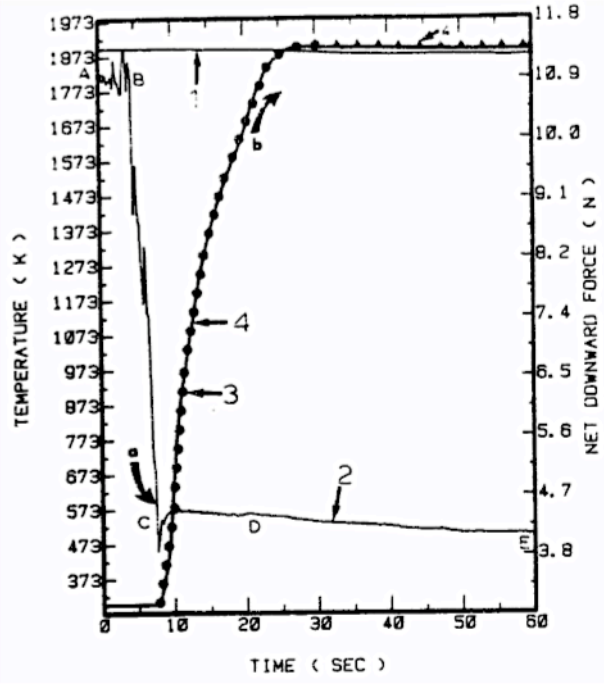

Figure 25 – Results of dissolving a niobium cylinder in liquid steel[30]

Several pieces of information can be gathered from Figure 25. It was observed that the radius decreased in a linear manner during the dissolution period. This linearity is attributed to the mass transfer kinetics of dissolution of a large object; the mass transfer coefficient is not a strong function of diameter when the dissolving object is large. Generally speaking, if the object is small enough, the effect of size is an important one on the dissolution kinetics and such a linear trend would not be observed. Another experimental observation shown in Figure 25 is that the temperature distribution in the cylinder exceeded the bath temperature by a constant value (~10°C), which may be related to the exothermic reaction of Nb with liquid Fe[††]. In the publication, it was stated that the heat generated by the exothermicity of ferroniobium was *small*. In other words, it

[††] The partial molar heat of mixing of Nb at infinite dilution in liquid iron is $\Delta\bar{H}^{0}_{Nb} = -37.7$ kJ/mol atoms

does not have a large effect on the kinetics of dissolution of ferroniobium, contrary to previous publications. This discrepancy with the previous publications can be remedied by considering that dissolution kinetics is governed by mass transfer phenomena (*i.e.* not heat transfer kinetics). If the temperature is increased slightly at the surface of the dissolving object, the resulting effect on the diffusion coefficient, concentration profile, and fluid conditions is hardly noticeable.

The modeling efforts are combined with the experimental results in Figure 26. It was observed that the time of the steel shell period was predicted to exist for 10–15 seconds on a 2.54 cm diameter Nb cylinder. Experimental results for the "free" dissolution period of Nb cylinders in liquid steel were only presented for times not exceeding 60 seconds, as the dissolution kinetics of niobium is more sluggish compared to zirconium and titanium cylinders.

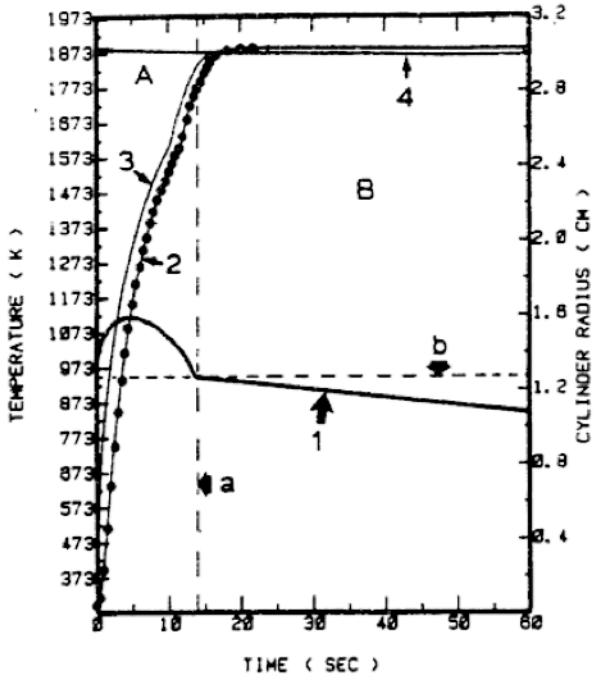

Figure 26 – Experimental and predicted results of a niobium dissolution experiment in liquid steel[30]

The last publication dealing with the effect of microstructure on the rate of dissolution was by Argyropoulos *et al*[28]. In this work, the formation of intermetallics at the interface of the niobium cylinder and the solidified steel shell around the cylinder was observed. In order to capture this event, a composite cylinder was fabricated; this composite cylinder was composed of an inner cylinder of solidified steel surrounded by an outer cylinder of niobium (Figure 27). The formation of intermetallics was observed by inserting a thermocouple, whose tip was at the steel/niobium interface of the composite cylinder.

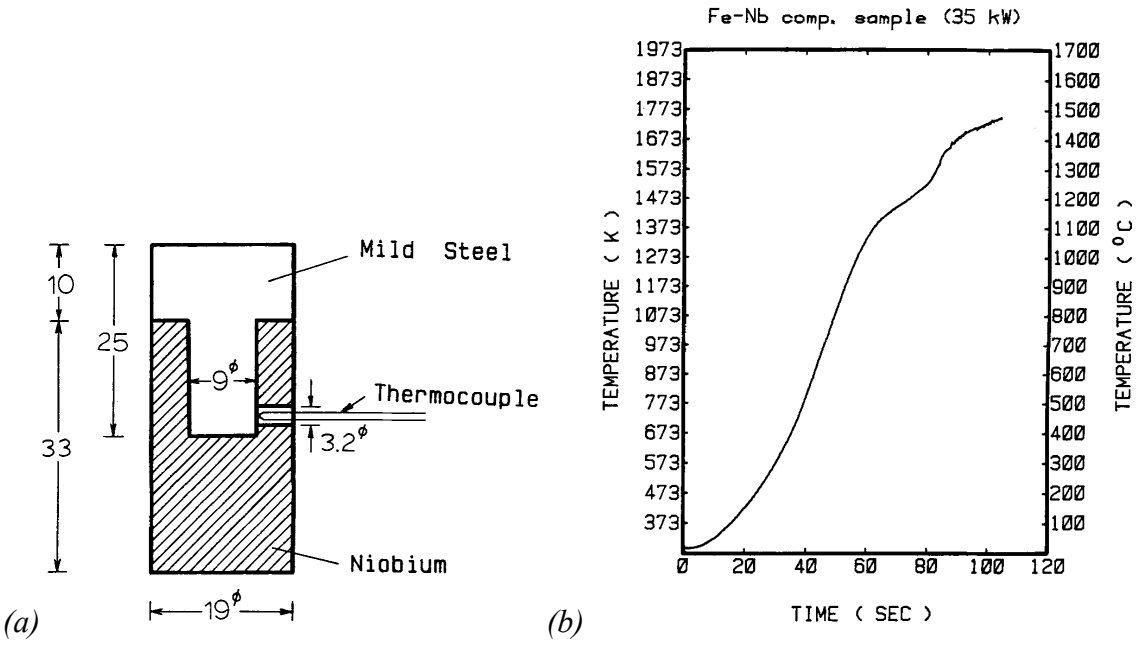

Figure 27 – *(a)* Schematic cross-section of a composite cylinder (all dimensions are in millimeters); *(b)* a typical outcome of the temperature-time dependence during induction heating experiments[28]

When the composite cylinder was inductively heated, a reaction was detected by the thermocouple near 1370°C at the steel/Nb interface. This reaction occurs near the 80th second in Figure 27 and is detected by abrupt changes in the temperature-time data. After

this erratic behaviour, the thermocouple failed and the authors attributed this failure to chemical attack of the thermocouple by the eutectic liquid that formed at the reaction temperature. Once the liquid eutectic formed, the high mass transfer rates aided in formation of intermetallic compounds. The intermetallic compounds Fe_2Nb and Fe_2Nb_3 were identified as reaction products by electron probe X-ray microanalysis (EPMA).

These results were related to the addition of ferroniobium in liquid steel by adding ferroniobium to a steel bath. Since the heat transfer kinetics are an important consideration for the time of the steel shell period, a low superheat bath and a high superheat bath were prepared. When the bath superheat is low, the interfacial reaction was observed, since the time that the steel shell existed on ferroniobium was longer than the time needed for the formation of intermetallics to occur. In the case that the bath superheat is high, this reaction did not take place, since the steel shell melts back before the niobium cylinder reached the reaction temperature to form intermetallic compounds. However, if intermetallic compounds formed during the steel shell period, they were expected to form at near the end of the existence of the steel shell.

This is shown in Figure 28 where the steel shell period is predicted from a model for various diameters of niobium cylinders. In this figure, curve 2 represents baths with low superheats, while curve 3 represents baths with high superheats. However, both curves 2 and 3 were predicted to have similar times for the existence of the steel shell. The interfacial reaction to form intermetallic compounds did not affect the time of the shell period. Such a conclusion was attributed to the fact that the interfacial reaction

occurred at late stages of the steel shell existence, and the small amount of heat released did not result in a shorter time.

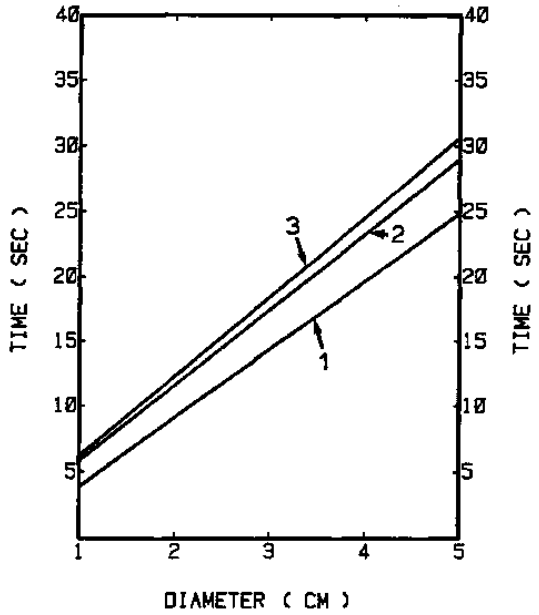

Figure 28 – Predicted steel shell periods for niobium cylinders of various diameters; curve 1: when reaction begins during steel shell period; curve 2: shell period for large value of generated heat flux; curve 3: shell period without any heat generation[28]

Another aspect of this work was the kinetics of dissolution of pure Nb cylinders. This was examined to compare with the bcc Nb particles observed in the ferroniobium microstructure. However, the particles are of the micron size, too small to be used in experiments. Therefore, Nb cylinders with diameters ranging from 2 to 6 cm were immersed in liquid steel and their weight change was measured under natural and forced convection conditions. A load cell was used to measure the change in weight by suspending the cylinders in the melt; additionally, the temperature of the liquid was measured continuously during immersion and all the data was recorded by a data acquisition system.

One of the primary goals of [28] was to identify an actual mechanism of Nb mass transfer in liquid steel, taking into account the macroexothermicity of Nb in liquid Fe. To do this, niobium cylinders were dissolved in liquid steel, and the mass transfer coefficients at various temperatures and fluid conditions were experimentally determined. These mass transfer coefficients were extrapolated from the experimental data by way of linear regression analysis. These mass transfer coefficients were then used in a temperature-dependant dissolution equation to predict the kinetics of dissolution of niobium cylinders in liquid steel. The rate-controlling step was identified as liquid phase diffusion through a boundary layer at the niobium/steel interface. For this reason, the effect of macroexothermicity was stated to be minor on the dissolution rate of niobium as shown by Sismanis *et al.*[30]. The results of these efforts produced Figure 29, which gives the total dissolution time (including the shell period) for a niobium cylinder in liquid steel.

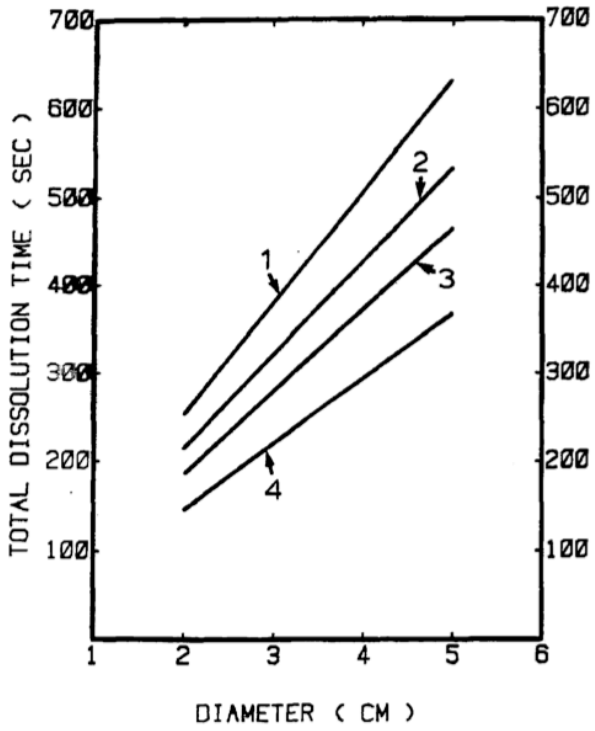

Figure 29 – Predicted total dissolution times for different steel bath temperatures and stirring conditions; curve 1: liquid steel at 1590°C, natural convection; curve 2: liquid steel at 1615°C, natural convection; curve 3: liquid steel at 1640°C, natural convection; curve 4: liquid steel at 1610°C, forced convection [28]

In conclusion, the publications reviewed the most important papers dedicated to ferroniobium dissolution kinetics. Yet, a significant aspect is missing in these publications. Although the second group considered the binary Fe–Nb system and the phases contained therein, such as Fe_2Nb, Fe_7Nb_6, Fe_2Nb_3, and Nb solid solution, the microstructure of standard grade and high-purity grade ferroniobium was not inspected to determine if the microstructure corresponded to the binary phase diagram. In particular, an impurity element may promote the formation of another phase. For example, carbon is known to readily form niobium carbides. What if the concentration of carbon is sufficient to stimulate the formation of carbides during solidification of ferroniobium? The

multiphase aspect of a ferroniobium alloy takes on a whole new meaning with the presence of thermodynamically stable phases such as carbides. Thus, the dissolution kinetics of niobium carbide must also be determined.

4 Thermodynamic Databases

Computational thermodynamics employs databases containing thermodynamic properties of phases in systems of interest (steels, Al alloys, aqueous solutions, *etc.*). Today, almost all databases are constructed using the so called CALPHAD method[31,32]. A practical implementation of this technique requires a critical analysis of all available experimental data on thermodynamic properties of phases and heterogeneous mixtures as well as on conditions of phase equilibria. As a part of the analysis, uncertainties are assigned to experimental conditions (*e.g.*, mole fractions and temperatures) and measured quantities (activities, enthalpies of mixing, etc.). Then information is passed to a program finding such adjustable coefficients in the analytical descriptions of the Gibbs energies of phases that the best match between the experimental quantities and their computed counterparts[‡‡] is achieved. A modern database is a result of thermodynamic optimizations (assessments) written in a prescribed format.

Regretfully, databases dedicated to ferroalloys, in general, and ferroniobium, in particular, do not exist. Under such a circumstance, the usage of one of several commercially available steel databases seems not too unreasonable. It should be kept in mind, however, that while using a particular database, one should remain within compositional limits specified by developers of the database. In the case of steel databases, there are bounds imposed on the concentrations of iron and alloying additions. For the two Thermo-Calc compatible databases tried in this work, the maximum values are shown in Table 4, from which it is apparent that, strictly speaking, neither are suitable

[‡‡] PARROT module of Thermo–Calc is the most frequently utilized program of this kind.

to model solidification of ferroniobium in which the concentration of Nb is much higher than 5 wt.%. This does not mean that the calculations should not be launched; this means that simulation results must be interpreted and used with a healthy scepticism.

Table 4 – Limitations on the wt. % of components in the thermodynamic databases

Component	Database	
	TCFE2	TCFE6
Fe	≥50	
C	≤2	≤7
Nb	≤1	≤5

Since it would be unreasonable to carry out identical calculations using the two databases and present computational outcomes side-by-side, it was decided to utilize TCFE2 and TCFE6 for constructing the Fe–Nb phase diagram and compare them with those known from experiments.

4.1 Comparing Databases in the Fe–Nb Binary System

The Fe–Nb phase diagrams calculated from these two databases are shown in Figure 30. The iron-rich sides are virtually identical, but above 40 at. % Nb, the diagrams diverge. A comparison of the calculated phase diagrams with the most reliable experimental counterpart shown in Figure 30*(b)* suggests that preference should be given to TCFE2. This older database also yields a much more reasonable 1600°C isotherm. Consequently, it was decided to use TCFE2 for thermodynamic modeling. It is worth reiterating that since this database is intended for steels, it is not merely desirable, but necessary to confront the results of numerical simulations with experimental observations.

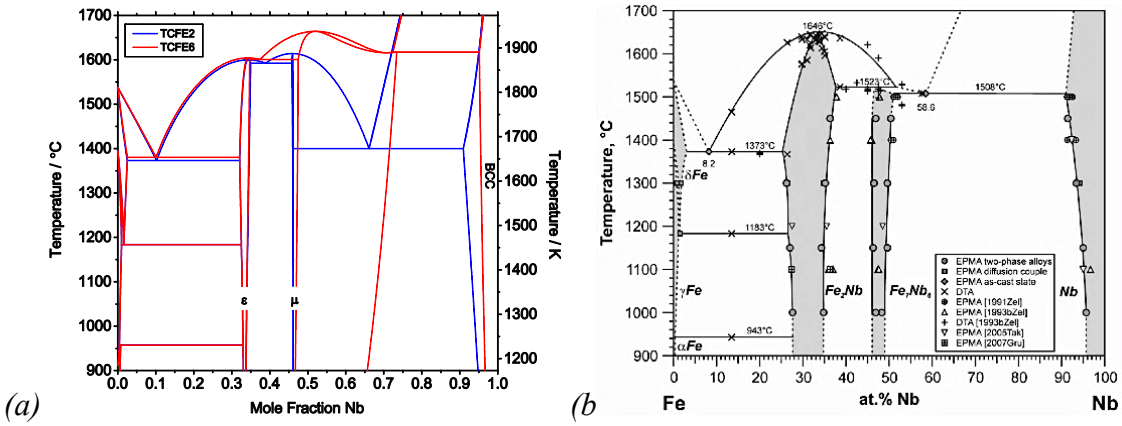

Figure 30 – The Fe–Nb phase diagram from *(a)* thermodynamic databases and *(b)* Voss *et al.*[19]

Now, inspect the phase diagram of the Fe–Nb system shown in Figure 31 and consider the solidification of the melt containing 76.5 wt. % Nb (in the following sections, all % are wt. % unless otherwise indicated). Since this composition is nearly identical to the calculated eutectic composition, the resulting ferroniobium is a eutectic mixture of the μ-phase[§§] and Nb-rich bcc phase (Table 5).

Table 5 – Relevant information concerning phases discussed in this contribution

Phase	Crystal Structure	Structure Form	at. % Nb
μ	Hexagonal (rhombohedral)	Fe_7Nb_6	46–51
ε (C14 Laves)	Hexagonal	Fe_2Nb	25–38
η	…	Fe_2Nb_3	60–62
Niobium Carbide	Hexagonal	Nb_2C	66–75
Nb-rich	bcc	Nb	91–100

[§§] Its sublattice model adopted in the TCFE2 database is $(Fe, Nb)_7(Nb)_2(Fe, Nb)_4$.

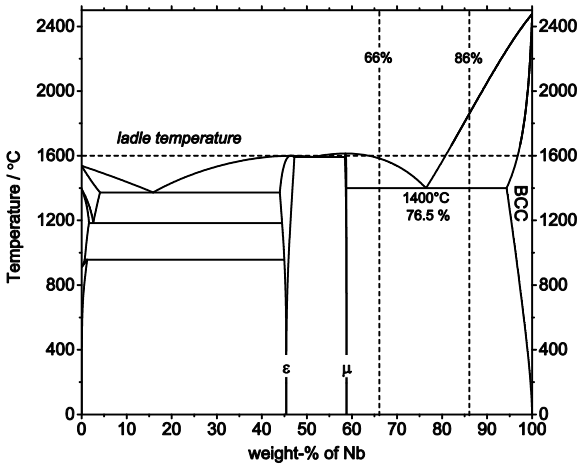

Figure 31 – The phase diagram of the Fe–Nb system and supplementary information

Consider the situation when a piece of ferroniobium having the eutectic composition is added to steel having a temperature around 1600°C, *i.e.*, approximately 200°C higher than the eutectic temperature. Almost instantly, steel freezes at the surface of the addition resulting in the formation of a crust (shell), enveloping the ferroalloy[24,25,29,30,33]. The crust re-melts, the piece is being heated up and then it fuses yielding a Nb-rich liquid which promptly mixes with the surrounding molten steel. From the physical viewpoint, what happens with ferroniobium in this case is not dissimilar from melting of iron[34], manganese, nickel[35,36], and tin or scrap[37,38] immersed in hot steel. Ferroniobium with 76.5 wt.% Nb perfectly serves the purpose it is intended for without any adverse side effects. In other words, at 1600°C its disintegration is accompanied by a release of phases that cannot survive heating in a ladle without melting.

4.2 Computing the Solidification Path of a Fe–66%Nb Alloy

The solidification path of a melt containing 66 % Nb is shown in Figure 32. In the beginning of freezing, the μ phase forms and then it accumulates in the system. As a result, the remaining liquid is being enriched with niobium. When the concentration of Nb becomes equal to the eutectic concentration, a eutectic solidification occurs. The phase portrait of ferroniobium with 66 % Nb is primary μ phase particles (approximately 60 %) and the μ+bcc eutectic.

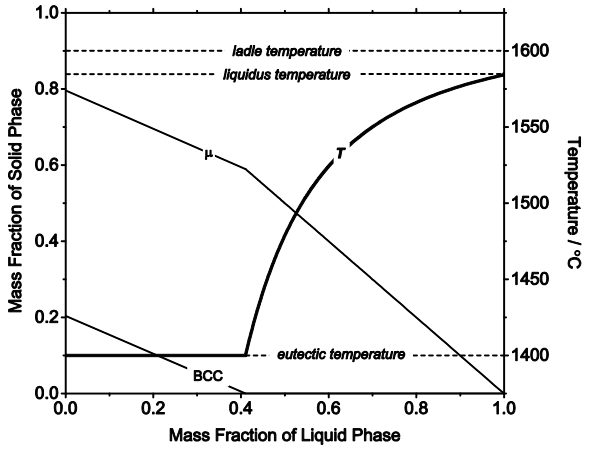

Figure 32 – Accumulation of phases during solidification of Fe–66%Nb melt

In order to understand what happens when a piece of such ferroniobium is added to steel, assume that its heating to a certain temperature T^* does not affect those parts of ferroalloy that crystallised at temperature above T^*. The parts of ferroalloy that formed during solidification below T^* fuse yielding volumes of liquid with a uniform composition. In other words, the state achieved by increasing temperature up to T^* is indistinguishable from the state attained by interrupting solidification at this same temperature[39]. Heating of ferroniobium with 66 % Nb dropped in liquid steel results in

the eutectic melting at 1400°C and a release of the primary μ particles in the surrounding liquid steel. These particles cannot withstand heating to ladle temperature; they will melt and mix quickly with steel. It can thus be concluded that the usage of Fe–66%Nb ferroalloy should not cause difficulties.

4.3 Computing the Solidification Path of a Fe–86%Nb Alloy

The situation would be dramatically different if ferroniobium with 86 % Nb is utilised. As Figure 33 suggests, heating of ferroalloy to 1600°C inside a ladle triggers the eutectic melting. As a result, primary bcc particles are released in steel. A prominent feature of these particles is that they are not compositionally uniform. The Nb concentration decreases from the center where solidification begins to the surface at which it becomes equal to the eutectic concentration. Consequently, at 1600°C, only an outer portion of the particles fuses and mixes with steel when the ladle temperature is achieved.

Dissolution of the remaining Nb-rich particles in the surrounding liquid is a slower process, which means that the primary bcc pieces may remain undissolved, which, in turn, may cause two detrimental effects. First, the Nb concentration in a steel matrix will be less than expected. Second, and more importantly, if these particles are coarse, then their presence in the final product may adversely affect its mechanical properties. Whether the coarse particles arguably existing in ferroniobium are actually seen in steels microalloyed with Nb depends on their dissolution rate, which, in turn, depends on steel's composition. The importance of determining the kinetics of dissolution was clearly understood by Argyropoulos who experimentally determined the dissolution rate of

niobium in liquid steel[28]. From that work, it can be estimated what time would be sufficient for a complete dissolution of a Nb-rich particle with a given size in fluid conditions of forced or natural convection. For instance, the time for complete dissolution of a particle 20 mm in diameter in a steel bath temperature of 1600°C is approximately 3.8 minutes for natural convection conditions.

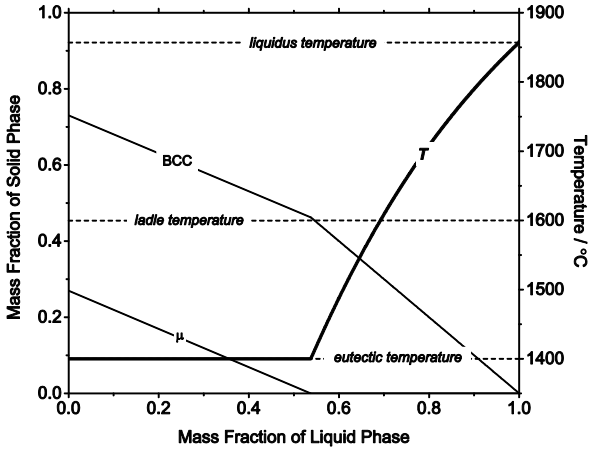

Figure 33 – Accumulation of phases during solidification of a Fe-86%Nb melt

4.4 The Effect of Carbon

It was understood a while ago[27-30] that ferroalloys were multiphase entities, and that an easily detectable dispersion of a piece of ferroalloy as a macroscopic object did not necessarily mean that it had been completely dissolved in the true meaning of this word. It was realised[11,12] that its partial fusing[***] could release solid phases with melting points higher than the ladle temperature, and that it could not be taken for granted that the dissolution of corresponding particles in steel happened quickly. Consequently, it is tempting to infer that this research field is so well-developed[24-30,33,40] that it does not

[***] In a majority of cases, the onset of partial fusing corresponds to eutectic melting.

require further experimental and theoretical efforts. Such a conclusion, however, would be premature. In order to understand why, recall that according to Figure 32, the usage of Fe–66%Nb ferroalloy should be worry-free. What will happen if this alloy contains carbon? A computational answer to this question is given in Figure 34. If carbon percentage in ferroniobium is as low as 0.1 %, it does not have a harmful effect in the sense that its liquidus temperature does not exceed the ladle temperature. If carbon content increases, this favourable state of affairs does not hold.

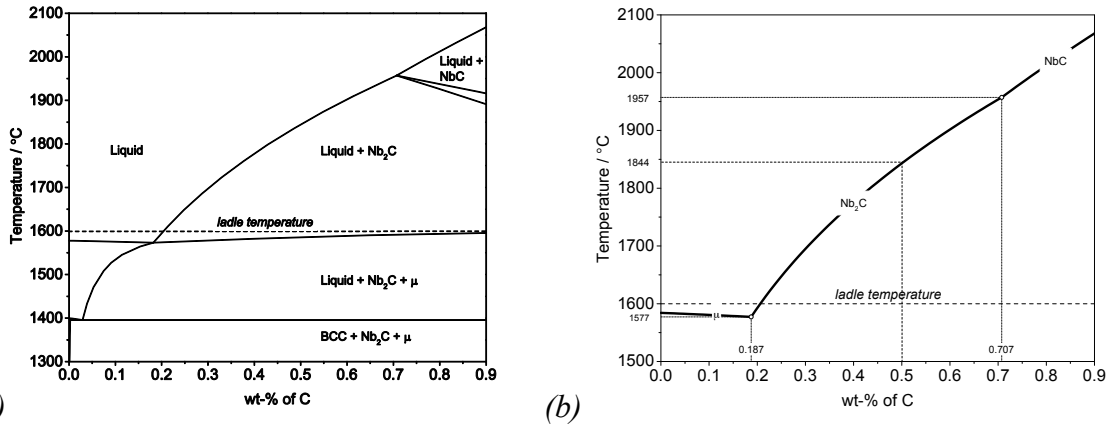

Figure 34 – *(a)* Isopleth of the Fe–66%Nb–C system; *(b)* Liquidus curve extracted from *a* with supplementary information

4.4.1 Computing the Solidification Path of a Fe–66%Nb–0.5%C Alloy

Consider the sequence of events during the manufacturing of Fe–66%Nb–0.5%C ferroalloy. Ferroniobium is cast from temperature exceeding 2000°C, which is deemed sufficient for a complete melting. When temperature decreases below liquidus (*i.e.*, below 1844°C), the Nb_2C phase with the hcp structure begins to form. At the moment when temperature reaches 1600°C (ladle temperature), the system contains approximately 8% of Nb_2C (Figure 35). Although it is hardly possible to predict a size distribution of Nb_2C

particles, which depends on technological particularities, coarse carbide precipitates may form if the cooling rate is sufficiently low. If a piece of such ferroniobium is dropped in steel, then most of it (slightly more than 90 %) will melt by the time 1600°C is achieved, which means a full disintegration of the piece, if it is considered as a macroscopic physical object. If a piece of ferroniobium is attached to a load cell, and its mass change is monitored as was the case in previous works[25-27,29,40], then the instance of a complete disappearance can easily be detected. The piece as such has vanished indeed, but it would take additional time for any carbide particles that formed above 1600°C during the solidification of ferroalloy to dissolve in liquid steel.

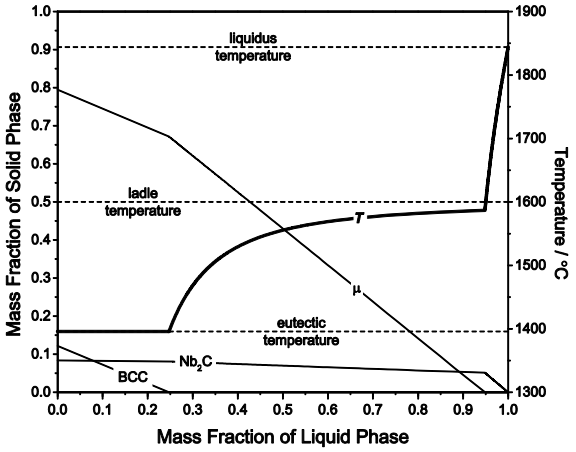

Figure 35 – Accumulation of phases during solidification of a Fe-66%Nb-0.5%C melt

These computational results suggest that $M_2(C,N)$ carbonitrides may exist in ferroalloys, in general, and in ferroniobium, in particular. A validity of the computational results is questionable, because, as mentioned above, the concentration limits within which TCFE2 should be employed were not respected. Apparently, the hypothesis that the carbon concentration has a pronounced effect on the phase portrait of ferroniobium and its liquidus temperature must be corroborated experimentally. In the next two

sections our efforts to find experimental evidences supporting the supposition are presented.

5 Experimental Method

Four ferroniobium alloys with carbon composition shown in Table 6 were prepared from samples of as-received ferroniobium (Table 7). All four samples were placed in a rotating water-cooled copper hearth inside an arc-melting furnace in a protective argon atmosphere. The alloys were above liquidus temperature for at least one minute and then solidified quickly, producing a fine microstructure. Subsequently, they were flipped over, and the melting/solidification process was repeated 4–5 times to ensure a compositional homogeneity of the liquid ferroalloy. Alloy 1 is an as-received commercial ferroalloy. Alloys 2–4 were produced by adding required amounts of carbon (tiny graphite rods were used) to Alloy 1, which implies that the Nb concentration in all the alloys was approximately equal to 66 %. The concentration of carbon is reported as an average concentration in Table 6 for each ferroniobium alloy, and was measured using a LECO CS–444 carbon/sulphur analyzer.

Table 6 – Concentration of carbon (wt. %) for each ferroniobium alloy

	Alloy 1	Alloy 2	Alloy 3	Alloy 4
Target Concentration	…	0.3	0.5	0.7
Actual Concentration	0.113	0.309	0.548	0.693

Table 7 – Chemical composition (wt. %) of as-received ferroniobium (analysis per ferroniobium manufacturer)

Al	C	Fe	Mn	Nb	P	Pb	S	Si	Sn	Ti
1.1	0.1	Bal.	0.35	65.8	0.1	0.089	<0.1	1.3	0.038	0.49

Solidification of each alloy was followed by a metallographic investigation to reveal microstructural changes caused by the variations of carbon concentration. Such an examination is associated with a particular complication[†††] hinted by Figure 34, which suggests that an increase in carbon concentration may result in the formation of primary Nb_2C particles above 1600°C. An increase of driving force for the formation of primary Nb_2C during cooling may cause growth of these carbide particles at high temperature. Microstructural features, in general, and the distribution of particle sizes, in particular, are expected to be influenced by the rate of heat extraction during solidification[41], such that, if the cooling rate is high, the Nb_2C particles are very fine.

The metallographic preparation (see section 10.1 on page 106) of ferroniobium involved sectioning, polishing, and etching[42] each alloy in a similar manner. Although compositional dissimilarities make an identification of each phase possible *via* the EDX analysis, this technique is semi-quantitative. A crystallographic identification of each phase by electron backscattered diffraction (EBSD) is used to guarantee that the EDX results are not misinterpreted. The crystallographic information on all possible phases was retrieved from the Inorganic Crystal Structure Database (ICSD)[43].

[†††] The unexpected appearance of many, large carbides that form as a primary phase in the microstructure of ferroniobium may lead to a complication for steelmakers if these carbides dissolve slowly in liquid steel.

6 Experimental Results and Discussion

Several randomly chosen pieces of commercial grade ferroniobium with the composition given in Table 7 were examined using optical microscopy. They all demonstrated very similar microstructural features exemplified by Figure 36. Commercial ferroniobium contains chunky and elongated Nb_2C particles whose size may reach tens of microns. Although the concentration of carbon is low, the presence of carbides is unsurprising in view of their remarkable thermodynamic stability.

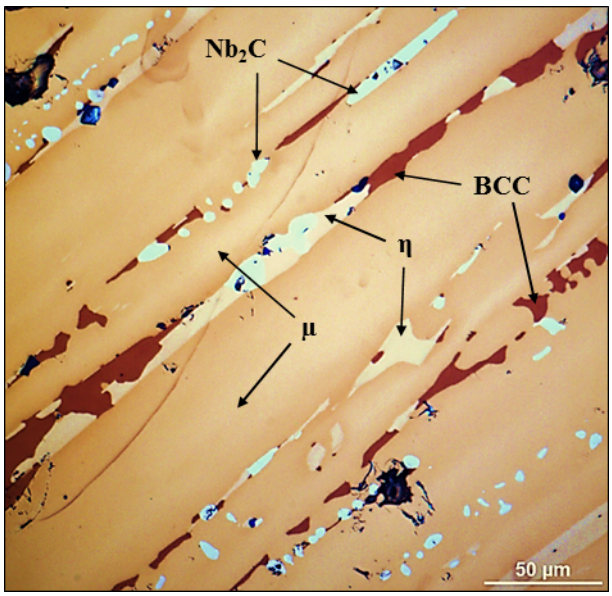

Figure 36 – Microstructure of ferroniobium (as-received)

Let us compare the predictions based on both information TCFE2 contains and the assumption that Scheil's formalism works, with the factual microstructures of solidified Alloys 1–4. The computational results for Alloys 1–4 are illustrated in Figure 37 and relevant aspects to this contribution have been extracted into Table 8. An examination of

Table 8 reveals that the Nb_2C phase becomes a primary phase[‡‡‡] when the carbon concentration is increased from 0.113 to 0.309 % C.

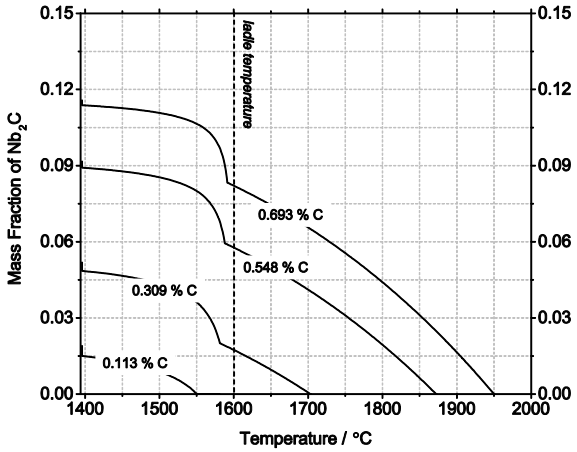

Figure 37 – The influence of carbon concentration on the accumulation of the Nb_2C phase during solidification of ferroniobium alloys from Table 6

Table 8 – Effect of carbon concentration on different parameters calculated from TCFE2 and Scheil for ferroniobium alloys

	% Carbon	$T^{liquidus}$ (°C)	Primary Phase	Mass Percent of Nb_2C Phase	Phase Portrait
Alloy 1	0.113	1575	μ	1.9	μ , bcc, Nb_2C
Alloy 2	0.309	1705	Nb_2C	5.2	μ , bcc, Nb_2C
Alloy 3	0.548	1873	Nb_2C	9.2	μ , bcc, Nb_2C
Alloy 4	0.693	1950	Nb_2C	11.6	μ , bcc, Nb_2C

The microstructure of each of these ferroniobium alloys with carbon concentrations given in Table 6 was examined to determine the primary phase that formed during solidification, and its weight fraction. Optical micrographs containing etched microstructures of these four alloys were examined (Figure 38) and software for the optical microscope was utilised to determine the weight fraction of the Nb_2C phase. Although the software gives surface fractions for each phase, they are converted to weight

[‡‡‡] "primary phase" refers to the phase that formed first during solidification of an alloy

fractions using phase densities retrieved from ICSD. An example of the surface fraction of phases for the ferroniobium alloy with 0.113 % C is compared with thermodynamic calculations in Table 9. It is clear from the microstructures in Figure 38 that when carbon content increases from 0.113 % to 0.309 %, there is a distinct change of primary phase. At low carbon concentrations, the Nb_2C phase forms primarily in the interdendritic regions in Figure 38(a); however, with an increase in carbon concentration, the Nb_2C phase in Figure 38(b) is clearly shown to be the primary phase, because the morphology has changed to chunky, elongated particles that do not align in a preferred orientation. As the carbon concentration increases in Figure 38(c) and Figure 38(d), the fraction of primary Nb_2C phase increases and consequently decreases in the interdendritic regions. These results agree with the thermodynamic predictions of Table 8.

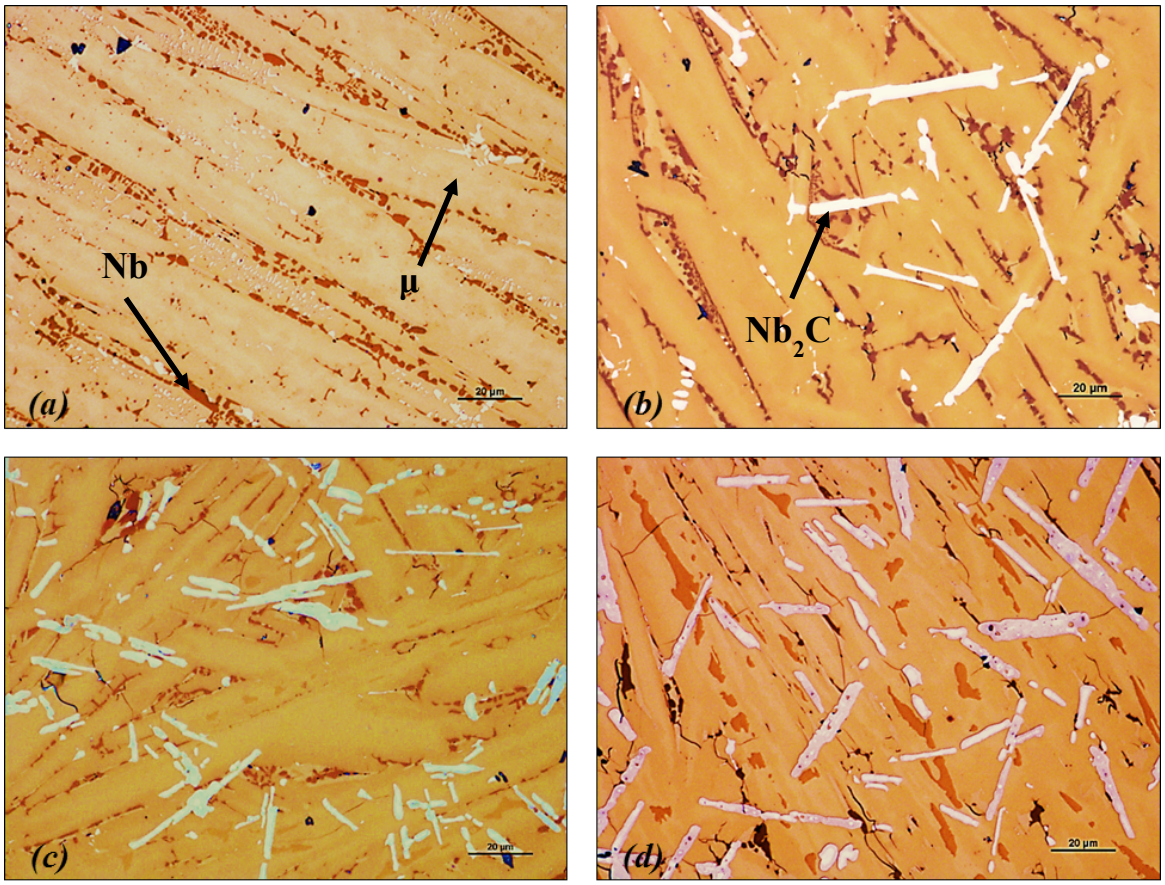

Figure 38 – The representative microstructures of ferroniobium alloys with varying carbon content; images *(a)-(d)* correspond to Alloys 1–4, respectively

Table 9 – Comparison of weight fractions of phases in Alloy 1

Phase	Weight Fractions (%)	
	From image analysis	Prediction based on TCFE2 and Scheil
Nb_2C	2.5	1.9
bcc	14.7	21.29
μ	82.8	76.81
Total	100	100

The backscattered electron (BSE) images of Alloy 4 are shown in Figure 39. Since this alloy contained phases with the largest sizes, it was chosen to perform EDX analysis; the EDX results of these images is presented in Table 10. From this table, two Nb-rich phases were detected by EDX analysis. The phase corresponding to location 4 was determined to be the Nb-rich bcc phase, based mostly on the fact that there was significant solubility of Fe in the Nb-rich phase, as compared to locations 1 and 5 which contained trace amounts of Fe in the Nb-rich phase. This was supported with the investigation of the crystal structure using EBSD (Figure 40). The Nb-rich bcc phase was confirmed to have the bcc crystal structure; the other Nb-rich phase corresponding to locations 1 and 5 was predicted to be a carbide phase (*i.e.* NbC and/or Nb_2C). From the EBSD results, this carbide phase was confirmed to be the Nb_2C phase with the hcp crystal structure.

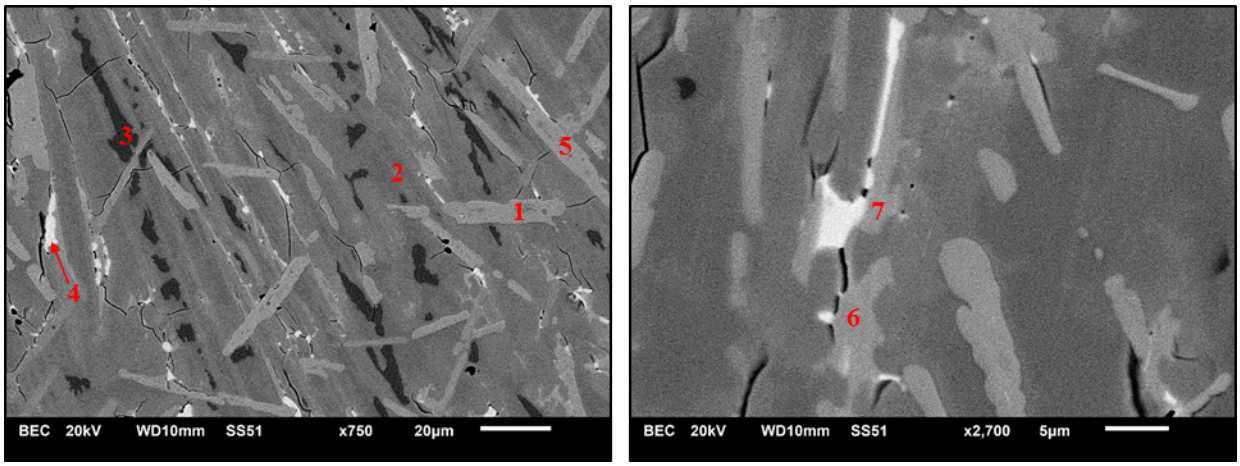

Figure 39 – BSE images of Alloy 4

Table 10 – EDX analysis of phases in Alloy 4 at locations shown in Figure 39

Location	Elements (at. %)						Phase (based on EBSD)
	Fe	Nb	Ti	Al	Si	Mn	
1	0.89	98.47	0.64	0.00	0.00	0.00	Nb_2C
2	43.00	51.71	0.41	0.88	3.59	0.41	μ
3	52.18	39.63	0.30	0.99	6.43	0.47	ε
4	7.29	92.20	0.51	0.00	0.00	0.00	bcc
5	0.89	98.47	0.64	0.00	0.00	0.00	Nb_2C
6	34.48	62.46	0.77	0.56	1.73	0.00	η
7	35.19	61.02	0.67	0.59	2.52	0.00	η

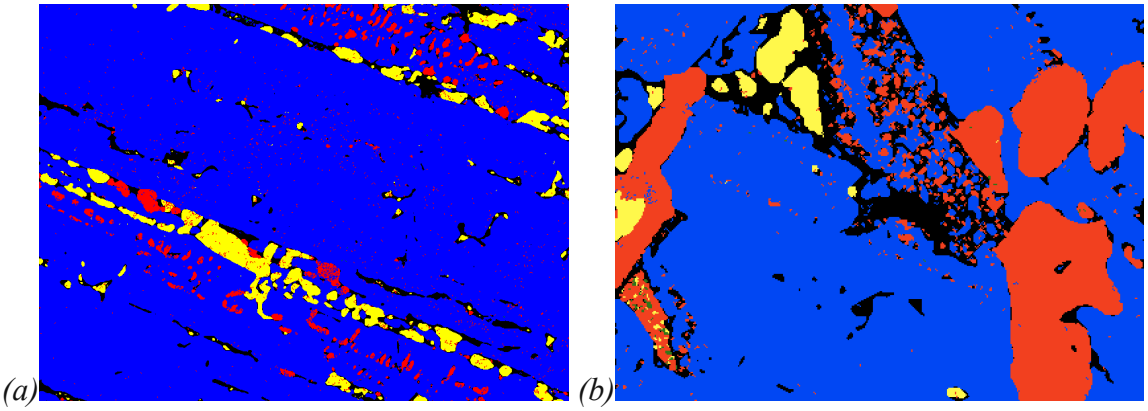

(a) *(b)*

Figure 40 – EBSD maps for *(a)* Alloy 1 and *(b)* Alloy 4; yellow is the bcc phase, red is the hcp phase, and blue is the μ-phase; the black areas are unidentified regions

Additionally, EBSD was used to identify the μ-phase and the interdendritic ε phase. However, the crystal structure of the metastable η-phase was not identified in the EBSD analysis because its crystallography has not been reported in the literature. As a result, identification of the η-phase is based solely on EDX analysis and optical micrographs. These results coincide with Bejarano *et al.*[16,17] and Raman *et al.*[23], who noted that the η-phase may be stabilised by the presence of impurities such as Al, Ti, and Si.

In summary, a combination of SEM-EDX and SEM-EBSD was used to validate the thermodynamic modeling of the Fe–Nb–C system. The increase of carbon content has a two-fold effect which is indisputable: first, the mass fraction of Nb_2C increases with increasing carbon content; second, Nb_2C becomes the primary phase as carbon content increases.

7 Dissolution Thermodynamics and Kinetics

The dissolution kinetics of numerous ferroalloys was investigated several decades ago. Since this area of high temperature metallurgy has been heavily researched, it is tempting to conclude that it does not deserve further attention. However, it has been shown in this contribution that ferroniobium contains several thermodynamically stable phases: the bcc niobium rich phase, and the hcp niobium carbide phase whose dissolution kinetics have *not* been considered in previous works. It is noteworthy to mention that the micron size of these phases permits them to escape the detection of macroscopic measuring devices (*i.e.* load cells attached to a bulk piece of ferroniobium).

If these thermodynamically stable phases dissolve slowly, they may be incorporated into the cast slab as proposed by Abraham et al[11,12]. Although fine particles are desired (*e.g.* tens of nanometers), the large size of these stable particles in the slab has a deleterious effect on mechanical properties such as yield strength and toughness. It has been shown in the literature review that Nb-rich particles have been observed in HSLA cast slabs. Therefore, this contribution will also focus on modeling the kinetics and thermodynamics of dissolution of Nb, Nb_2C, and NbC.

In order to validate the model, experimental results must be used as a comparison. A good model would ideally capture the specific assumptions and conditions used in the experiments. There are two challenges that present themselves here: first, the physics of the model must be established for the simple case (*i.e.* two-component system); second, the lack of publications with experimental work on dissolution of thermodynamically stable phases (*i.e.* multi-component systems) present a challenge to validate the model for

a multicomponent system. To that end, the model will be validated using the two-component system of iron and niobium, which considers the dissolution of niobium spheres in liquid iron. The physics of this model is validated with experimental work performed by Argyropoulos *et al.*[28]. Subsequently, dissolution of Nb_2C and NbC in liquid iron will be modeled. This ternary model can be compared with commercial software like DICTRA, which considers diffusionally controlled transformations in solid-solid and solid-liquid systems. This software uses thermodynamic and mobility databases to determine rates of diffusional transformations.

7.1 A Theoretical Treatment

While the expression for mass fluxes can be written in such a way to conceptualize the kinetics of dissolution, the thermodynamics of dissolution is more complicated. The thermodynamics of dissolution is a term that expresses the equilibrium that a dissolving body achieves with a liquid solvent. If a solid dissolves in a liquid, then there exists an equilibrium concentration at the interface of the solid and liquid that permits the solid to dissolve in the liquid. Although this interface can be considered to have a thickness, in the case of dissolution only the side of the interface adjacent to the liquid is relevant, because the diffusion of a component in liquid is much faster than the diffusion of a component through a solid phase. The thermodynamics of dissolution determines the equilibrium composition at the interface of a solid body dissolving in a liquid.

7.1.1 Mass Flux Balance for a Pure Substance

In the treatment of mass transport phenomena, it is instructive to return to the basic problem of mass fluxes[§§§] and the mechanisms of mass transport, in order to clearly define the problem. The starting point for modeling the dissolution phenomenon of solid sphere of niobium immersed in an isothermal melt of pure liquid iron is to determine the mass flux. The choice of spherical geometry permits the formulation of mass fluxes to be considered in one dimension-a simplification indeed-but a useful one. In the following treatment, the starting point for dissolution is to equate the change in mass of a solid object with the flux of the mass of the solid object into the liquid per surface area per unit time. Since one-dimensional flow will be considered as a simplification where the operative dimension is in the radial direction, this equation can be transcribed from words to an expression in the following form:

$$\frac{dm_{\mathrm{Nb}}}{dt} = -N_{\mathrm{Nb}} A_{\mathrm{int,Nb}} \qquad -(1)$$

where N_{Nb} is the total mass flux of niobium, for which the diffusive flux and bulk flux (i.e. from convection) is combined.

This total mass flux is the foundation upon which the phenomena of dissolution are derived. From it, the concentration profile can be established, and the mass balance can be determined. Thus, the flux equations are relied upon to relate fluid conditions and properties and the dissolution thermodynamics and kinetics of a solute in a solvent. The expression for total mass flux is extracted from Bird *et al.*[44] in the following manner:

[§§§] Mass fluxes will be used instead of molar fluxes, although the formulation is the same

$$\underbrace{N_{\mathrm{Nb}}}_{\text{total flux}} = \underbrace{J_{\mathrm{Nb}}}_{\text{diffusive flux}} + \underbrace{\omega_{\mathrm{Nb}}\left(N_{\mathrm{Nb}} + N_{\mathrm{Fe}}\right)}_{\text{bulk flux}} \qquad -(2)$$

The precise relationship between the total flux, N_{Nb}, and the bulk flux is not easily determined since the flux of niobium *and* the flux of iron must be known to solve equation (2). Researchers have overcome this obstacle by characterizing the fluid conditions with dimensionless numbers[45].

Such efforts have resulted in reasonable approximations for velocity or density gradients. Of course, for a stagnant fluid, velocity and density gradients are zero and consequently, the bulky theoretical derivations are reduced to a simple diffusion equation. For example, the mass flux expression for a stagnant fluid is:

$$N_{Nb} = -\frac{\rho_L D_{Nb}}{\left(\omega_{Fe}\right)_{\ln}}\frac{\partial \omega}{\partial r} = \frac{\rho_L D_{Nb}}{\left(\omega_{Fe}\right)_{\ln} R_{Nb}(t)}\left(\omega_{Nb}^{*} - \omega_{Nb}^{\infty}\right) \qquad -(3)$$

It should be noted that since mass fractions are used in the concentration gradient of equation (3), the Fickian flux is adjusted by incorporating the density of the liquid into the mass flux expression; this can be clarified by performing a unit analysis. In addition, the term $\left(\omega_{Fe}\right)_{\ln}$ is a correction factor used for non-dilute systems, where the flux of solute atoms from the interface introduces a counter-flux of solvent atoms to the interface (see section 10.2 on page 106 for details).

7.1.2 The Mass Transfer Coefficient

In order to treat velocity and density gradients, one must turn to equation (2) and consider the sum of bulk and diffusive fluxes. The manner in which the velocity term is included in the mass flux balance is rather elusive. One will notice that the bulk flux in

equation (2) is a product of concentration and velocity for forced convection (or, density for natural convection). To handle this awkward product, dimensionless numbers (Table 11) are employed to capture the physics of non-zero velocity and density gradients.

Table 11 – Definitions of dimensionless numbers

Dimensionless Number	Symbol	Meaning
Grashof	Gr	Ratio of natural convection buoyancy force to viscous force
Reynolds	Re	Ratio of inertial to viscous forces
Schmidt	Sc	Ratio of the momentum and mass diffusivities
Sherwood	Sh	Ratio of convective to diffusive mass transport

The mass transfer coefficient is used to incorporate the bulk flow and diffusive flow into one parameter, the Sherwood number *(Sh)*. The Ranz-Marshall correlation of the Sherwood number is used in forced convection, and the Grashof number is used in natural convection, which correlates the flow driven by density gradients in the fluid of varying composition.

$$\text{Forced Convection (velocity gradients): } Sh_F = 2 + 0.6\,\mathrm{Re}^{1/2}\,Sc^{1/3} = 2 + 0.6\left(\frac{2vR_{Nb}(t)}{\nu}\right)^{1/2}\left(\frac{\nu}{D_{Nb}}\right)^{1/3} \quad -(4)$$

$$\text{Natural Convection (density gradients): } Sh_N = 2 + 0.59\left[Gr_m Sc\right]^{1/4} = 2 + 0.59\left[\frac{\left(2R_{Nb}(t)\right)^3 g\Delta\rho}{\nu D_{Nb}}\right]^{1/4} \quad -(5)$$

The *Sh* number accounts for the fluid conditions and properties and is related to the mass transfer coefficient as follows:

$$\text{Forced Convection (velocity gradients): } k_F = \frac{Sh_F\left(D_{Nb}\right)}{2R_{Nb}(t)} \quad -(6)$$

$$\text{Natural Convection (density gradients): } k_N = \frac{Sh_N\left(D_{Nb}\right)}{2R_{Nb}(t)} \quad -(7)$$

This mass transfer coefficient is used in the dissolution equation to determine the kinetics of dissolution for particles in a liquid that is described by natural or forced convection. This expression also applies to the stagnant liquid case, for which $Sh = 2$ and the mass transfer coefficient becomes $k = \frac{D_{Nb}}{R}$. This permits us to rewrite equation (3) as:

$$N_{Nb} = -\frac{\rho_L k_{Nb}}{(\omega_{Fe})_{\ln}}\left(\omega_{Nb}^{*} - \omega_{Nb}^{\infty}\right) \qquad -(8)$$

For each fluid condition (*i.e.* stagnant, natural, or forced), this expression is modified in the following sections. However, it operates on the condition of mass transfer from the solid to the liquid in the form of mass per unit time (*i.e.* kg/sec).

$$\frac{dm_{Nb}}{dt} = -N_{Nb}A_{\text{int},Nb}$$

$$\rho_{Nb}\frac{dV_{Nb}}{dt} = -N_{Nb}A_{\text{int},Nb}$$

$$\rho_{Nb}dV_{Nb} = -\frac{\rho_L k_{Nb}}{(\omega_{Fe})_{\ln}}\left(\omega_{Nb}^{*} - \omega_{Nb}^{\infty}\right)A_{\text{int},Nb}dt$$

$$\rho_{Nb}\left(\frac{4\pi}{3}\right)d\left(R_{Nb}^{3}(t)\right) = -\frac{\rho_L k_{Nb}}{(\omega_{Fe})_{\ln}}\left(\omega_{Nb}^{*} - \omega_{Nb}^{\infty}\right)\left(4\pi R_{Nb}^{2}(t)\right)dt$$

$$d\left(R_{Nb}(t)\right) = -\frac{\rho_L k_{Nb}}{\rho_{Nb}(\omega_{Fe})_{\ln}}\left(\omega_{Nb}^{*} - \omega_{Nb}^{\infty}\right)dt \qquad -(9)$$

Since k_{Nb} is a function of R_{Nb}, further derivation cannot continue until it is determined whether the liquid is stagnant or convective. As was shown in (6) and (7), the Sherwood number for both natural and forced convection is a function of R_{Nb} as well.

7.2 Results for a Pure Substance

Prior to discussing the results of the Pure Substance Model, some discussion on the selection of parameters used in the model is necessary. These parameters are listed in Table 12. Firstly, this model only considers the dissolution of a sphere of pure niobium placed in thermal equilibrium with a stagnant pool of pure hot liquid iron (T=1600^{o}C). This can be justified in practice, because the atoms that the niobium sphere is in contact with are most probably iron, and least probably niobium atoms. Secondly, the constants such as diffusion coefficients of carbon[46] and niobium[47], and kinematic viscosity[48] of niobium in liquid iron have been extracted from the literature. Thirdly, three fluid velocities were chosen for the case of forced convection to cover a range of fluid conditions similar to fluid conditions identified in previous publications[24-30] on ferroniobium dissolution kinetics. Lastly, the density difference in the Gr number is due to the saturated solution density near the interface of the pure niobium sphere and pure liquid iron, which is saturated with Nb atoms and forms a density gradient with the atoms farther away from the interface.

Table 12 – Parameters used in modeling dissolution for a binary Fe–Nb system

Parameter	Symbol	Units	Value
Liquid density	ρ_L	kg/m^3	7,100
Solid density	ρ_{Nb}	kg/m^3	8,570
Diffusion coefficient of Nb	D_{Nb}	m^2/s	4.6e-9
Velocity	υ	m/s	0.1 / 0.3 / 0.9
Kinematic viscosity	ν	kg/m/s	7.21e-07

7.2.1 Stagnant Fluid

For a stagnant fluid, the mass transfer number is simplified to $k = \frac{D_{Nb}}{R}$. The dissolution kinetics is calculated from the following equation:

$$R_{Nb}(t)dR_{Nb} = -\frac{\rho_L D_{Nb}}{\rho_{Nb}\left(\omega_{Fe}\right)_{\ln}}\left(\omega_{Nb}^{*} - \omega_{Nb}^{\infty}\right)dt$$

$$\int_{R_{0,Nb}}^{0} R_{Nb}(t)\,dR_{Nb} = -\frac{\rho_L D_{Nb}}{\rho_{Nb}\left(\omega_{Fe}\right)_{\ln}}\left(\omega_{Nb}^{*} - \omega_{Nb}^{\infty}\right)\int_{0}^{t_f} dt \qquad -(10)$$

Considering that the dissolution of niobium occurs in a semi-infinite liquid, the concentration build-up of solute in the liquid with time is considered negligible and does not influence the dissolution rate. Therefore, only the time is integrated in the right-hand side of equation (10), which gives the final equation for dissolution of a niobium sphere in liquid iron:

$$R_{Nb} = \sqrt{R_{0,Nb}^2 - \frac{\rho_L D_{Nb}}{\rho_{Nb}\left(\omega_{Fe}\right)_{\ln}}\left(\omega_{Nb}^{*} - \omega_{Nb}^{\infty}\right)t} \qquad -(11)$$

It follows that the dissolution of Nb-rich particles observed in the microstructure of ferroniobium would be modeled. Such particles in the microstructure are approximated as spheres. The dissolution results for a 50μm diameter Nb sphere in pure liquid iron is shown in Figure 41. The initial size of the niobium sphere was chosen to represent the size of bcc Nb phase observed in the commercial ferroniobium. The assumption of pure liquid iron is a reasonable one, since prior to the addition of ferroniobium the liquid iron does not have a source of niobium.

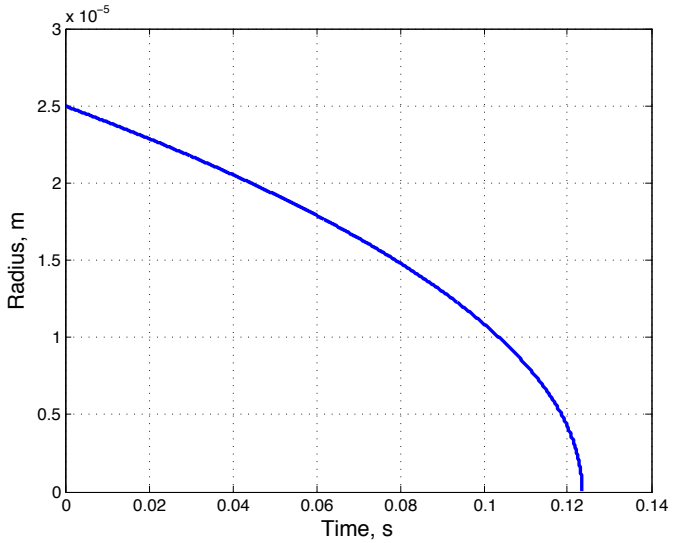

Figure 41 – Predicted time to complete dissolution of a niobium sphere in liquid iron

7.2.2 Forced Convective Fluid

Since the mass transfer coefficient now includes velocity and density gradients, a separation of terms is performed to group the like terms together on each side of the equation (9). Since there are two types of convection, two expressions must be derived. The derivations for these expressions are revealed in detail in section 10.3 on page 107.

Forced convection is given by equation (6). The grouping of like terms results in the following expression, which was integrated by MATLAB[****]:

$$\int \frac{R}{\alpha_F + \frac{1}{2}\alpha_F \beta_F R^{1/2}} dR = \int dt$$

$$t = \frac{4R_{Nb}^{3/2}}{3\alpha_F \beta_F} - \frac{4R_{Nb}}{\alpha_F \beta_F^2} - \left(\frac{32 \log\left(\beta_F R_{Nb}^{1/2} + 2\right)}{\alpha_F \beta_F^2} \right) + \left(\frac{16 R_{Nb}^{1/2}}{\alpha_F \beta_F^3} \right) \qquad -(12)$$

[****] All integrals calculated in this contribution were performed using MATLAB

Since many of the works cited in this contribution deal with dissolving solids with sizes larger than 1 cm under natural and forced convection conditions, the results graphically illustrated in Figure 42 will compare with these works for a niobium sphere with 2 cm diameter. The influence of the velocity of the liquid on the dissolution time is observed by comparing the velocities plotted in Figure 42. The effect of size on the dissolution time for a niobium sphere in a forced convective fluid is shown in Figure 43.

7.2.3 Natural Convective Fluid

Dissolution under natural convection conditions is given by equation (7). The grouping of like terms results in the expression below and is graphically illustrated in Figure 42. Since the density differences between the liquid iron and solid niobium are similar, the natural convection fluid has a smaller influence on the dissolution time, as compared to forced convection.

$$\int \frac{R}{\alpha_N + \frac{1}{2}\alpha_N \beta_N R^{3/4}} dR = \int dt$$

$$t = \frac{8R_{Nb}^{5/4}}{5\alpha_F \beta_F} - \frac{8R_{Nb}^{1/2}}{\alpha_F \beta_F^2} - \left(\frac{(16)4^{1/3} \log\left((1024)2^{1/3} + 1024 * \beta_F^{1/3} R_{Nb}^{1/4}\right)}{3\alpha_F \beta_F^{8/3}} \right) + \left(\frac{4^{1/3} \log\left(1024\beta_F^{1/3} R_{Nb}^{1/4} - (512)2^{1/3}\right) + 8/3}{\alpha_F \beta_F^{8/3}} \right) - \left(\frac{(-8/3)4^{1/3} \log\left((512)2^{1/3} - 1024\beta_F^{1/3} R_{Nb}^{1/4}\right)}{\alpha_F \beta_F^{8/3}} \right) \quad -(13)$$

The effect of size on the dissolution time for a niobium sphere in a natural convective fluid is shown in Figure 43.

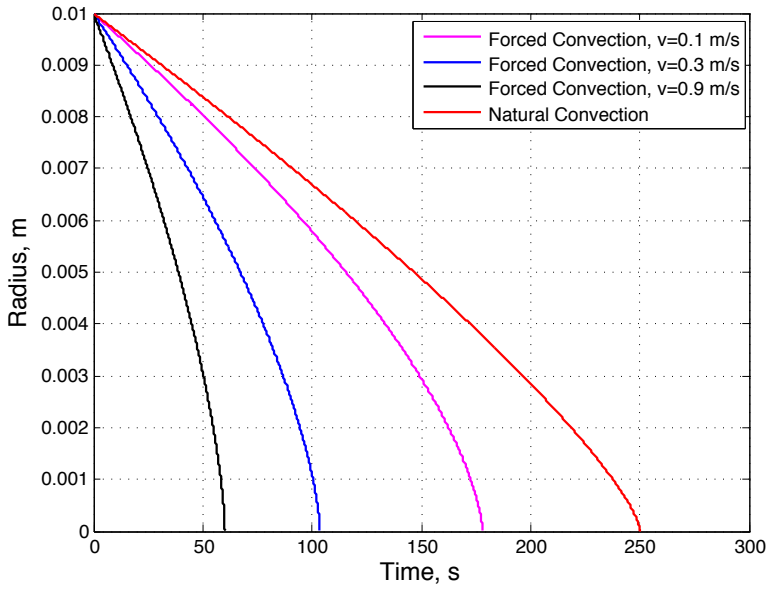

Figure 42 – Dissolution kinetics of a 2 cm diameter niobium sphere at 1600°C in liquid iron under forced and natural convection conditions

7.3 Comparison with a Model in Literature

The results of these convective models are compared with experimental observations from previous publications on the dissolution of niobium in liquid iron. Although Argyropoulos[28] linearly extrapolated the experimentally determined mass transfer coefficients in his calculations, the results have similar values but different trends. For this reason, the deviation between the model and Argyropoulos' calculations increases with increasing sample diameter, since the model accounts for a varying radius with time in the mass transfer coefficient. The results of the model and Argyropoulos' calculations are compared in Figure 43. Since no velocity values were calculated in Argyropoulos' work, the forced convective fluid has not been associated with a particular velocity. However, when the radius of the niobium sphere becomes small, the velocity of Argyropoulos' calculations approaches the velocity of 0.1 m/s in the model.

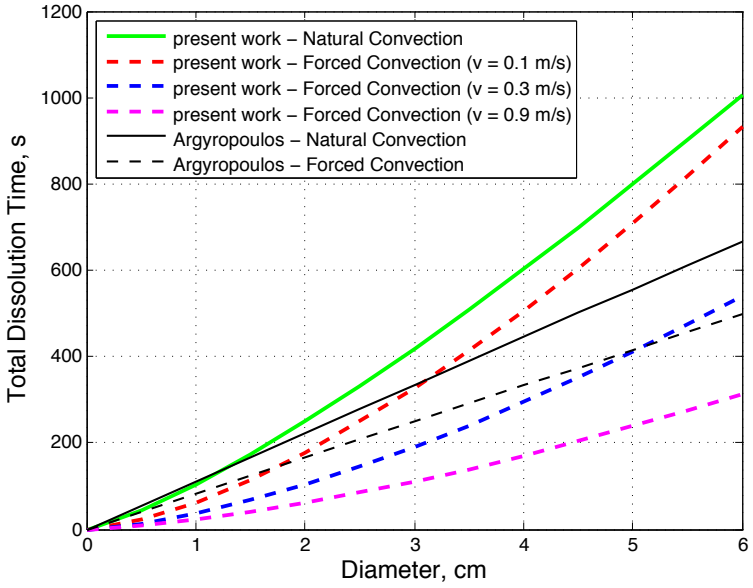

Figure 43 – The results of the pure substance model compared with experimental works published by Argyropoulos[28]

7.4 Mass Flux Balance for a Diatomic Compound

The mass flux balance for a diatomic compound†††† is similar to the pure substance case. Since the diatomic compound has two components, this complicates the model in several ways. First, the stoichiometry of the diatomic compound must be respected. This is based on the assumption of a pure diatomic compound without the consideration of vacancies or substitutional elements in the crystal structure, as well as a homogeneous composition throughout the compound. Second, the mass flux of both components must be equivalent to ensure that the condition of stoichiometry is maintained. In the consideration of mass fluxes, it must be noted that a coefficient must be applied for both atoms of the compound. If an amount of mass of the first component

†††† It should be noted that a diatomic compound is used in this contribution to refer to a compound containing two different atoms, which may occupy substitutional and/or interstitial positions in the crystal lattice.

is dissolved into the liquid, a corresponding amount of mass of the second component must also dissolve. Since molar fluxes give the clearest example of this, consider the dissolution of Nb_2C in liquid iron. The molar balance gives 2 Nb and 1 C; therefore, for every mole of niobium that dissolves into liquid iron, two moles of carbon must dissolve to maintain stoichiometry. In the case of a mass balance, these values must be converted from molar to mass fractions (see section 10.4 on page 110 for details). In the following expressions, variables will be used to hold values calculated in section 10.4.

For the Nb_2C phase:

$$\mathrm{Nb_2C} \rightarrow \varsigma \mathrm{Nb} + \lambda \mathrm{C}$$

$$\lambda N_{\mathrm{Nb}} = \varsigma N_{\mathrm{C}}$$

Equating the mass flux of niobium with the mass flux of carbon after equation (8):

$$\frac{\lambda \rho_L k_{Nb}}{(\omega_{Fe})_{\ln}}\left(\omega_{Nb}^{*} - \omega_{Nb}^{\infty}\right) = \frac{\varsigma \rho_L k_C}{(\omega_{Fe})_{\ln}}\left(\omega_C^{*} - \omega_C^{\infty}\right) \qquad -(14)$$

For the NbC phase:

$$\mathrm{NbC} \rightarrow \psi \mathrm{Nb} + \xi \mathrm{C}$$

$$\xi N_{\mathrm{Nb}} = \psi N_{\mathrm{C}}$$

Equating the mass flux of niobium with the mass flux of carbon after equation (8):

$$\frac{\xi \rho_L k_{Nb}}{(\omega_{Fe})_{\ln}}\left(\omega_{Nb}^{*} - \omega_{Nb}^{\infty}\right) = \frac{\psi \rho_L k_C}{(\omega_{Fe})_{\ln}}\left(\omega_C^{*} - \omega_C^{\infty}\right) \qquad -(15)$$

The condition of flux equality ensures that each component will dissolve in conjunction with the other and the equilibrium concentration at the interface will maintain a steady state condition during the dissolution process. It is important to point out that there exists

a unique solution to (14) and (15) since the mass fractions ω_i^* and ω_j^* (where *i*=Nb,Ti and *j*=C,N) are directly related to each other by the liquidus boundary of a compound with liquid iron (*e.g.* NbC). In other words, a mass fraction of niobium that lies on the phase boundary in equilibrium with liquid iron has a corresponding mass fraction of carbon. Since the flux equality involves equilibrium interfacial concentrations, our attention is turned to the description of the solid/liquid equilibrium.

In a ternary system, an infinite number of tie lines may be drawn from a stoichiometric compound to its liquidus phase boundary (Figure 44). Therefore, it is necessary to impose a condition of flux equality to determine which composition is the equilibrium one. In other words, the flux equality condition must be solved using compositions along the liquidus phase boundary, along with the condition of phase equilibrium.

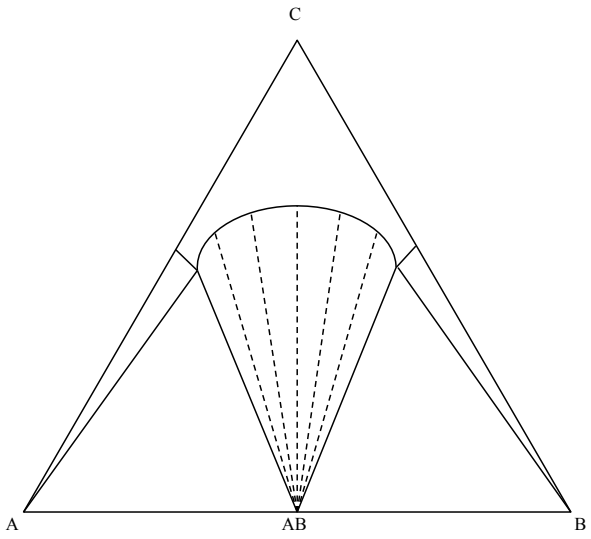

Figure 44 – An infinite number of tie lines may be drawn from the pure compound AB to its solubility phase boundary with component C

7.4.1 Determination of the Liquidus Phase Boundary

The manner in which liquid iron is brought into equilibrium with diatomic compounds such as NbC and Nb_2C has been approximated by Wagner's interaction parameter formalism. The solubility product of a compound is calculated using Gibbs energy according to equation (15). The data for calculating K_{sp} can be found from a SGTE data source. Wagner's formalism makes use of the solubility product and interaction parameters to calculate the equilibrium compositions. In the expressions below, the energy released when Nb_2C dissolves in liquid iron at 1600°C and its corresponding solubility product are given. The expression for calculating the solubility curve with published data for the first order interaction coefficients is given by (15).

$$Nb_2C \rightarrow 2Nb + C$$
$$\Delta G_{Nb_2C}^{1873K} = 123{,}082.57 \text{ J/mol}$$
$$K_{sp}^{Nb_2C} = 3.6941e-04$$

$$\log K_{sp}^{Nb_2C} = \log(\%C)(\%Nb)^2 + \left(2e_{Nb}^{Nb} + e_C^{Nb}\right)\%Nb + \left(2e_{Nb}^{C} + e_C^{C}\right)\%C \qquad -(15)$$

Although Wagner's formalism is widely used by metallurgists, it is limited because in most systems only first-order interaction parameters have been published. It can be easily comprehended that difficulties will arise when the effect of second-order interaction parameters on the equilibrium composition is non-negligible. For example, consider the Fe–Nb–C system in Figure 45; the liquidus curve given by the TCFE2 database of Thermo-Calc is dissimilar to the liquidus curve calculated by Wagner's formalism for the equilibrium between liquid iron and the diatomic compound Nb_2C.

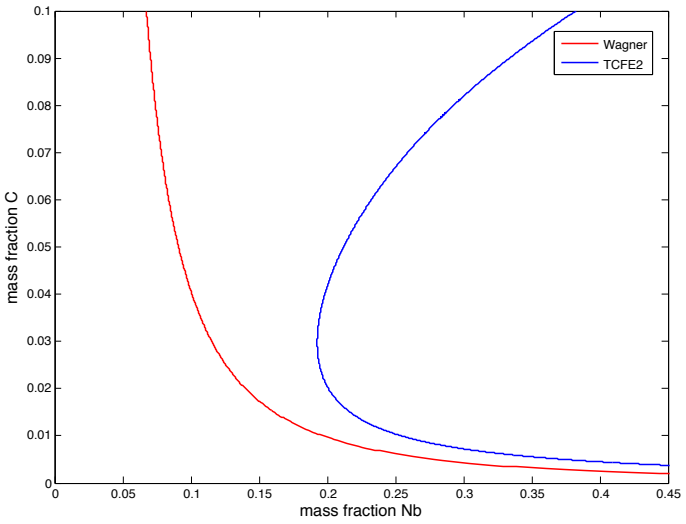

Figure 45 – Comparison of the liquidus curves generated by ThermoCalc database TCFE2 with Wagner's formalism for the phase Nb_2C

In order to maintain an accurate description of the liquidus curves, the liquidus curve from the ternary Fe–Nb–C phase diagram will be generated by ThermoCalc and used in the calculations of flux equality. Once the equilibrium concentrations defined by the ternary phase diagram are determined in conjunction with the flux equality, the dissolution kinetics can be modeled.

Essentially, the physics of the diatomic model is identical to the pure substance model. However, since a flux equality expression is used to determine the equilibrium concentrations, the flux expression for either component may be used to predict the dissolution kinetics of a diatomic compound in stagnant liquid where diffusion is the dominant mechanism. Actually, modeling the dissolution kinetics of both components of the diatomic compound will serve as an internal check that the code is consistent for both components. In the results that follow, the prediction of time to complete dissolution is given for one fcc diatomic compound, NbC, and one hcp diatomic compound, Nb_2C.

7.5 Results of Diatomic Compound Model for NbC

For each diatomic compound, the flux equality will be generated and supplied alongside the predicted dissolution kinetics. The parameters used in the modeling are tabulated in Table 13. One note of importance is that the density of the solid on the liquid side of the interface is now a saturated solution density, since the liquid is made up of two components (*i.e.* Nb and C).

Table 13 – Parameters used to model dissolution of NbC and Nb_2C in liquid iron

Parameter	Symbol	Units	Value
Liquid density	ρ_L	kg/m^3	7,100
Solid density	ρ_S	kg/m^3	7,800
Diffusion coefficient of Nb	D_{Nb}	m^2/s	4.6e-09
Diffusion coefficient of C	D_C	m^2/s	11e-09

7.5.1 Stagnant Fluid

As has been shown on page 72 for a stagnant fluid, the mass transfer number is simplified and the dissolution kinetics for NbC can be modeled by the following equations:

$$R_{Nb} = \sqrt{R_{0,Nb}^2 - \frac{\xi \rho_L D_{Nb}}{\rho_{Nb_2C}} \left(\omega_{Nb}^* - \omega_{Nb}^\infty\right) t} \qquad -(16)$$

$$R_{Nb} = \sqrt{R_{0,Nb}^2 - \frac{\psi \rho_L D_{Nb}}{\rho_{Nb_2C}} \left(\omega_{Nb}^* - \omega_{Nb}^\infty\right) t} \qquad -(17)$$

Based on these expressions, the result for flux equality and dissolution of diatomic compounds such as NbC in liquid iron are shown in Figure 46. For the Nb_2C particle, the

dissolution kinetics could not be established, because flux equality was not attained. The finer details of this problem are revealed in section 7.6.2 on page 84.

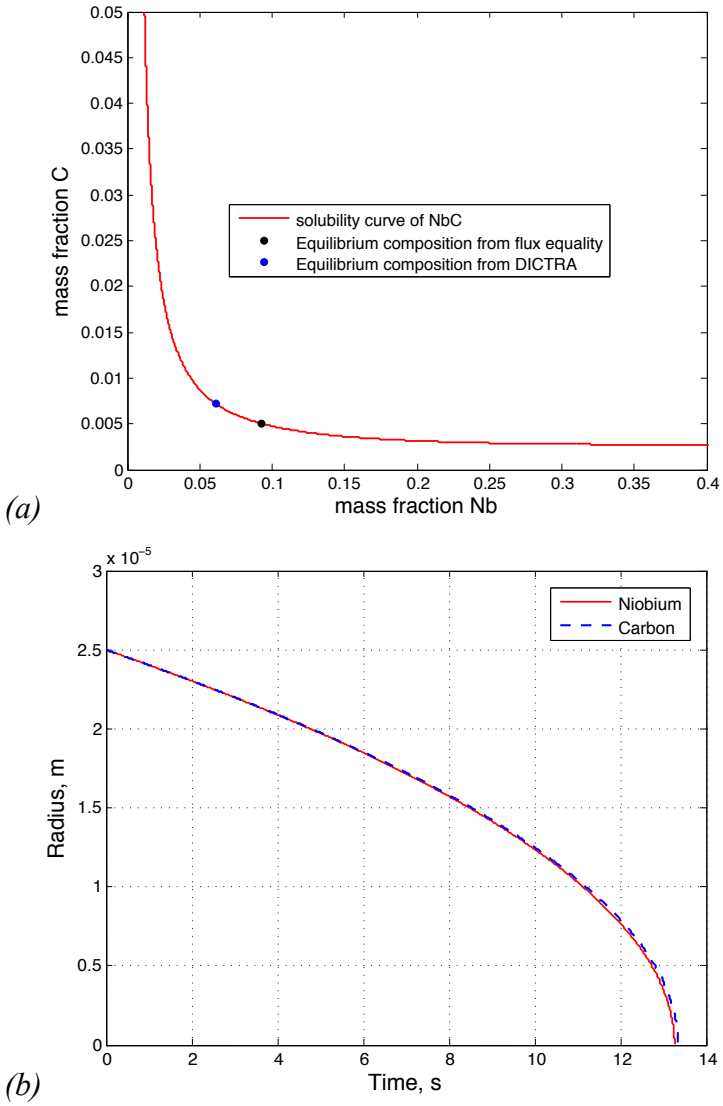

Figure 46 – The *(a)* flux equality and equilibrium compositions, and *(b)* dissolution kinetics predicted for NbC in pure liquid iron at 1600°C

7.6 Comparison with Models in Literature

DICTRA is a commercial software that employs the description of thermodynamic and mobility databases to calculate solid-solid and solid-liquid diffusional

transformations. The software is limited in that it can only take into account the stagnant fluid condition and convective conditions are not calculable. For our purposes this limitation is satisfactory because the size of particles in liquid steel is tens of microns in diameter. It is well known[49] that micron-sized particles have a negligible slip condition in the fluid they are travelling in. In other words, these small particles can be considered to travel with the fluid flow and remain in a locally stagnant condition. As a result, the dissolution of NbC and Nb_2C in stagnant liquid iron can be modeled utilizing this software and compared with the diatomic compound model.

7.6.1 Simulation Results of DICTRA

It should be realized that since the developers of DICTRA have programmed a user interface, the simulation results of the dissolution of NbC and Nb_2C must be interrogated to determine their veracity. It is acknowledged that although the results differ between DICTRA and DCM, the order of magnitude of the time to dissolve NbC and Nb_2C in liquid iron is preserved. Such differences can be attributed to the selection of parameters by developers of the software (*e.g.* diffusion coefficients). The diffusion coefficient used by DICTRA for any element in the liquid is $1x10^{-9}$ m^2/s. This is the major cause for observed variance in dissolution times since the equilibrium compositions at the interface will be affected, as well as dissolution kinetics (see section 10.5). However, since the order of magnitude was preserved between the two models, the order of magnitude for the kinetics of dissolution is also preserved. The results for dissolution of NbC and Nb_2C in pure liquid iron at 1600°C are given in Figure 47.

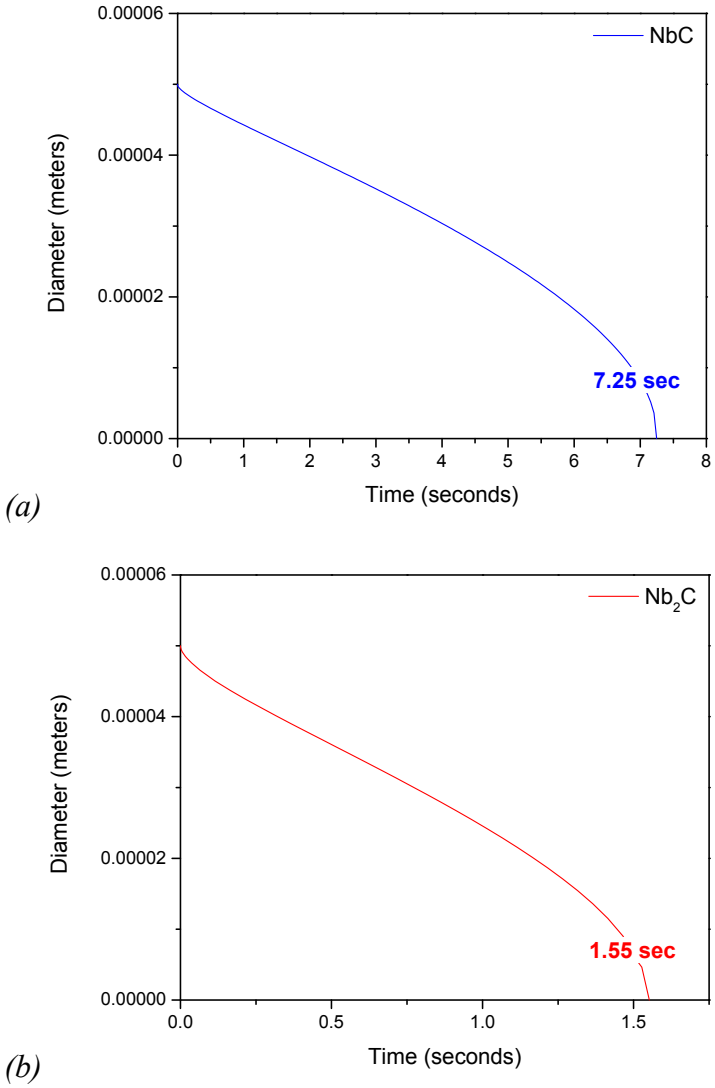

Figure 47 – Results from DICTRA for the dissolution of *(a)* NbC and *(b)* Nb_2C spheres in liquid iron at 1600°C

7.6.2 The Flux Equality

Since the DCM cannot determine the flux equality for dissolution of Nb_2C, a natural question is asked: how is DICTRA able to produce a result? To answer this question, the solubility curves for each compound in equilibrium were extracted from the ternary phase diagrams and plotted along with the equilibrium compositions defined by

DICTRA at the interface, and the stoichiometric line defined by the flux equality. Although a brief glance at Figure 48 would indicate that the results are as expected for NbC, one should note that for the Nb_2C compound there is a discrepancy that must be resolved when considering the compositions at the interface. The following paragraphs will attempt to shed light on the cause of this inconsistency.

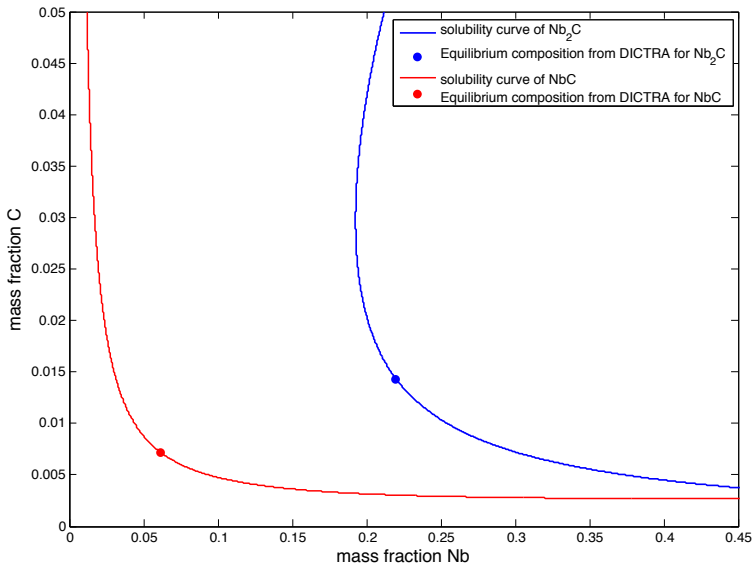

Figure 48 – *(a)* the Nb_2C and NbC liquidus boundaries, and the equilibria established by DICTRA on these boundaries

To generate the solubility curve for Nb_2C for every combination of compositions of Nb and C, all phases were suppressed other than the hcp and liquid phase. In this way, the equilibrium composition determined by DICTRA can be graphically illustrated to exist precisely on the solubility curve of Nb_2C with liquid iron, as expected. However, when inspecting the Fe–Nb–C system in Figure 49, one will notice that there is a composition range for which the Nb_2C phase exists. In other words, a thermodynamic competition with the fcc phase prevents the hcp phase from forming at all combinations

of Nb and C concentrations. Therefore, the interfacial equilibrium composition calculated by DICTRA resides on the metastable continuation of the Nb_2C solubility curve.

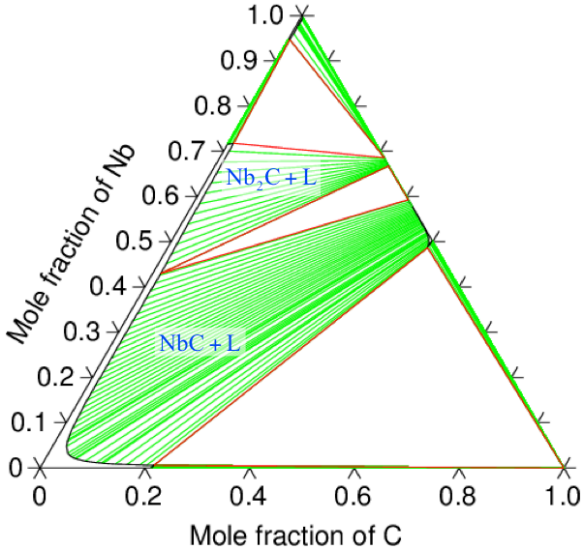

Figure 49 – The ternary Fe–Nb–C system from TCFE2

The dissolution of the Nb_2C phase is questionable because an equilibrium composition with liquid iron that satisfies the flux equality, and is situated on the most thermodynamically stable liquidus boundary, is not achieved.

A natural question is asked: what really does occur? Consider the following scenario: the Nb_2C phase undergoes a solid-solid transformation to the NbC phase at the interface (refer to Figure 50). Since the NbC phase is able to establish an equilibrium composition at the interface with liquid iron that satisfies flux equality, and resides on the most thermodynamically stable phase boundary, it will form at the interface between Nb_2C and liquid iron. Indeed, it is a challenging task to cook up a possible scenario and provide all necessary details, but consider the following simple sequence of events: first, Nb and C are at the interface contacting liquid iron; Nb leaves the surface and solves into

the liquid iron, leaving a niobium poor shell; enough niobium leaves so that a structural rearrangement occurs at the interface forming a fcc shell of the NbC phase. This flux of niobium occurs unhindered, since Nb readily dissolves in liquid iron. Once an NbC shell has formed-one can imagine it to be a monatomic layer or two-it establishes equilibrium with liquid iron in a manner shown by Figure 48. This scenario is illustrated in Figure 50 where the total mass flux of niobium is the sum of N_{Nb}^{1} and N_{Nb}^{2}, while the total mass flux of carbon is simply N_C.

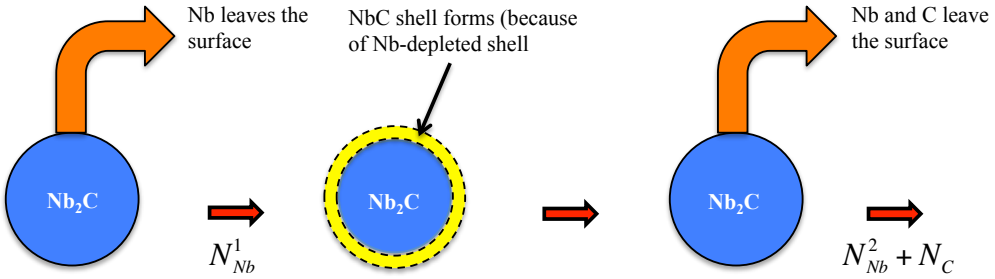

Figure 50 – A proposed scenario of the dissolution of Nb_2C in liquid iron

It is assumed that the mass flux equality between niobium and carbon results in an equilibrium composition that coincides with the point established by DICTRA along the liquidus phase boundary of Nb_2C. In other words, the total flux of Nb and the total flux of C coincide with the calculations of DICTRA, even though the precise mechanism is not revealed. This can be attributed to a rapid structural transformation and subsequent dissolution. Niobium is always available to dissolve into the liquid iron, since it is always at the interface. For this reason, the dissolution kinetics determined by DICTRA is assumed to be reasonably accurate.

7.7 Results of Diatomic Compound Model for Nb_2C

Considering the mechanism proposed in the previous section, as well as what is observed in DICTRA, the entire solubility curve for Nb_2C in liquid steel is used in determining the equilibrium compositions at the interface. In the case of a stagnant fluid, the dissolution kinetics for Nb_2C are expressed as follows:

$$R_{Nb} = \sqrt{R_{0,Nb}^2 - \frac{\lambda \rho_L D_{Nb}}{\rho_{Nb_2C}} \left(\omega_{Nb}^* - \omega_{Nb}^\infty \right) t} \qquad -(18)$$

$$R_C = \sqrt{R_{0,C}^2 - \frac{\varsigma \rho_L D_C}{\rho_{Nb_2C}} \left(\omega_C^* - \omega_C^\infty \right) t} \qquad -(19)$$

The predicted dissolution kinetics of the Nb_2C phase is illustrated in Figure 51.

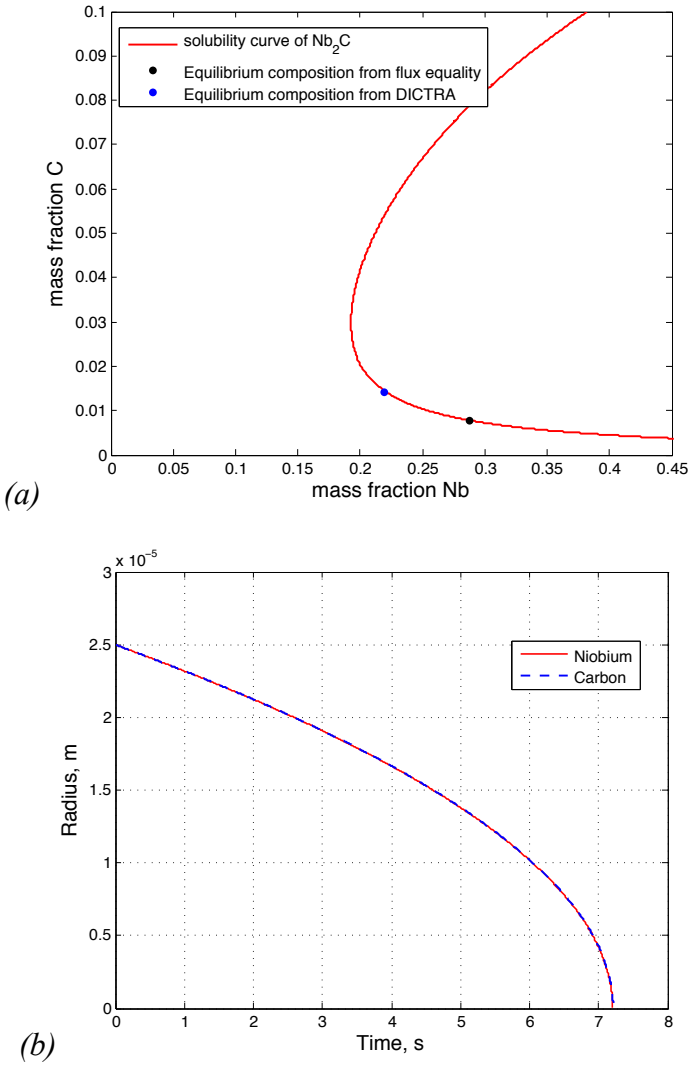

Figure 51 – The *(a)* flux equality and equilibrium compositions, and *(b)* dissolution kinetics predicted for Nb_2C in pure liquid iron at 1600°C with an unbounded solubility curve

7.8 Experimental Challenges in Measuring Dissolution Kinetics

Although the experimental efforts to determine dissolution kinetics may appear to be simple, it is quite difficult. There are at least three complications making experiments challenging and questioning their qualitative usefulness. The first difficulty is geometrical. The losses of mass and gains in Nb concentration are to be related to the rate

of dissolution and expressed in terms of number of moles of NbC leaving a unit surface per unit time. If an initial shape of the specimen is geometrically convenient[‡‡‡‡], and if it does not change during the experiment, then such a problem is mathematically straightforward. Pure carbides are so much harder than ferroalloys that their machining yielding a desired shape is prohibitively expensive. In view of this, it is likely that a piece of NbC made *via* arc melting will be used as such. Although its shape can hardly be characterized as perfectly opportune, accumulated experience suggests that the specimen will closely resemble a spherical cap, *i.e.*, a mathematically manageable shape.

The second intricacy is non-isothermality. If a piece of carbide placed in the melt is not hot enough, then its dissolution can commence only after a complete re-melting of an iron crust that formed upon the initial contact of NbC with molten metal. This delay can be avoided if the sample is preheated. It is suggested to keep it near the melt's surface and rely upon radiation. A two-wavelength pyrometer displaying a correct temperature regardless of the emissivity of an object it is aimed to will be used to ensure that carbide's temperature is close to that of the liquid. For insurance, temperature can simultaneously be measured using a tiny B-type thermocouple [§§§§] or even less exotic R- or S-types inserted in a small hole drilled on the surface. Another cause of non-isothermality is a continuing usage of power during the experiment. It will be attempted to measure temperature oscillations as well as to outline a temperature field inside the crucible and use this information for estimating a corresponding error in determining kinetic characteristics of NbC dissolution.

[‡‡‡‡] Cylindrical or spherical
[§§§§] Pt 30%Rh – Pt 6% Rh

The third and the most important difficulty in interpreting experimental data lies in the conditions which dissolution occurs. It must be emphasized that for the problem in hand, dissolution is not a pure diffusionally controlled process. In the real industrial world, it takes place either in a stagnant liquid[*****] or in a stirred (inductively or mechanically) one. A large dissolving object may either rest at the bottom or float at the surface depending on its density. A small object may be taken by a moving liquid and travel with it at almost the same, or slightly lesser, speed. This speed, *i.e.*, the intensity of fluxes, depends on whether the liquid experiences a natural or forced convection as well as on the geometry of the crucible used in experiments. It must be admitted that even though it is indeed possible to record a change of mass and an increase of Nb concentration in the course of ferroniobium dissolution, it is not clear how to relate kinetic information extracted from such measurements to particularities of dissolutions conditions. It might be advantageous to design two kinds of experiments. The first type would correspond to the lowest possible rate of dissolution; in the second one, the rate would be maximized. Consequently, it will be possible to estimate time in which a piece of NbC (or, Nb_2C) having a certain size will completely dissolve. Identifying such limiting experimental conditions is not a trivial task by itself; however, in this contribution, the experimental challenges are left for another.

[*****] Within which convectional fluxes exist, indeed.

8 Case Study: Coarse Particles in Continuously Cast HSLA Steel

To substantiate the claim of coarse particles observed in centerline regions of HSLA steels as outlined in section 2 on page 5, it is useful to dedicate a portion of this contribution to the industrial problem. After examining the microstructure of ferroniobium and its phase portrait, combined with the observation of Nb_2C particles in the microstructure and their dissolution behaviour in liquid steel, the final section is dedicated to a case study of a HSLA steel sample that contains coarse particles. This section will investigate coarse particles at the centerline of HSLA slabs, and will include characterization of these particles as well as a hypothesis regarding their origin.

8.1 Characterization of Coarse Particles

In collaboration with the Steel Research Centre at McMaster University, the steelmaking company Evraz North America submitted samples of an as-cast steel slab. The samples were taken from a region that contained both the centerline and quarterline positions. The composition of the HSLA steel is given in Table 14; the un-etched microstructure of a region near the centerline is shown in Figure 52(a). Aside from the expected inclusions (*i.e.* MnS, oxides, *etc*), coarse particles were observed near centerline cracking, ranging from 1 to 10 microns in the longest dimension. Two types of particles were identified based on geometry and color (due to etching from alumina polishing). The first particle type has an irregular shape and is soft yellow in colour. The second particle type has highly faceted interfaces and is a gold color. Since the indicators of shape and

color are aesthetic in nature, further investigation was performed to characterize these coarse particles and identify their composition and crystal structure.

Table 14 – Composition of HSLA steel in wt. % (as per manufacturer)

C	Mn	S	P	Si	Cu	Ni	Cr
0.029	1.22	0.001	0.007	0.19	0.11	0.05	0.03
V	**Nb**	**Mo**	**Sn**	**Al**	**Ca**	**Ti**	**N**
0.061	0.043	0.024	0.007	0.041	0.0042	0.009	0.0083

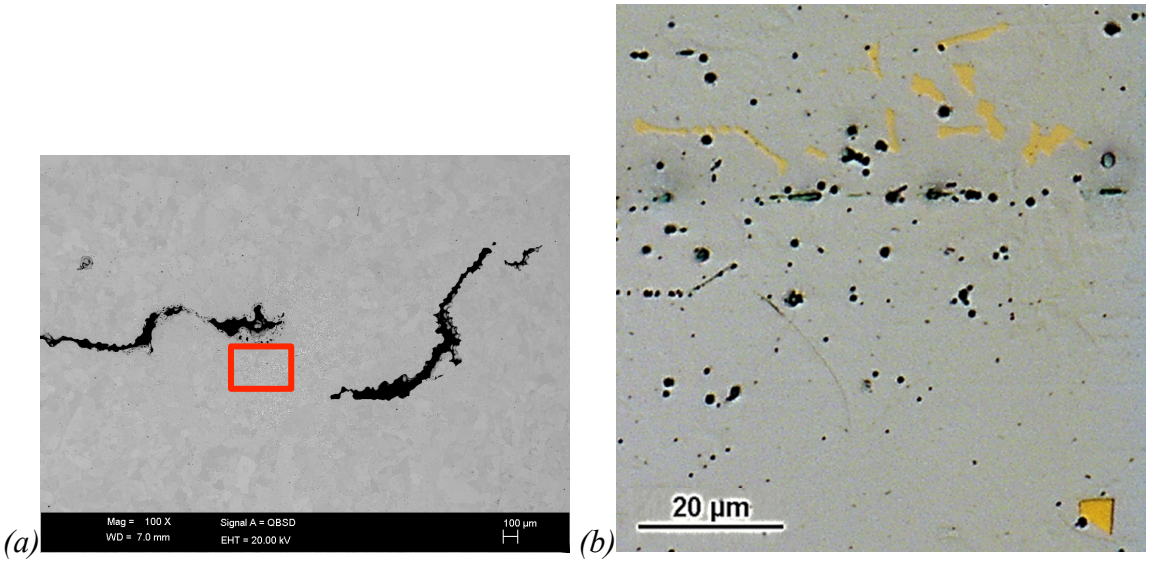

Figure 52 – *(a)* SEM micrograph of the region where coarse particles were observed; the centerline cracking is commonly associated with nearby particles, and *(b)* optical micrograph of particles at centerline region of HSLA steel.

To determine the composition of the coarse particles, SEM-EDS in BSE mode was utilized. The two particles observed in optical microscopy were assumed to have a different composition and are shown in Figure 52(b). The particles have a different grey-scale contrast due to the atomic number, an indication that the particles differ compositionally. The analysis from SEM-EDS is shown in Table 15; particle 1 is a Nb-rich compound while particle 2 is Ti-rich. It should be noted that Particle 1 is almost entirely

composed of Nb as the main substitutional component, while Particle 2 is a solid solution of about 75 wt. % Ti and 25 wt. % Nb. Based on the SEM-EDS results, it cannot be determined if these particles are metallic compounds or if they are carbides or nitrides The reason is because light non-metallic elements such as carbon, nitrogen and oxygen cannot be measured in SEM-EDS.

Therefore, EBSD was used to determine the crystal structure of these particles, and it was found that the particles were fcc crystal structure in a matrix of ferrite (Figure 53). Although the Ti-rich particle and the Nb-rich particle were both assigned the color blue in the EBSD image, the lattice parameters were too close to differentiate between a fcc nitride, fcc carbide, or fcc carbonitride.

Table 15 – SEM-EDX results of the two particles identified in Figure 53

Location	wt. % of Elements			Predicted Phase from EDX and EBSD Analysis	Crystal Structure from EBSD
	Fe	Ti	Nb		
1	3.17	1.47	95.36	Nb(C,N)	fcc
2	2.89	73.55	23.55	(Ti,Nb)(C,N)	fcc

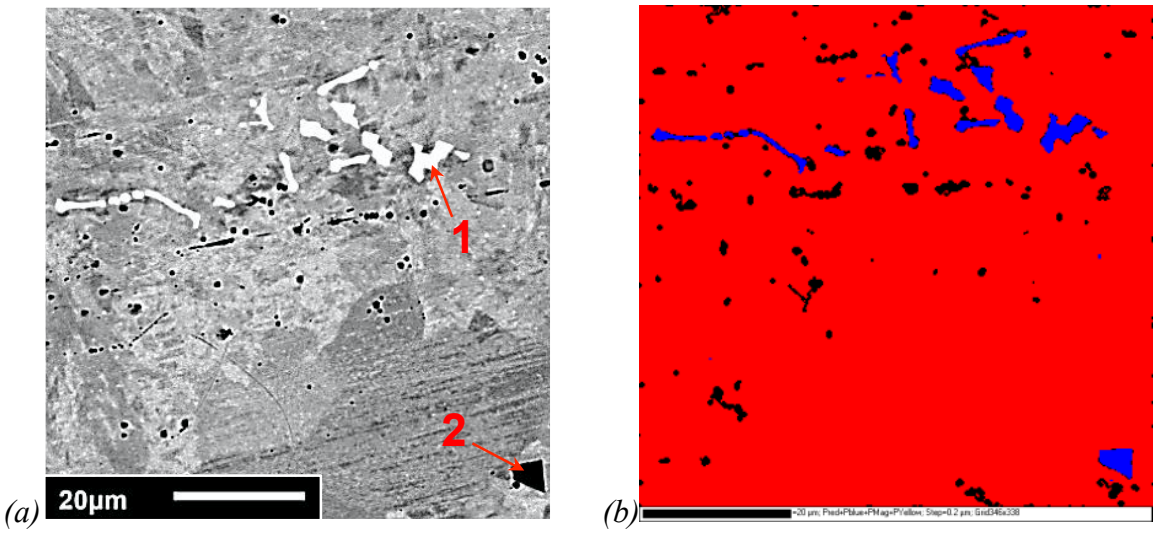

Figure 53 – *(a)* SEM-BSE image of the two types of particles located near the centerline, and *(b)* a corresponding EBSD image

8.2 What is the Origin of Coarse Particles in HSLA Steel?

The observation of coarse particles in Figure 53 is leads to the question: where did these particles come from? Why are the particles aligned along the centerline[†††††], rather than being dispersed throughout the metal matrix with a random alignment? In many cases, the existence of coarse particles has been discussed in the literature[5-10], but consideration of the cause of their alignment along the centerline region has been neglected. In the following sections, the centerline region will be analyzed to determine how the centerline differs from the rest of the sample.

8.2.1 Composition Profile in HSLA Steel Slab Sample

In this section, the composition profile of the slab will be investigated with the aim of determining the origin of the coarse particles near the centerline. For this reason, a piece of HSLA cast slab provided by Evraz was sectioned and the centerline cracking was

[†††††] The centerline refers to the last region to solidify, rather than the geometrical centerline; this region is determined by the casting conditions

exposed (Figure 54). Upon identifying the centerline region, the sample was machined to remove all oxides, foreign material, and most importantly, to remove the centerline crack from the surface of the sample. The removal of the crack was necessary to ensure that there was no leaks during glow discharge optical emission spectroscopy (GDOES).

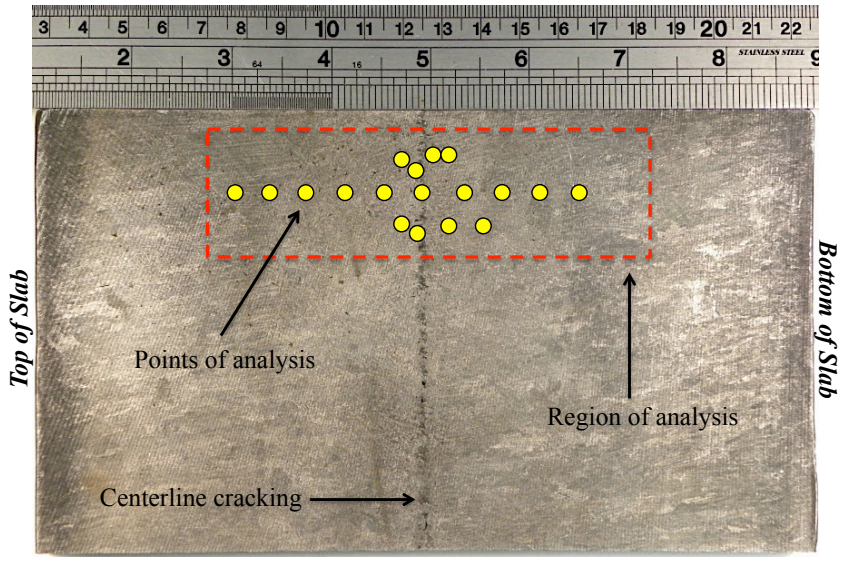

Figure 54 – Sample of an as-cast HSLA steel slab and additional information

The technique of GDOES was performed to determine the concentration of the elements at select positions (Figure 55). At areas near the centerline region, a number of spots were taken to obtain a higher resolution of data points with the aim of extracting more information from the centerline region. The resolution was difficult to obtain otherwise, since the 4 mm spot size of the instrument was the limiting factor.

The results of GDOES are shown in Figure 55. Since the compositions of different elements vary, the results are presented in three graphs, all from the same slab sample analysis. There are three patterns that are observed in these results for nearly all elements (exceptions are Al, V, N): first, there are two smaller spikes on either side of the

centerline region. These smaller spikes occur at distances less than 5 mm from the centerline. Since the resolution of the spot size in the GDOES instrument is 4 mm, identifying the precise position of these peaks from the centerline would most likely result in them approaching the centerline. However, at distances no further than 5 mm from the centerline, this small spike is observed. Second, immediately following these small spikes, there is a decrease in concentration as the position of analysis moves closer towards the centerline. The last pattern observed in the results is a large spike in composition at the centerline region. In the sections that follow, a possible explanation for these patterns will be presented. However, the justification of the use of these results will be offered first.

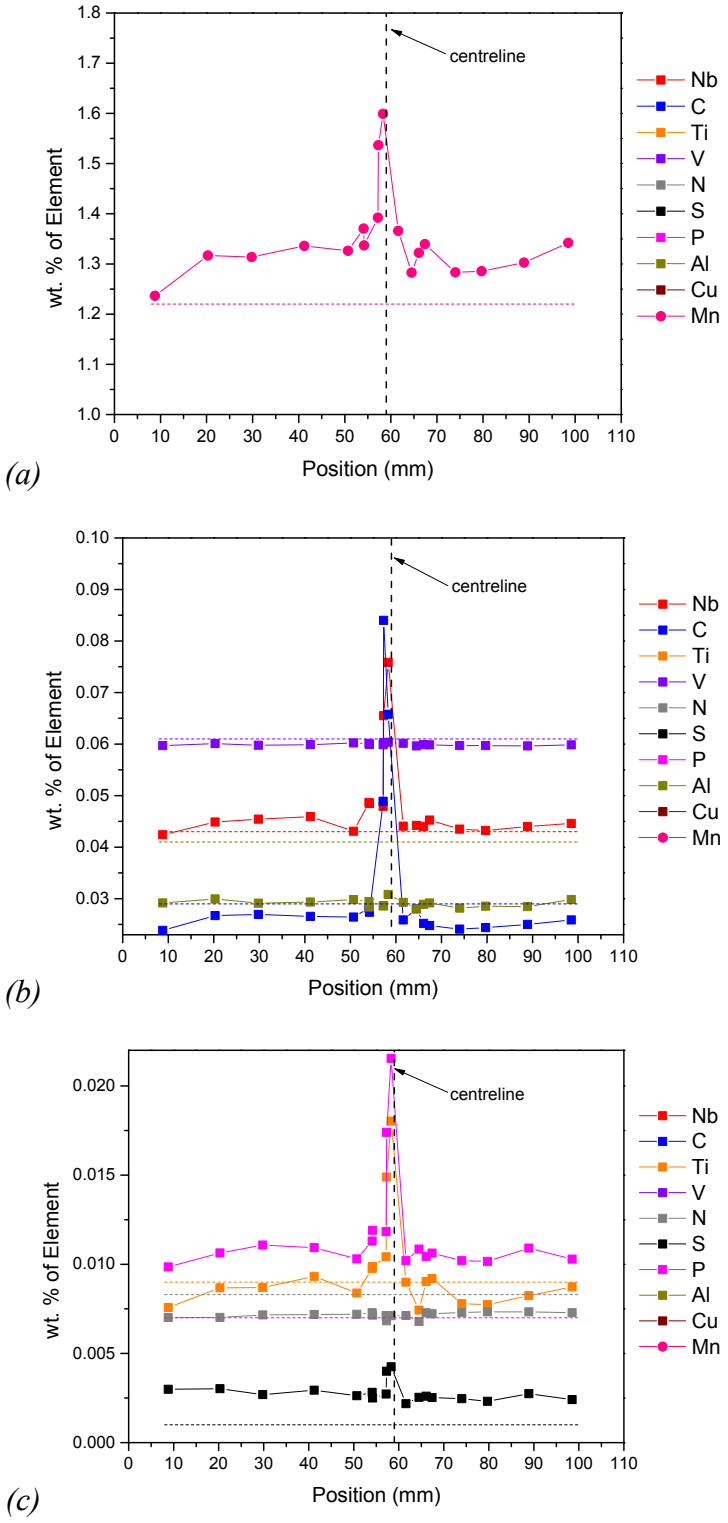

Figure 55 – GDOES analysis of as-cast HSLA steel slab; the dashed lines are the bulk compositions given in Table 14

8.2.2 Comparison of Composition Profiles with Literature

The results presented were from a single analysis of the HSLA slab sample; for this reason, a statistical defect can be expected. However, metallurgists who are interested in the concentration of elements near the centerline have performed this type of analysis[‡‡‡‡‡] in previous works[50-52]; in almost every case, publications attribute the concentration of elements at the centerline to macrosegregation. Therefore, a comparison of these results and the distinct similarity of patterns with the literature may give confidence to the results presented in Figure 55 as well as the arguments presented about why these patterns are observed, especially when considering the fact that different types of steels are compared with the same patterns near the centerline. It must also be noted that this is a case study, and not an exhaustive analysis of the problem stated at the beginning of this section.

When comparing the GDOES results with previous works on analyzing the composition profile of select elements (*i.e.* C, Mn, S) across the slab width, there are comparable results. Consider the work of Moore *et al.*[50], who analyzed the macrosegregation of C in a medium carbon steel slab with ICP analysis. Although ICP-OES was used, a similar pattern is observed in Figure 56.

[‡‡‡‡‡] That is, measuring the concentration of elements in regions far from the centerline, and comparing them with the conentrations at the centerline.

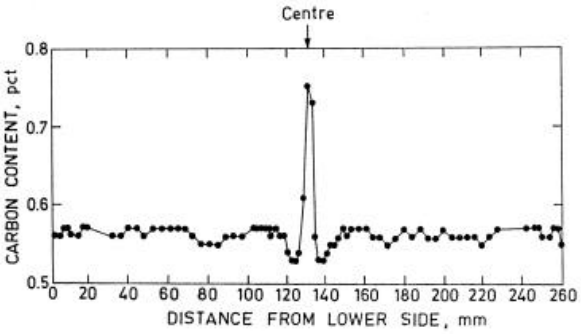

Figure 56 – A typical concentration profile in continuous slab casting of medium carbon steel[50]

Another example from the literature is the macrosegregation profiles published by Aminorroaya-Yamini[51] who analyzed the compositions of C, P, and Nb in the centerline region of HSLA pipeline steels (Figure 57). The analysis was performed using a very accurate technique called EPMA; this technique provided a superior resolution of data points that produces similar patterns with the current study.

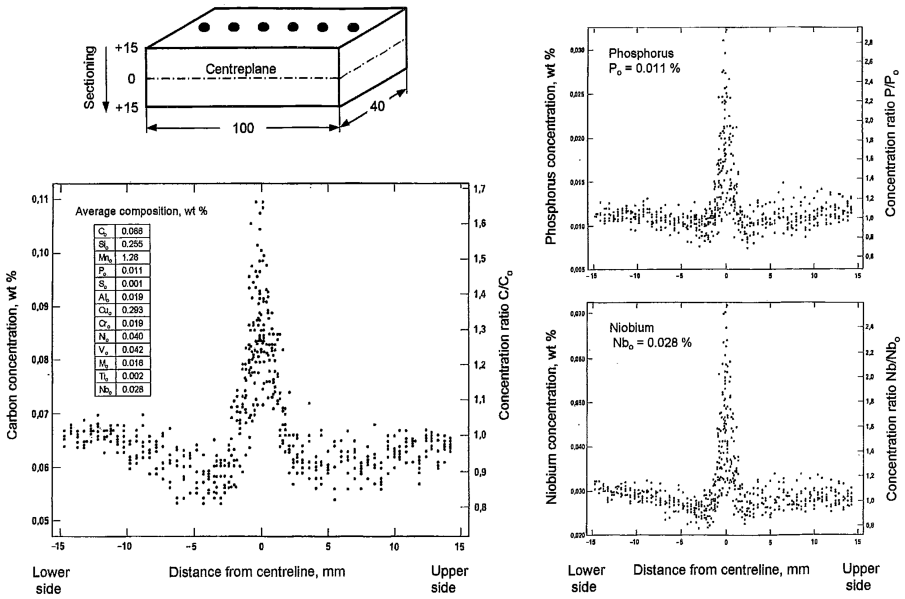

Figure 57 – Segregation profiles of C, P and Nb at the centerline of an as-continuously cast HSLA steel slab[51]

The last example from the literature is Presslinger *et al.*[52] who measured the compositions of elements C, Cr, Si, and Mn from the surface of the slab to the centerline of the slab. The concentrations were measured by EPMA; however, a poor resolution of data points was performed, such that only the concentration spike at the centreline is captured in these results. Still, as shown in Figure 58, the results contain a similar pattern as the results of this current study.

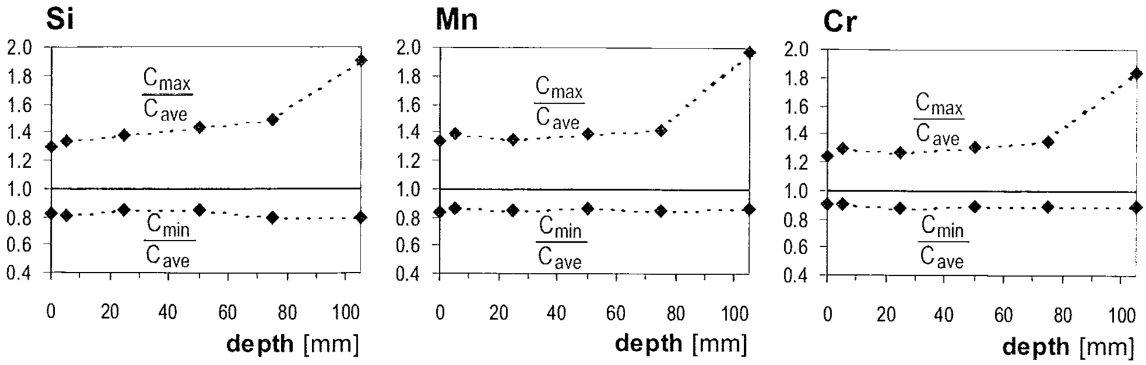

Figure 58 – Macrosegregation of elements in a dual-phase (DP) steel[52]

8.2.3 Proposed Origin of Coarse Particles

In most cases where coarse particles are observed in steels, the cause is attributed to macrosegregation. To review, macrosegregation is a global phenomenon coming from the accumulation of microsegregated regions during solidification. The accumulation of microsegregated solutes may be caused by a number of factors related to casting conditions, such as bulging of the slab between the rollers which moves the liquid in the axial direction, and convective and thermal-solutal effects that move the interdendritic liquid out of the interdendritic regions and mix it with the rest of the bulk liquid. The microsegregated solutes are move from the interdendritic regions out in front of the solidifying front, causing the liquid ahead of the solidifying front to be enriched with

solute. The end result is an increase in solute concentration from the outer edge of the solidifying slab to the inner core where final solidification takes place.

The increase in concentration near the centreline may be high enough to stimulate the formation of coarse precipitates in the liquid. This is be possible for two reasons: first, the particles are thermodynamically stable, and second, the concentration is so high that once heterogeneous nucleation occurs, the driving force to attach more atoms to this surface is low enough that coarsening of these particles occurs (*i.e.* micron-sized particles develop). Indeed, in the enriched liquid at the centreline there are enough atoms to form large particles.

Therefore to return to the pattern of the GDOES results, as well as the results in literature, it is proposed that two phenomena occur: first, macrosegregation occurs as solidification progresses, slowly increasing the concentration of solutes in the liquid with time. As the liquid solidifies, there is a slight increase of solute concentration in the matrix far from the centreline; this concentration increase becomes more pronounced as solidification progresses toward the centreline. The second phenomenon occurs once the liquid is enriched with solutes. The enriched liquid stimulates the formation of particles and these particles nucleate heterogeneously on another surface. Since there is an excess of solute atoms in the enriched liquid, the particle grows rapidly to a micron size, and is the pushed by the solidifying front to the centreline region, where final solidification occurs. An immediate decrease in concentration in the liquid coincides with the nucleation and growth of the particle, and this is observed after the small spike at off-

centreline positions. The large spike in composition at the centreline is a direct result of the accumulation of coarse particles at the centreline.

Although this proposed scenario may be criticized for its simplicity in comparison with the plethora of events that may have an effect on macrosegregation during continuous casting, one should note that once the majority of solidification has been completed, the system is relatively quiescent and the intense fluxes observed at the beginning of solidification have disappeared. Therefore, one may approximate the solute-enriched liquid as a steady state system; as a result, the solidifying front will move slowly towards the centreline region. From this point of view, it is reasonable to assume that the solidifying front will not overtake the particle and trap it in the matrix. Instead, particle pushing by the solidifying front is more likely. This may be a possible explanation for observing Nb-rich particles (as well as other coarse particles) at the centreline of continuously cast slabs.

The two questions proposed in section 8.2 on page 95 can be answered in the following manner from the perspective of macro segregation and particle pushing: the particles originated by nucleation in the enriched liquid due to macrosegregation, and aligned themselves at the centreline by particle pushing during the last stages of solidification.

9 Conclusion

The existence of coarse particles in HSLA steels has posed a problem for steelmakers for decades. From this angle, Abraham *et al.* proposed that the coarse particles were inherited from ferroalloy additions. Numerous coarse particles were identified as Nb-rich, and for this reason, the characterization of ferroniobium was conducted.

The examination of commercial ferroniobium revealed the existence of two thermally stable phases; these phases were identified as bcc Nb and hcp Nb_2C. The predictions of Thermo-Calc with the Scheil-Gulliver solidification conformed with the microstructural observations for features such as phases, phase fractions, and the influence of carbon. The evidence pointed conclusively to the poisonous effect of carbon on the microstructure of commercial ferroniobium.

Based on the conjecture of Abraham *et al.*[11,12], thermally stable phases in ferroniobium may not dissolve completely in liquid iron. The dissolution of these phases in liquid iron was modeled and compared with experimental data, as well as the commercial software DICTRA. In all cases, the size and type of thermally stable phases observed in ferroniobium were shown to dissolve readily in liquid steel. In addition, the dissolution of the phase NbC (which was not observed in ferroniobium) was modeled and it dissolved easily in liquid iron as well. From these results, it was concluded that the coarse particles observed in HSLA steels did not originate from ferroalloy additions.

Finally, a case study of coarse particles in HSLA steels was conducted on a sample from Evraz. The characterization of these coarse particles revealed that they were

Nb-rich and Ti-rich particles with the fcc crystal structure. Since the fcc phase of NbC dissolved easily in liquid iron, the conjecture that they may form in a solute enriched liquid was proposed. The alignment of the particles at the centreline, as well as their large size, led to further study of how they formed in the liquid, and how they were aligned at the centerline region of the slab. The conclusion of this case study was that a two-fold mechanism was responsible: first, the nucleation and growth of the particles in the solute enriched liquid, and second, a particle pushing mechanism that aligned the particles at the centreline region where they were trapped at final freezing.

Finally, here are proposed further areas that ought to be investigated for the interested persons:

1. Experimental validation of the dissolution of NbC and Nb_2C compounds in liquid iron.
2. A deeper understanding of the precise mechanisms involved in nucleation and growth of particles in solute enriched liquid, particularly in the continuous casting process.
3. An experimental validation of the proposed cause of coarse particles in as-continuously cast HSLA steels and their alignment at the centreline; in particular, careful studies of the centerline composition profile.
4. The prevention of the formation of these coarse particles.

10 Appendices

10.1 Appendix A – Preparation of Microstructures

The ferroniobium alloy contains hard and soft phases and it is difficult to produce a presentable microstructure that is not consumed with mechanical damage induced during the metallographic preparation. The following tables give the preparation procedure for all ferroniobium alloys (Table 16), and the etchant that was used to produce the micrographs (Table 17). Since the etchant is used electrolytically, the settings for electrolytic etching are 10 V for 15–20 seconds.

Table 16 – Metallographic preparation information for ferroniobium

Step	Surface	Suspension	Lubricant	Time (min)	Force, N (per sample)	RPM	Rotation
1	MD-Piano 120	…	Water	15:00	45	300	><
2	MD-Piano 220	…	Water	15:00	45	300	><
3	MD-Piano 500	…	Water	15:00	45	300	><
4	MD-Piano 1200	…	Water	15:00	45	300	><
5	MD-Allegro	9 um	Blue	5:00	35	300	><
6	MD/DP-Plan	6 um	Blue	5:00	35	300	><
7	MD/DP-Dur	3 um	Blue	5:00	35	300	><
8	MD/DP-Dac	1 um	Blue	5:00	30	300	><
9	MD/OP Chem	0.05 um	Water	4:00	25	150	><

Table 17 – Etchant used in producing etched microstructures of ferroniobium

Constituent	H_20	Lactic Acid	Phosphoric Acid	Citric Acid	Oxalic Acid	Ethanol
Amount	140 mL	40 mL	20 mL	20 g	20 g	240 mL

10.2 Appendix B – Correction Factor for Non-dilute Systems

The correction factor is built into the equations because of the flux of B atoms against the flux of A atoms in the liquid medium. In the case that the A atoms are non-dilute, they will diffuse through the B atoms to regions of lower concentration but they

will exchange places with a combination of mostly A atoms and some B atoms (since the liquid is not dilute with atoms of A). If the motion of A atoms is to happen by diffusion, the opposite motion of B atoms must occur to take the place of the A atoms and reduce the concentration.

This corrective factor was adopted from the theory by Geiger *et al.*[53] and the mathematical expressions take on the following form after integration of the first Fick's law with specific boundary conditions:

$$\ln\left(\frac{1-X_A}{1-X_A^0}\right)=\frac{x}{l}\ln\left(\frac{1-X_A^l}{1-X_A^0}\right)$$

$$N_A=-\frac{CD_A}{1-X_A^0}\left(\frac{dX_A}{dx}\right)_{x=0}=\frac{CD_A}{l}\ln\left(\frac{1-X_A^l}{1-X_A^0}\right)$$

$$N_A=\frac{CD_A}{\left(X_B\right)_{\ln}}\left(\frac{X_A^0-X_A^l}{l}\right)$$

where $\left(X_B\right)_{\ln}$ is the log *mean* of the terminal values of X_B.

$$\left(X_B\right)_{\ln}=\frac{X_B^l-X_B^0}{\ln\left(X_B^l/X_B^0\right)}$$

In the case that the system is dilute, $\left(X_B\right)_{\ln}\to 1$, and the flux expression contains only the diffusive flux:

$$N_A=CD_A\left(\frac{X_A^0-X_A^l}{l}\right)$$

10.3 Appendix C – Derivations of Convective Fluid Equations

The intent of this appendix is to reveal the mathematics that give the final result of equations (12) and (13). By simply taking up pen and paper, these equations will be easily

understood. There are two types of convective expressions: forced and natural convection. The starting point of these derivations is the Sherwood number for each type in equations (4) and (5).

10.3.1 Forced Convection

Inserting equation (4) into equation (6) gives:

$$k_F = \frac{D_{Nb}}{2R_{Nb}\left(\omega_{Fe}\right)_{\ln}}\left[2+0.6\,\mathrm{Re}^{1/2}\,Sc^{1/3}\right] = \frac{D_{Nb}}{2R_{Nb}\left(\omega_{Fe}\right)_{\ln}}\left[2+0.6\left(\frac{2\upsilon R_{Nb}}{\nu}\right)^{1/2}\left(\frac{\nu}{D_{Nb}}\right)^{1/3}\right]$$

$$k_F = \frac{D_{Nb}}{R_{Nb}\left(\omega_{Fe}\right)_{\ln}} + \frac{0.6D_{Nb}}{2R_{Nb}\left(\omega_{Fe}\right)_{\ln}}\left(\frac{2\upsilon R_{Nb}}{\nu}\right)^{1/2}\left(\frac{\nu}{D_{Nb}}\right)^{1/3}$$

$$k_F = \frac{D_{Nb}}{R_{Nb}\left(\omega_{Fe}\right)_{\ln}} + \frac{0.6D_{Nb}}{2R_{Nb}\left(\omega_{Fe}\right)_{\ln}}\left(\frac{2^{1/2}\upsilon^{1/2}}{\nu^{1/6}D_{Nb}^{1/3}}\right)R_{Nb}^{1/2} \qquad -(17)$$

Insert (17) into the dissolution equation (9), rearrange and integrate to arrive at equation (12):

$$d\left(R_{Nb}\right) = -\frac{\rho_L}{\rho_{Nb}}\left[\frac{D_{Nb}}{R_{Nb}\left(\omega_{Fe}\right)_{\ln}} + \frac{0.6D_{Nb}}{2R_{Nb}\left(\omega_{Fe}\right)_{\ln}}\left(\frac{2^{1/2}\upsilon^{1/2}}{\nu^{1/6}D_{Nb}^{1/3}}\right)R_{Nb}^{1/2}\right]\left(\omega_{Nb}^{*}-\omega_{Nb}^{\infty}\right)dt$$

$$d\left(R_{Nb}\right) = -\left[\frac{\rho_L D_{Nb}}{\rho_{Nb}R_{Nb}\left(\omega_{Fe}\right)_{\ln}}\left(\omega_{Nb}^{*}-\omega_{Nb}^{\infty}\right) + \frac{0.6\rho_L D_{Nb}}{2\rho_{Nb}R_{Nb}\left(\omega_{Fe}\right)_{\ln}}\left(\omega_{Nb}^{*}-\omega_{Nb}^{\infty}\right)\left(\frac{2^{1/2}\upsilon^{1/2}}{\nu^{1/6}D_{Nb}^{1/3}}\right)R_{Nb}^{1/2}\right]dt$$

$$R_{Nb}d\left(R_{Nb}\right) = -\left[\frac{\rho_L D_{Nb}}{\rho_{Nb}\left(\omega_{Fe}\right)_{\ln}}\left(\omega_{Nb}^{*}-\omega_{Nb}^{\infty}\right) + \frac{0.6\rho_L D_{Nb}}{2\rho_{Nb}\left(\omega_{Fe}\right)_{\ln}}\left(\omega_{Nb}^{*}-\omega_{Nb}^{\infty}\right)\left(\frac{2^{1/2}\upsilon^{1/2}}{\nu^{1/6}D_{Nb}^{1/3}}\right)R_{Nb}^{1/2}\right]dt$$

$$\alpha_F = -\frac{\rho_L D_{Nb}}{\rho_{Nb}\left(\omega_{Fe}\right)_{\ln}}\left(\omega_{Nb}^{*}-\omega_{Nb}^{\infty}\right)$$

$$\beta_F = 0.6\left(\frac{2^{1/2}\upsilon^{1/2}}{\nu^{1/6}D_{Nb}^{1/3}}\right)$$

$$R_{Nb}(t)\; d\left(R_{Nb}\right) = \left[\alpha_F + \frac{1}{2}\alpha_F\beta_F\left(R_{Nb}(t)\right)^{1/2}\right]dt$$

$$\int_{R_0}^{0} \frac{R_{Nb}(t)}{\alpha_F + \frac{1}{2}\alpha_F\beta_F\left(R_{Nb}(t)\right)^{1/2}}\; d\left(R_{Nb}\right) = \int_{0}^{t_f} dt$$

10.3.2 Natural Convection

Inserting equation (5) into equation (7) gives:

$$k_N = \frac{D_{Nb}}{2R_{Nb}(t)}\left[2 + 0.59\left(Gr_m Sc\right)^{1/4}\right] = \frac{D_{Nb}}{2R_{Nb}(t)}\left[2 + 0.59\left(\frac{\left(2R_{Nb}(t)\right)^3 g\Delta\rho}{\nu D_{Nb}}\right)^{1/4}\right]$$

$$k_N = \frac{D_{Nb}}{R_{Nb}(t)} + \frac{0.59D_{Nb}}{2R_{Nb}(t)}\left(\frac{\left(2R_{Nb}(t)\right)^3 g\Delta\rho}{\nu D_{Nb}}\right)^{1/4}$$

$$k_N = \frac{D_{Nb}}{R_{Nb}(t)} + \frac{0.59D_{Nb}}{2R_{Nb}(t)}\left(\frac{8g\Delta\rho}{\nu D_{Nb}}\right)^{1/4}\left(R_{Nb}(t)\right)^{3/4} \qquad -(18)$$

Insert (18) into the dissolution equation (9), rearrange and integrate to arrive at equation (13):

$$d\left(R_{Nb}\right) = -\frac{\rho_L}{\rho_{Nb}}\left[\frac{D_{Nb}}{R_{Nb}\left(\omega_{Fe}\right)_{\ln}} + \frac{0.59D_{Nb}}{2R_{Nb}\left(\omega_{Fe}\right)_{\ln}}\left(\frac{8g\Delta\rho}{\nu D_{Nb}}\right)^{1/4} R_{Nb}^{3/4}\right]\left(\omega_{Nb}^{*} - \omega_{Nb}^{\infty}\right)dt$$

$$d\left(R_{Nb}\right) = -\left[\frac{\rho_L D_{Nb}}{\rho_{Nb}R_{Nb}\left(\omega_{Fe}\right)_{\ln}}\left(\omega_{Nb}^{*} - \omega_{Nb}^{\infty}\right) + \frac{0.59\rho_L D_{Nb}}{2\rho_{Nb}R_{Nb}\left(\omega_{Fe}\right)_{\ln}}\left(\omega_{Nb}^{*} - \omega_{Nb}^{\infty}\right)\left(\frac{8g\Delta\rho}{\nu D_{Nb}}\right)^{1/4} R_{Nb}^{3/4}\right]dt$$

$$R_{Nb}d\left(R_{Nb}\right) = -\left[\frac{\rho_L D_{Nb}}{\rho_{Nb}\left(\omega_{Fe}\right)_{\ln}}\left(\omega_{Nb}^{*} - \omega_{Nb}^{\infty}\right) + \frac{0.59\rho_L D_{Nb}}{2\rho_{Nb}\left(\omega_{Fe}\right)_{\ln}}\left(\omega_{Nb}^{*} - \omega_{Nb}^{\infty}\right)\left(\frac{8g\Delta\rho}{\nu D_{Nb}}\right)^{1/4} R_{Nb}^{3/4}\right]dt$$

$$\alpha_F = -\frac{\rho_L D_{Nb}}{\rho_{Nb}\left(\omega_{Fe}\right)_{\ln}}\left(\omega_{Nb}^{*} - \omega_{Nb}^{\infty}\right)$$

$$\beta_F = 0.59\left(\frac{8g\Delta\rho}{vD_{Nb}}\right)^{1/4}$$

$$R_{Nb}(t)\; d\left(R_{Nb}\right) = \left[\alpha_N + \frac{1}{2}\alpha_N\beta_N\left(R_{Nb}(t)\right)^{3/4}\right]dt$$

$$\int_{R_0}^{0} \frac{R_{Nb}(t)}{\alpha_N + \frac{1}{2}\alpha_N\beta_N\left(R_{Nb}(t)\right)^{3/4}}\, d\left(R_{Nb}\right) = \int_{0}^{t_f} dt$$

10.4 Appendix D – Converting the Coefficients in Mass Flux Expressions

Consider the dissolution of one mole of Nb_xC_y that can be described by the following expression:

$$Nb_xC_y \rightarrow xNb + yC \qquad -(19)$$

The molar flux can then be written as:

$$J_{Nb} = yD_{Nb}\left(C_{Nb}^{*} - C_{Nb}^{\infty}\right)$$
$$J_C = xD_C\left(C_C^{*} - C_C^{\infty}\right)$$

An example is the Nb_2C phase. If ε=1, x=2/3, and y=1/3, then the molar fluxes can be written as:

$$J_{Nb} = \frac{1}{3}D_{Nb}\left(C_{Nb}^{*} - C_{Nb}^{\infty}\right)$$
$$J_C = \frac{2}{3}D_C\left(C_C^{*} - C_C^{\infty}\right)$$

However, when the concentration is in mass percent, the fluxes must be converted from molar fluxes to mass fluxes. In this case, the mole fractions of Nb and C must become

mass fractions in the dissolution expression (19). To do this, the molecular mass of each component in the system is needed:

$$wt.\%\ \mathrm{i} = \frac{(at.\%\ \mathrm{i})(M_i)}{(at.\%\ \mathrm{i})(M_i)+(at.\%\ \mathrm{j})(M_j)+(at.\%\ \mathrm{k})(M_k)+\ldots}\ \mathrm{x}\ 100\%$$

The mass flux equation (3) must now be used with the mass fractions rather than the mole fractions. From this angle, the table below gives the atomic fractions of Nb and C, and their converted mass fractions, which are used in the modeling of dissolution of NbC and Nb_2C.

Table 18 – The conversion of molar to mass fractions for the mass flux equality

	NbC	**Nb_2C**
Atomic fraction, Nb	1/2	2/3
Mass fraction, Nb	ξ=5753/6500	ς=5871/6250
Atomic fraction, C	1/2	1/3
Mass fraction, C	ψ=747/6500	λ=379/6250

10.5 Appendix E – Adjusted Diffusion Coefficients

To compare with the results of DICTRA, one must use the same diffusion coefficients that the commercial software DICTRA uses. Since the kinetics are diffusionally controlled, the value of the diffusion coefficient plays a major role. In fact, the diffusion coefficient has two duties: the determination of flux equality, and equilibrium composition. By changing the diffusion coefficients of carbon and niobium in the DCM to $1x10^{-9}$ m^2/s, the results of the flux equality from the DCM are compared with the DICTRA results, and the dissolution kinetics is also shown for NbC (Figure 59) and Nb_2C (Figure 60).

The results show that the equilibrium compositions at the interface are nearly identical for DICTRA and DCM. The dissolution kinetics of the DCM are increased significantly with the use of the adjusted diffusion coefficients compared to the DICTRA results in Figure 47. One will quickly realize that the time in the steelmaking ladle (~10–50 minutes) and the casting machine (~20–30 minutes) would allow these particles to dissolve easily; thus, these particles would not end up in the cast structure, even if the DCM was an accurate prediction of the dissolution kinetics.

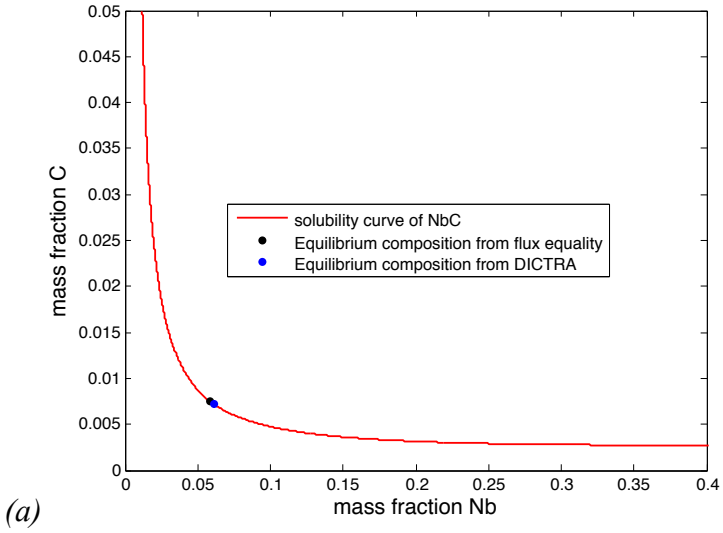

(a)

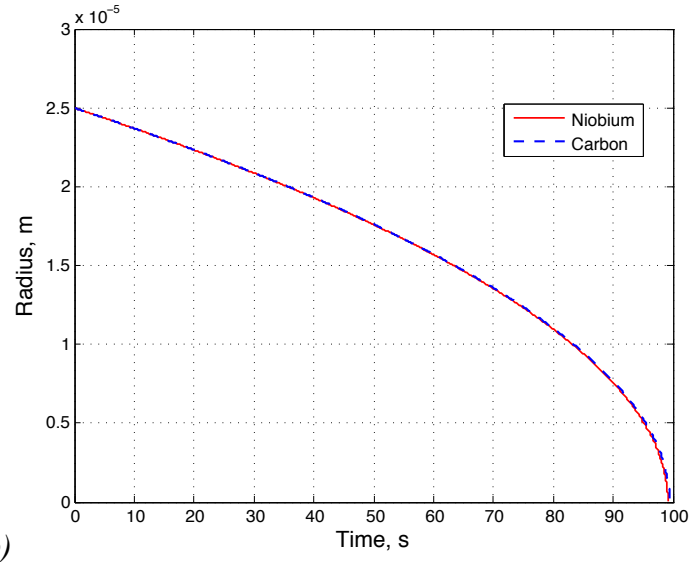

(b)

Figure 59 – *(a)* the equilibrium compositions on the solubility curve of NbC, and *(b)* the predicted dissolution of NbC in pure liquid iron with adjusted diffusion coefficients for niobium and carbon

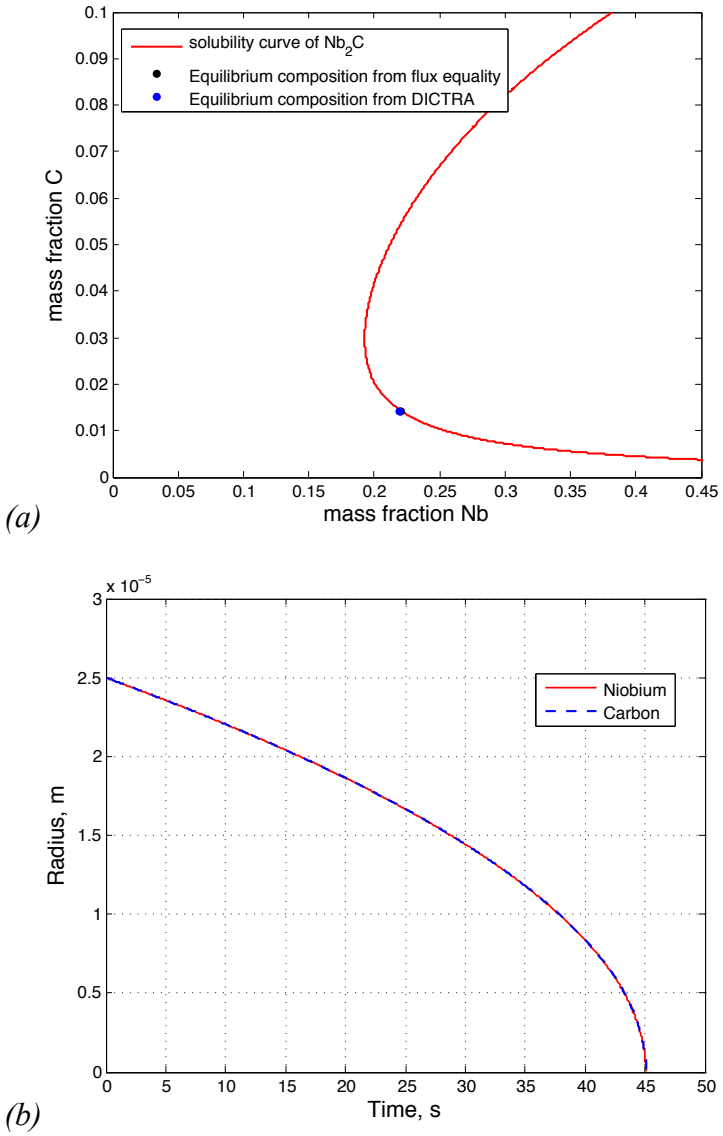

Figure 60 – *(a)* the equilibrium compositions on the solubility curve of Nb_2C, and *(b)* the predicted dissolution of Nb_2C in pure liquid iron with adjusted diffusion coefficients for niobium and carbon; note that the equilibrium compositions of DICTRA and the DCM are almost identical

11 Reference List

1. Rashid, M. S.: 'High-strength, low-alloy steels', *Science*, 1980, **208**, (4446), 862-869.

2. Porter, L. F.; Repas, P. E.: 'Evolution of HSLA Steels', *Journal of Metals*, 1982, **34**, (4), 14-21.

3. Paules, J. R.: 'Developments in HSLA Steel Products', *JOM*, 1991, **43**, (1), 41-44.

4. Kushida, T.; Okaguchi, S.; Hamada, M.; Yamamoto, A.; Ohnishi, K.: 'STUDY OF X80 GRADE HIGH STRENGTH LINE PIPE FOR SOUR SERVICE', *T. Kushida, S. Okaguchi, M. Hamada, A. Yamamoto, K. Ohnishi, and J. Fujino (Sumitomo Metal Industries, Ltd. , Japan), Paper No. 24. Presented at CORROSION/97 (March 10-14, 1997, New Orleans, LA), Sponsored by NACE International*, 1997.

5. Chen, Z.; Loretto, M. H.; Cochrane, R. C.: 'Nature of large precipitates in titanium-containing HSLA steels', *Materials Science and Technology*, 1987, **3**, (10), 836-844.

6. Tian, Q.; Chen, Y.; Chen, J.; Xu, G.; Zheng, Y. Characterization of Nb-rich Phase Precipitation near Internal Cracks in Continuously Cast Slabs. Minerals, Metals and Materials Society (TMS), 184 Thorn Hill Road, Warrendale, PA, 15086-7528, USA: 2007.

7. Zhuo, X.; Wang, X.; Wang, W.; Lee, H. G.: 'Nature of large (Ti, Nb)(C, N) particles precipitated during the solidification of Ti, Nb HSLA steel', *Journal of University of Science and Technology Beijing: Mineral Metallurgy Materials (Eng Ed)*, 2007, **14**, (2), 112-117.

8. Zhuo, X.; Woo, D.; Wang, X.; Lee, H.: 'Formation and thermal stability of large precipitates and oxides in titanium and niobium microalloyed steel', *Journal of Iron and Steel Research International*, 2008, **15**, (3), 70-77.

9. Zhou, C.; Priestner, R.: 'The Evolution of Precipitates in Nb-Ti Microalloyed Steels during Solidification and Post-solidification Cooling', *ISIJ International*, 1996, **36**, (11), 1397-1405.

10. Mendoza, R.; Huante, J.; Alanis, M.; Gonzalez-Rivera, C.; Juarez-Islas, J. A.: 'Slab cracking after continuous casting of API 5L X-70 grade steel for pipeline sour gas application', *Ironmaking and Steelmaking*, 1999, **26**, (3), 205-209.

11. Abraham, S.; Klein, R.; Bodnar, R.; Dremailova, O. Formation of Coarse Particles in Steel as related to Ferroalloy Dissolution Thermodynamics Part I: Ferroalloy Melting, Dissolution and Microstructures. Minerals, Metals and Materials Society (TMS): 2007.

12. Abraham, S.; Klein, R.; Bodnar, R.; Dremailova, O. Formation of Coarse Particles in Steel as related to Ferroalloy Dissolution Thermodynamics Part II: Crystallographic Study of Ferroalloys and Coarse Particles. Minerals, Metals and Materials Society (TMS): 2007.

13. De Faria Sousa, C. A. The evolution of FeNb manufacturing. In *Niobium, Science and Technology*; Minerals, Metals and Materials Society: Orlando, FL, United states, 2001; pp 89-96.

14. Paul, E.; Swartzendruber, L. J.: 'The Fe--Nb (Iron--Niobium) System', *Bull. Alloy Phase Diagrams*, 1986, **7**, (3), 248-254.

15. Huang, W.: 'A thermodynamic evaluation of the Fe-Nb-C system', *Zeitschrift fur Metallkunde*, 1990, **81**, (6), 397-404.

16. Bejarano, J. M. Z.; Gama, S.; Ribeiro, C. A.; Effenberg, G.; Santos, C.: 'On the existence of the Fe2Nb3 phase in the Fe-Nb system', *Zeitschrift fuer Metallkunde/Materials Research and Advanced Techniques*, 1991, **82**, (8), 615-620.

17. Zelaya Bejarano, J. M.; Sanjurjo, N. L.; Gama, S.; Ribeiro, C. A.; Campos, C.: 'X-ray study of alloys of the Fe-Nb system', *Revista de Fisica Aplicada e Instrumentacao*, 1996, **11**, (4), 156-160.

18. Bejarano, J. M. Z.; Gama, S.; Ribeiro, C. A.; Effenberg, G.: 'The iron-niobium phase diagram', *Zeitschrift fur Metallkunde*, 1993, **84**, (3), 160-164.

19. Voss, S.; Palm, M.; Stein, F.; Raabe, D.: 'Phase Equilibria in the Fe-Nb System', *Journal of Phase Equilibria and Diffusion*, 2011, **32**, (2), 97-104.

20. Khvan, A. V.; Hallstedt, B.: 'Thermodynamic description of the Fe-Mn-Nb-C system', *CALPHAD: Computer Coupling of Phase Diagrams and Thermochemistry*, 2012, **39**, 62-69.

21. Khvan, A. V.; Hallstedt, B.: 'Thermodynamic assessment of FeMnNbN and NbCN systems', *CALPHAD: Computer Coupling of Phase Diagrams and Thermochemistry*, 2013, **40**, 10-15.

22. Toffolon, C.; Servant, C.: 'Thermodynamic assessment of the Fe-Nb system', *CALPHAD: Computer Coupling of Phase Diagrams and Thermochemistry*, 2000, **24**, (2), 97-112.

23. Raman, A.: 'STRUCTURAL STUDY OF NIOBIUM-IRON ALLOYS', *INDIAN ACAD SCI PROCEED*, 1967, **65**, (4), 256-265.

24. Argyropoulos, S. A.; Guthrie, R. I. L. Dissolutions kinetics of ferroalloys in steelmaking. In *Steelmaking Conference Proceedings*; Iron & Steel Soc of AIME: Pittsburgh, PA, USA, 1982; pp 156-167.

25. Argyropoulos, S. A.: 'Dissolution Characteristics of Ferroalloys in Liquid Steel', *Electric Furnace Proceedings, Vol. 41; Detroit, Mich. ; U. S. A. ; 6-9 Dec. 1983*, 1983, 81-93.

26. Sismanis, P. G.; Argyropoulos, S. A.: 'Dissolution of niobium, boron and zirconium ferroalloys in liquid steel and liquid iron', *I & SM*, 1989, **16**, (7), 39-47.

27. Argyropoulos, S. A. Effect of microexothermicity and macroexothermicity on the dissolution of ferroalloys in liquid steel. In *Electric Furnace Conference Proceedings*; Iron & Steel Soc of AIME: Toronto, Ont, Can, 1985; pp 133-148.

28. Argyropoulos, S. A.; Sismanis, P. G.: 'The mass transfer kinetics of niobium solution into liquid steel', *Metallurgical Transactions B (Process Metallurgy)*, 1991, **22B**, (4), 417-427.

29. Gourtsoyannis, L.; Guthrie, R. I. L.; Ratz, G. A. Dissolution of ferromolybdenum, ferroniobium and rare earth (lanthanide) silicide in cast iron and steel melts. In *Electric Furnace Conference Proceedings*; Iron & Steel Soc of AIME: Toronto, Ont, Can, 1985; pp 119-132.

30. Sismanis, P. G.; Argyropoulos, S. A.: 'Modelling of exothermic dissolution', *Canadian Metallurgical Quarterly*, 1988, **27**, (2), 123-133.

31. Saunders, N.; Miodownik, A. P. *CALPHAD (Calculation of Phase Diagrams): A Comprehensive Guide;* 1 ed.; Pergamon: 1998.

32. Lukas, H.; Fries, S. G.; Sundman, B. *Computational thermodynamics: the Calphad method;* Cambridge University Press: 2007.

33. Argyropoulos, S. A.; Guthrie, R. I. L.: 'The Influence of High Exothermic Heats of Dissolution on the Solution of Solid Alloy Additions Into Molten Baths of Steel', *Heat and Mass Transfer in Metallurgical Systems; Dubrovnik; Yugoslavia; Sept. 1979*, 1979, 159-174.

34. Guthrie, R. I. L.; Gourtsoyannis, L.: 'Melting rates of furnace or ladle additions in steelmaking', *Canadian Metallurgical Quarterly*, 1971, **10**, (1), 37-46.

35. Webber, D. S.; Peaslee, K. D.; Von Richards, L. Nickel dissolution in argon stirred steel. In *ICS 2005 - Proceedings of the 3rd International Congress on the Science and Technology of Steelmaking*; Association for Iron and Steel Technology, AISTECH: Charlotte, NC, United states, 2005; pp 811-819.

36. Webber, D. S.; Peaslee, K. D.; Von Richards, L. Alloy dissolution in argon stirred steel. In *AISTech 2004 - Iron and Steel Technology Conference Proceedings*; Association for Iron and Steel Technology, AISTECH: Cleveland, OH, United states, 2006; pp 741-752.

37. Brabie, L. C.; Kawakami, M.: 'Kinetics of steel scrap melting in molten Fe-C bath', *High Temperature Materials and Processes (UK) (UK)*, 2000, **19**, (3-4), 241-255.

38. Li, J.; Brooks, G.; Provatas, N.: 'Kinetics of scrap melting in liquid steel', *Metallurgical and Materials Transactions B: Process Metallurgy and Materials Processing Science*, 2005, **36**, (2), 293-302.

39. Purdy, G. R.; Malakhov, D. V.; Guha, A.: 'Homogenization of multicomponent alloys via partial melting', *Journal of Phase Equilibria*, 2001, **22**, (4), 439-450.

40. Sismanis, P. G.; Argyropoulos, S. A.: 'The Effect of Oxygen on the Recovery and Dissolution of Ferroalloys. (Retroactive Coverage)', *Steelmaking Proceedings. Vol. 69; Washington, D. C. ; USA; 6-9 Apr. 1986*, 1986, 315-326.

41. Sheshukov, O. Y.; Vyaznikova, E. A.; Smirnova, V. G.; Ovchinnikova, L. A.: 'Influence of the cooling rate on the structure of silicon ferroalloys', *Steel in Translation*, 2011, **41**, (4), 323-325.

42. Crouse, R. S.; Oak Ridge National Laboratory Metals and Ceramics Division; U.S.Atomic Energy Commission *Identification of carbides, nitrides, and oxides of niobium and niobium alloys by anodic staining;* Oak Ridge National Laboratory: 1965.

43. Bergerhoff, G.; Brown, I. D. Inorganic Crystal Structure Database. Allen, F. H., Bergerhoff, G., Sievers, R., Eds.; Int. Union Crystallogr., Data Comm., Chester, United Kingdom: 1987; pp 77-95.

44. Bird, R. B.; Stewart, W. E.; Lightfoot, E. N. Transport phenomena. Wiley: New York, 1960; p 780.

45. Incropera, F. P.; Lavine, A. S.; DeWitt, D. P. *Fundamentals of heat and mass transfer;* John Wiley & Sons Incorporated: 2011.

46. Ershov, G. S.; Maiboroda, V. P.; Permyakova, T. V.: 'Influence of temperature and alloying elements on the diffusion rate of carbon in liquid iron', *Russian metallurgy. Metally*, 1989, (1), 22-25.

47. Ershov, G. S.; Kasatkin, A. A.; Gavrilin, I. V.: 'Diffusion of alloying elements in liquid iron', *Izvestiya Akademii Nauk SSSR, Metally*, 1978, (2), 76-79.

48. Shunyaev, K. Y.; Korchemkina, N. V.; Lisin, V. L.; Chentsov, V. P.; Pechischeva, N. V. The iron-niobium phase diagram and the viscosity of liquid alloys in this system. 2002.

49. Coudure, J. M.; Irons, G. A.: 'The Effect of Calcium Carbide Particle-Size Distribution on the Kinetics of Hot Metal Desulfurization', *ISIJ International*, 1994, **34**, (2), 155-163.

50. Moore, J. J.: 'REVIEW OF AXIAL SEGREGATION IN CONTINUOUSLY CAST STEEL', *I & SM*, 1980, **7**, (10), 8-16.

51. Aminorroaya-Yamini, S.: 'Effect of titanium additions to low carbon, low manganese steels on sulphide precipitation', *University of Wollongong Thesis Collection*, 2008, 403.

52. Presslinger, H.; Mayr, M.; Tragl, E.; Bernhard, C.: 'Assessment of the Primary Structure of Slabs and the Influence on Hot- and Cold-Rolled Strip Structure', *Steel Research International*, 2006, **77**, (2), 107-115.

53. Poirier, D. R.; Geiger, G. H. Transport phenomena in materials processing /. Minerals Metals & Materials Society: Warrendale, Pa., 1994; pp xii, 658.